A Study on Sodium Secondary Batteries Using Ionic Liquids as Electrolytes

Atsushi Fukunaga

2016

Contents

Chapter 1

General introduction

1.1 Electrochemical energy storage

The prevention of global warming and the reduction of dependence on nuclear power generation are urgent issuesover the world [1–3]. Although there are increasing demands for renewable energy such as photovoltaic and wind power generations, supplying high quality electricity to the grids is also important. The introduction of renewable energy requires the entire society to reconsider the generation and use of electric power [1]. As a result, technologies and systems which enable mass introduction of renewable energy are attracting more attention nowadays [4–7].

The devices which compensate the intermittency are required to utilize the renewable energy [1, 2]. Energy storage system (ESS) is the key technology for the mass introduction of renewable energy into the grids (see Fig. 1–1) [8, 9]. Several types of energy storage such as mechanical, electrical, chemical, and electrochemical storages are considered for large scaled stationary power supply [10, 11]. Especially, electrochemical energy storages, which are represented by secondary batteries, are recognized as ones of the best solutions owing to their high efficiency, high energy

density, and scalability [2, 10, 11].

Fig. 1–2, Table 1–1, and Table 1–2 show the comparison of the characteristics for several different batteries. Lithium–ion batteries (LIBs) have the highest gravimetric energy density, power density and cycleability [11–15]. As a result, LIBs have dominated the world market for the portable electronic power sources. Nowadays, LIBs are regarded as the best candidate for the uses in electronic vehicles (EVs) and large scaled stationary ESS. However, lithium resources are unevenly distributed in South America, which poses risks to the stable supply of lithium [16–18]. In the future, a shortage of Li resources and a price increase, which resembles oil crisis, can happen by the raising demands of LIBs. Therefore, alternative batteries compensating the shortage of lithium ion batteries are necessary to be developed.

1.2 Sodium secondary batteries

Sodium has chemical properties similar to those of lithium, as expected from its position in the periodic table of elements. Considering the standard redox potential of sodium, –2.714 V vs. SHE, close to that of Li, and the even distribution and high abundance of sodium resources, sodium secondary batteries are potential alternatives to LIBs. Typical chemical properties of sodium and lithium are shown in Table 1–3.

1.2.1 High temperature sodium secondary batteries

Early research on sodium secondary batteries focused on Na/S (NAS) and $Na/NiCl_2$ (ZEBRA) systems that utilize β''–alumina solid electrolyte and are operated in high temperature region (573–623 K) [19–23]. While NAS and ZEBRA systems have been commercialized for large scaled ESS, necessity of thermal management (573–623 K) to keep their performance is one of their drawbacks [24]. Furthermore, utilization of sodium metal as their negative electrode results in the decrease of total energy density because a large scaled incidental facility is required to ensure safety and legality [25]. Recently, alternative electrolytes to β''–alumina such as NASICON–type and glass ceramic electrolytes are being investigated [23]. The recent trend of researches on Na/S batteries has shifted towards the intermediate temperatures operation (373–443 K), though they are still in the early stage of development [23, 26].

1.2.2 Room temperature sodium secondary batteries

Sodium and lithium secondary batteries employing non–aqueous electrolytes and intercalation chemistry were first investigated in late 1970s and 1980s in parallel [27–30]. However, the commercial success of LIBs, which occurred in early 1990s,

made the battery community to focus on only LIBs. Recently, research interest in room temperature sodium secondary batteries has been resurrected, driven by the excellent potential for the development of affordable large scaled batteries, and offering the prospect of lessening the dependence on LIBs [31–36]. More specifically, for example, sodium secondary batteries have a merit in the current collector material of negative electrode, compared with LIBs. Since sodium does not make alloy with aluminum, aluminum current collector is applicable for the negative electrode of sodium secondary batteries, while more expensive copper should be used for LIBs [32]. Moreover, considering the chemical similarity between sodium and lithium, the mass production technologies for LIBs is also utilized in manufacturing large–sized sodium secondary batteries with a minimum development cost.

The principal concept of rocking–chair type Na secondary batteries is shown in Fig. 1–3. Positive and negative electrodes are made of Na intercalation compounds (active materials) electrically connected to current collectors. Generally, these electrodes are fabricated by coating active materials mixed with conductive additive and binder materials on metal foil current collectors. A porous insulating material (separator) is sandwiched between the positive and negative electrodes. The electrolyte which transports Na ions is filled in the stacked cell consisting of two electrodes and a

separator. During charging, Na ion extraction from positive electrode and Na ion insertion into negative electrode proceed simultaneously. The discharge reaction is the inverse of charge reaction during the repeat of charge–discharge process, the Na ions are shuttled between the negative and positive electrodes.

1.3 Positive electrode materials for sodium secondary batteries

Two classes of positive electrode materials are well–investigated: layered oxides [37–54] that have stacked structure of Na layer and MO_2 layer (M = transition metal), and polyanionic compounds [55–94] that possess octahedral interstitial sites available for Na accommodation. In this thesis, layered oxide $NaCrO_2$ that has excellent cycle ability and moderate gravimetric energy density is employed in order to construct highly stable sodium secondary batteries.

As in the case of LIBs, layered oxides Na_xMO_2 have been most widely investigated as positive electrode materials for Na secondary batteries [37–42]. The stacked structure is consisted of edge–shared MO_6 octahedra layers and Na ions are located between these layers. Most of Na_xMO_2 can be categorized into two groups with the classification defined by Delmas [43], O3 and P2 phases. As shown in Fig. 1–4, they are different in the stacking order of the oxygen layers (ABCABC for O3, and ABBA for

P2) and hence the intercalation sites for Na ions (octahedral for O3 and trigonal prismatic for P2). The number 3 in O3 or 2 in P2 describes the number of transition metal (M) layers along the stacking direction in the unit cell. For instance, $NaMnO_2$ [37], $NaCrO_2$ [39, 44, 45], $NaFeO_2$ [46], Na_xCoO_2 [38], and $NaNiO_2$ [47] are well–known positive electrode materials which utilize the 3d transition metals as the redox couples.

In order to improve the electrochemical performance of $NaMO_2$ positive electrode materials, solid–solutions of Na_xMO_2 have been investigated [40–42, 48–51]. P2–$Na_{0.67}[Fe_{0.5}Mn_{0.5}]O_2$ is the most prospective material in terms of reversible capacity (*ca*. 190 mAh g^{-1}) and energy density (*ca*. 520 Wh kg^{-1}) for the cell operating at room temperatures [41, 50, 51]. However, the capacity retention after 40 cycles was less than 80% of initial capacity. Moreover, compensating Na defection of P2–$Na_{0.67}[Fe_{0.5}Mn_{0.5}]O_2$ as prepared is necessary to use the entire reversible capacity of 190 mAh g^{-1}, which is a serious disadvantage for practical application. On the other hand, O3–$NaMO_2$ positive electrodes deliver moderate reversible capacities of *ca*. 120 mAh g^{-1} but generally have better cycleability. In addition, O3–$NaMO_2$ does not have Na defection as prepared state. The electrochemical properties of $NaMO_2$ positive electrodes described above are summarized in Table 1–4. Among them, O3–$NaCrO_2$ has been proved to possess good thermal stability even at the fully charged state of $Na_{0.5}CrO_2$ [44].

Therefore, the author has selected $NaCrO_2$ for the best candidate for long cycle life and safe Na secondary batteries operating even in the intermediate temperature region. The results of charge–discharge tests are presented in Chapters 3, 4 and 6.

1.4 Negative electrode materials for sodium secondary batteries

For LIBs, carbon materials, especially graphite, are generally used as the negative electrode active material, and their science and technology have been well developed [95]. However, graphitic carbons are not applicable for Na secondary batteries because sodium, unlike lithium, does not form intercalation compounds with graphite [95–98]. Recently, many non–graphitic carbonaceous materials that can storage Na atoms have been investigated, such as petroleum cokes [99], carbon black [100], soft carbons (small crystalline domains of ordered graphene) [95] and hard carbons (disordered with nanoscale porosity) [95, 96, 101–103]. Among them, hard carbons are the most investigated material and are regarded as the first–generation negative electrodes for Na secondary batteries. Generally, hard carbons exhibit capacities of 200–300 mAh g^{-1}. Since hard carbons are now being commercially produced as the negative electrode material for LIBs, their costs are reasonably low due to a mass production effect. From these reasons, the author has selected the hard carbon as a negative electrode material in

this thesis. The results of charge–discharge tests for hard carbon negative electrodes are described in Chapters 5 and 6.

According to the previous investigation on hard carbons conducted in an organic solvent based electrolyte at room temperature [95], during the initial Na intercalation into hard carbons, part of Na ions react with the electrolyte to form an electronically insulating but ionically conductive layer at the surface of carbon powders, which is known as the solid electrolyte interphase (SEI). Such an SEI forming reaction is one of the contributing factors of irreversible capacity for carbon electrodes. The irreversible capacity should be as small as possible because it confuses the amount of Na ions which can be transferred 'reversibly' between positive and negative electrodes [104]. So far, many nanostructured carbon materials have been investigated as negative electrodes, and the improved capacities and kinetics have been reported [105, 106]. However, the large irreversible capacity and unsatisfactory coulombic efficiency make them difficult to be applied to the practical batteries. The relatively large surface area of nanostructured materials is considered to be the main factor for the unavoidable irreversible capacity [33].

Similar to LIBs, there are many candidates of alloy negative electrodes that have high theoretical capacities compared with intercalation–based materials such as Sn

[107], Sn/Cu [108], Sn/C [109], SnO_2/graphene [110], Sb/C [111], and SnSb/C [112]. Among them, nanocomposites of SnO_2/graphene and Sb/C have been reported to deliver large reversible capacities of 600–700 mAh g^{-1} with moderate cycleability over 100 cycles [110, 111]. Recently, amorphous red phosphorous/carbon composite has been demonstrated to exhibit the highest reversible capacity of 1890 mAh g^{-1} (~$Na_{2.18}P$) [113]. For these composites electrodes, carbon matrix is considered to play important roles as conductive and buffering matrix to effectively release the mechanical stress caused by expansion/contraction of active materials upon Na insertion/extraction (alloying/dealloying) [111]. However, in spite of the high capacity of alloy compounds, their practical applications are still challenging, similar to the cases of LIBs [31, 98].

1.5 Electrolytes

Electrolytes play the key role of Na ion conduction between positive and negative electrodes. The electrochemical performance of batteries such as output power strongly depends on the ionic conductivity of electrolytes. Moreover, since electrolytes account for substantial portion of batteries, the safety of batteries is closely related to the nature of electrolytes [115–117]. However, electrolytes which enable the operation of Na secondary batteries are relatively limited [118–120]. To achieve the satisfactory

performance as practical batteries, the following properties are required for the electrolyte [23, 115–117]; (i) high ionic conductivity; (ii) high thermal stability; (iii) physical and chemical compatibility with the electrodes; (iv) low toxicity; (v) high safety; (vi) low cost. In this section, three types of electrolytes for Na secondary batteries are described.

1.5.1 Organic electrolytes

Carbonate–based solvents such as ethylene carbonate (EC), propylene carbonate (PC) and dimethyl carbonate (DMC), in which either $NaClO_4$ or $NaPF_6$ is dissolved, are regarded as the conventional electrolytes for sodium secondary batteries. The most common electrolyte based on organic solvent is 1 mol dm^{-3} $NaClO_4$ in PC, because PC possesses a wider liquid temperature range and a higher flash point compared with EC and other linear alkyl carbonates [102, 116]. These solutions have high ionic conductivities and low viscosities and adequate stability in the operation voltage range of Na secondary batteries. For hard carbon negative electrodes, the use of fluoroethylene carbonate (FEC) additive [121] is important in order to control the surface reaction between the electrode and the electrolyte, as reported in recent papers [107, 111, 113].

Although comprehensive investigations have proven that hard carbon is the first candidate as a negative electrode for Na secondary batteries, its electrochemical performance strongly depends on the kinds of electrolytes [102, 118, 119]. Moreover, the fully charged hard carbon (Na_xC) exhibits higher reactivity in organic electrolytes compared with Li_xC_6 of LIBs, which raises imperative concerns about the chemical stability of the organic electrolyte [122]. Formation of Na metallic dendrites on the negative electrode during charge also leads to a serious safety issue, because of the high reactivity of Na metal with carbonates and its low melting point (371 K) [32, 98].

1.5.2 Aqueous electrolytes

Aqueous Na secondary battery is another candidate in viewpoint of cost and safety [33]. Utilization of inexpensive sodium salts such as Na_2SO_4 and $NaNO_3$ has been investigated [123–125]. Since aqueous electrolytes have much higher ionic conductivity than organic solvents, aqueous Na secondary batteries provide high power, high efficiency, high safety, and longer cycle life. However, the narrow electrochemical window of water confines the cell voltage and thus the energy density of the batteries [33–35].

1.5.3 Ionic liquid electrolytes

Ionic liquid (ILs) have attracted much interests among researchers because of their unique properties such as flame resistance, negligible volatility, electrochemical stability, and thermal stability [126–128]. Several attractive advantages are expected when ILs are applied to the electrolyte of sodium secondary batteries; (i) flame resistance provides high safety; and (ii) thermal stability enables the batteries to be operated in wider temperature range. Since most research efforts from the battery community have targeted the development of electrode materials, the adoption of ionic liquid electrolytes for Na secondary batteries has received less attention [129–131].

Hagiwara *et al*. have investigated a series of ILs based on bis(fluorosulfonyl)amide (FSA) anions and bis(trifluoromethylsulfonyl)amide (TFSA) anions for battery applications at 340–440 K [132–135]. For instance, the Na[FSA]–K[FSA] system is suitable for Na battery operating around 363 K [136–138], while the Na[TFSA]–Cs[TFSA] system can be employed at 423 K [139]. In contrast to conventional ILs that usually contain expensive organic cations, Na[FSA] and K[FSA] are simple and cost-effective inorganic compounds. It should be noted that, unlike TFSA salts, FSA salts can be synthesized without the costly electrochemical fluorination process. Thus, FSA salts are well expected to be produced at a reasonably

low price in the near future. Recently, the Na[FSA]–[C_3C_1pyrr][FSA] (C_3C_1pyrr = *N*–methyl–*N*–propylpyrrolidinium) IL has been proposed, focusing on the low melting point (264 K), high conductivity, and good thermal stability of [C_3C_1pyrr][FSA] [140]. The structures of FSA anion and C_3C_1pyrr cation are shown in Fig. 1–5. By utilizing this IL as an electrolyte, good charge-discharge properties have been obtained for $Na_2FeP_2O_7$, $Na_{1.56}Fe_{1.22}P_2O_7$, and Na_2MnSiO_4 positive electrodes over 298–363 K [141–143].

1.6 Aim of this study

By summarizing the recent studies, sodium secondary batteries having long cycle life in intermediate temperature region are well expected to be constructed using the ionic liquid as an electrolyte. Thus, the aim of this study is to confirm the potential high performance of sodium secondary batteries utilizing ionic liquids. For this purpose, the following studies have been conducted.

In Chapter 3, the psychochemical properties of Na[FSA]–K[FSA] ionic liquid were investigated to collect fundamental data. Then, the charge–discharge properties of layered oxide $NaCrO_2$ were investigated in Na[FSA]–K[FSA] ionic liquid at 363 K.

In Chapter 4, the author revealed the psychochemical properties of Na[FSA]–

[C_3C_1pyrr][FSA] ionic liquid. Then, the charge–discharge behavior of $NaCrO_2$ was studied in Na[FSA]–[C_3C_1pyrr][FSA] ionic liquid in the temperature region of 273–363 K. The effects of Na^+ concentration on the charge-discharge properties were also investigated.

In Chapter 5, the charge–discharge behaviors of hard carbon negative electrode in Na[FSA]–K[FSA] and Na[FSA]–[C_3C_1pyrr][FSA] ionic liquids were studied at 363 K. The influence of K^+ ion in the ionic liquids on the charge-discharge properties was also investigated.

In Chapter 6, a coin-type full cell of hard carbon/Na[FSA]–[C_3C_1pyrr][FSA]/ $NaCrO_2$ was constructed and evaluated for demonstrating the capability of practical use. The author also fabricated a large–sized prismatic cell by mass production process and evaluated its performance. The obtained results such as energy density and cycle performance were compared with those of large–scaled LIBs.

References

[1] Z.G. Yang, J.L. Zhang, M.C.W. Kintner–Meyer, X.C. Lu, D.W. Choi, J.P. Lemmon, J. Liu, Chem. Rev. 111 (2011) 3577–3613.

[2] B. Dunn, H. Kamath, J.M. Tarascon, Science 334 (2011) 928–935.

[3] J. Liu, J.G. Zhang, Z.G. Yang, J.P. Lemmon, C. Imhoff, G.L. Graff, L.Y. Li, J.Z. Hu, C.M.Wang, J. Xiao, G. Xia, V.V. Viswanathan, S. Baskaran, V. Sprenkle, X.L. Li, Y.Y. Shao, B. Schwenzer, Adv. Funct. Mater. 23 (2013) 929–946.

[4] J.P. Holdren, Science 315 (2007) 737–737.

[5] P. Simon, Y. Gogotsi, Nat. Mater. 7 (2011) 845–854.

[6] T.R. Cook, D.K. Dogutan, S.Y. Reece, Y. Surendranath, T.S. Teets, D.G. Nocera, Chem. Rev. 110 (2010) 6474–6502.

[7] D. Ginley, M.A. Green, R. Collins, MRS Bull. 33 (2008) 355–364.

[8] J. Tollefson, Nature 456 (2008) 436–440.

[9] E. Marris, Nature 454 (2008) 570–573.

[10] M. Winter, R.J. Brodd, Chem. Rev. 104 (2004) 4245–4269.

[11] G.L. Soloveichik, Annu. Rev. CHem. Biomol. Eng. 2 (2011) 503–527.

[12] V. Etacheri, R. Marom, R. Elazari, G. Salitra, D. Aurbach, Energy Environ. Sci. 4 (2011) 3243–3262.

[13] J.B. Goodenough, Y. Kim, Chem. Mater. 22 (2010) 587–603.

[14] J.M. Tarascon, M. Armand, Nature 414 (2001) 359–367.

[15] B. Scrosati, J. Hassoun, Y.K. Sun, Energy Environ. Sci. 4 (2011) 3287–3295.

[16] J.M. Tarascon, Nat. Chem. 2 (2010) 510–510.

[17] W. Tahil, The Trouble with Lithium: Implications of Future PHEV Production for Lithium Demand (Meridian International Research, 2007). http://go.nature.com/jhDqLH

[18] W. Tahil, The Trouble with Lithium 2: Under the Microscope (Meridian International Research, 2006). http://go.nature.com/AWITRo

[19] Y.F.Y. Yao, J.T. Kummer, J. Inorg. Nucl. Chem. 29 (1967) 2453–2475.

[20] J.L. Sudworth, J. Power Sources 11 (1984) 143–154.

[21] J. Coetzer, J. Power Sources 18 (1986) 377–380.

[22] C.H. Dustmann, J. Power Sources 127 (2004) 85–92.

[23] K.B. Hueso, M. Armand, T. Rojo, Energy Environ. Sci. 6 (2013) 734–749.

[24] X.C. Lu, G.G. Xia, J.P. Lemmon, Z.G. Yang, J. Power Sources 195 (2010) 2431–2442.

[25] S.F Song, Z.Y. Wen, Y. Liu, J. Lin, X.G. Xu, Q.X. Zhang, J. Solid State Electrochem. 14 (2010) 1735–1740.
[26] X.C. Liu, B.W. Kirby, W. Xu, G.S. Li, J.Y. Kim, J.P. Lemmon, V.L. Sprenkle, Z.G. Yang, Energy Environ. Sci. 6 (2013) 299–306.
[27] M.S. Whittingham, Prog. Solid State Chem. 12 (1978) 41–99.
[28] K.M. Abraham, Solid State Ionics 7 (1982) 199–212.
[29] C. Delmas, JJ. Braconnier, C. Fouassier, P. Hagenmuller, Solid State Ionics 3–4 (1983) 165–169.
[30] J.M. Tarascon, G.W. Hull, Solid State Ionics 22 (1986) 85–96.
[31] S.W. Kim, D.H. Seo, X.H. Ma, G. Ceder, K. Kang, Adv. Energy Mater. 2 (2012) 710–721.
[32] M.D. Slater, D. Kim, E. Lee, C.S. Johnson, Adv. Funct. Mater. 23 (2013) 947–958.
[33] H.L. Pan, Y.S. Hu, L.Q. Chen, Energy Environ. Sci. 6 (2013) 2338–2360.
[34] B.L. Ellis, L.F. Nazar, Curr. Opin, Solid State Mater. Sci. 16 (2012) 168–177.
[35] V. Palomares, M. Casas–Cabanas, E. Castillo–Martinez, M.H. Han, T. Rojo, Energy Environ. Sci. 6 (2013) 2312–2337.
[36] V. Palomares, P. Serras, I. Villaluenga, K.B. Hueso, J. Carretero–Gonzalez, T. Rojo, Energy Environ. Sci. 5 (2012) 5884–5901.
[37] X.H. Ma, H.L. Chen, G. Ceder, J. Electrochem. Soc. 158 (2011) A1307–A1312.
[38] R. Berthelot, D. Carlier, C. Delmas, Nat. Mater. 10 (2011) 74–80.
[39] S. Komaba, C. Takei, T. Nakayama, A. Ogata, N. Yabuuchi, Electrochem. Commun. 12 (2012) 355–358.
[40] S. Komaba, N. Yabuuchi, T. Nakayama, A. Ogata, T. Ishikawa, I. Nakai, Inorg. Chem. 51 (2012) 6211–6220.
[41] N. Yabuuchi, M. Kajiyama, J. Iwatate, H. Nishikawa, S. Hitomi, R. Okuyama, R. Usui, Y. Yamada, S. Komaba, Nat. Mater. 11 (2012) 512–517.
[42] J. Billaud, G. Singh, A.R. Armstrong, E. Gonzalo, V. Roddatis, M. Armand, T. Rojob, P.G. Bruce, Energy Environ. Sci. 7 (2014) 1387–1391.
[43] C. Delmas, C. Fouassier, P. Hagenmuller, Physica B & C 99 (1980) 81–85.
[44] X.Xia, J.R. Dahn, Electrochem. Solid State Lett. 15 (2012) A1–A4.
[45] J.J. Ding, Y.N. Zhou, Q. Sun, Z.W. Fu, Electrochem. Commun. 22 (2012) 85–88.
[46] N. Yabuuchi, H. Yoshida, S. Komaba, Electrochemistry 80 (2012) 716–719.
[47] P. Vassilaras, X.H. Ma, X. Li, G. Ceder, J. Electrochem. Soc. 160 (2013) A207–A211.

[48] M. Sathiya, K. Hemalatha, K. Ramesha, J.M. Tarascon, A.S. Prakash, Chem. Mater. 24 (2012) 1846–1853.
[49] H. Yoshida, N. Yabuuchi, S. Komaba, Electrochem. Commun. 34 (2013) 60–63.
[50] B.M. de Boisse, D. Carlier, M. Guignard, C. Delmas, J. Electrochem. Soc. 160 (2013) A569–A574.
[51] J. Zhao, J. Xu, D.H. Lee, N. Dimov, Y.S. Meng, S. Okada, J. Power Sources 264 (2014) 235–239.
[52] Z. L. Jian, H.J. Yu, H.S. Zhou, Electrochem. Commun. 34 (2013) 215–218.
[53] S.P. Ong, V.L. Chevrier, G. Hautier, A. Jain, C. Moore, S. Kim, X.H. Ma, G. Ceder, Energy Environ. Sci. 4 (2011) 3680–3688.
[54] H.L. Chen, Q. Hao, O. Zivkovic, G. Hautier, L.S. Du, Y.Z. Tang, Y.Y. Hu, H.X. Ma, C.P. Grey, G. Ceder, Chem. Mater. 25 (2013) 2777–2786.
[55] A.K. Padhi, K.S. Nanjundaswamy, J.B. Goodenough, J. Electrochem. Soc. 144 (1997) 1188–1194.
[56] A.K. Padhi, K.S. Nanjundaswamy, C. Masquelier, S. Okada, J.B. Goodenough, J. Electrochem. Soc. 144 (1997) 1609–1613.
[57] Z.L. Gong, Y. Yang, Energy Environ. Sci. 4 (2011) 3223–3242.
[58] J. Xu, D.H. Lee, Y.S. Meng, Funct. Mater. Lett. 6 (2013) 1330001–1–1330001–7.
[59] B.L. Ellis, W.R.M. Makahnouk, Y. Makimura, K. Toghill, L.F. Nazar, Nat. Mater. 6 (2007) 749–753.
[60] K. Zaghib, J. Trottier, P. Hovington, F. Brochu, A. Guerfi, A. Mauger, C.M. Julien, J. Power Sources 196 (2011) 9612–9617.
[61] P. Moreau, D. Guyomard, J. Gaubicher, F. Boucher, Chem. Mater. 22 (2010) 4126–4128.
[62] M. Casas–Cabansa, V.V. Roddatis, D. Saurel, P. Kubiak, J. Carretero–Gonzalez, V. Palomares, P. Serras, T. Rojo, J. Mater. Chem. 22 (2012) 17421–17423.
[63] S.M. Oh, S.T. Myung, J. Hassoun, B. Scrosati, Y.K. Sun, Electrochem. Commun. 22 (2012) 149–152.
[64] T. Shiratsuchi, S. Okada, J. Yamaki, T. Nishida, J. Power Sources 159 (2006) 268–271.
[65] Y.L. Liu, Y.H. Xu, X.G. Han, C. Pallegrinelli, Y.J. Zhu, H.L. Zhu, J.Y. Yang, A.C. Chung, O. Vaaland, C.S. Wang, L.B. Hu, Nano. Lett. 12 (2012) 5664–5668.
[66] P. Barpanda, T. Ye, S. Nishimura, S.C. Chung, Y. Yamada, M. Okubo, H.S. Zhou, A. Yamada, Electrochem. Commun. 24 (2012) 116–119.

[67] P. Barpanda, G. Liu, C.D. Ling, M. Tamaru, M. Avdeev, S.C. Chung, Y. Yamada, A. Yamada, Chem. Mater. 25 (2013) 3480–3487.

[68] P. Barpanda, T. Ye, M. Avdeev, S.C. Chung, A. Yamada, J. Mater. Chem. A 1 (2013) 4194–4197.

[69] P. Barpanda, J.C. Lu, T. Ye, M. Kajiyama, S.C. Chung, N. Yabuuchi, S. Komaba, A. Yamada, RSC Adv. 3 (2013) 3857–3860.

[70] H. Kim, R.A. Shakoor, C. Park, S.Y. Lim, J.S. Kim, W. Cho, K. Miyasaka, R. Kahraman, Y. Jung, J. W. Choi, Adv. Funct. Mater. 23 (2013) 1147–1155.

[71] K.H. Ha, S.H. Woo, D. Mok, N.S. Choi, Y. Park, S.M. Oh, Y. Kim, J. Kim, J. Lee, L.F. Nazar, K.T. Lee, Adv. Energy Mater. 3 (2013) 770–776.

[72] T. Honma, N. Ito, T. Togashi, A. Sato, T. Komatsu, J. Power Sources 227 (2013) 31–34.

[73] P. Barpanda, S. Nishimura, A. Yamada, Adv. Energy Mater. 2 (2012) 841–859.

[74] H. Kim, I. Park, D.H. Seo, S. Lee, S.W. Kim, W.J. Kwon, Y.U. Park, C.S. Kim, S. Jeon, K. Kang, J. Am. Chem. Soc. 134 (2012) 10369–10372.

[75] H. Kim, I. Park, S. Lee, H. Kim, K.Y. Park, Y.U. Park, H. Kim, J. Kim, H.D. Lim, W.S. Yoon, K.Kang, Chem. Mater. 25 (2013) 3614–3622.

[76] K. Saravanan, C.W. Mason, A. Rudola, K.H. Wong, P. Balaya, Adv. Energy Mater. 3 (2013) 444–450.

[77] Z.L. Jian, W.Z. Han, X. Lu, H.X. Yang, Y.S. Hu, J. Zhou, Z.B. Zhou, J.Q. Li, W. Chen, D.F. Chen, L.Q. Chen, Adv. Energy Mater. 3 (2013) 156–160.

[78] Y.H. Jung, C.H. Lim, D.K. Kim, J. Mater. Chem. A 1 (2013) 11350–11354.

[79] J.B. Goodenough, H.Y. Hong, J.A. Kafalas, Mater. Res. Bull. 11 (1976) 203–220.

[80] K. Chihara, A. Kitajou, I.D. Gocheva, S. Okada, J. Yamaki, J. Power Sources 227 (2013) 80–85.

[81] P. Serras, V. Palomares, A. Goni, I.G. de Muro, P. Kubiak, L. Lezama, T. Rojo, J. Mater. Chem. 22 (2012) 22301–22308.

[82] R.A. Shakoor, D.H. Seo, H. Kim, Y.U. Park, J. Kim, S.W. Kim, H. Gwon, S. Lee, K. Kang, J. Mater. Chem. 22 (2012) 20535–20541.

[83] W.S. Cong, X.B. Ji, Z.P. Wu, Y.C. Yang, Z. Zhou, F.Q. Li, Q.Y. Chen, C.E. Banks, J. Power Sources 256 (2014) 258–263.

[84] Y.U. Park, D.H. Seo, H.S. Kwon, B. Kim, J. Kim, H. Kim, I. Kim, H.I. Yoo, K. Kang, J. Am. Chem. Soc. 135 (2013) 13870–13878.

[85] Y. Kawabe, N. Yabuuchi, M. Kajiyama, N. Fukuhara, T. Inamasu, R. Okuyama, I. Nakai, S. Komaba, Electrochem. Commun. 13 (2011) 1225–1228.

[86] S.W. Kim, D.H. Seo, H. Kim, K.Y. Park, K. Kang, Phys. Chem. Chem. Phys. 14 (2012) 3299–3303.

[87] A. Langrock, Y.H. Xu, Y.H. Liu, S. Ehrman, A. Manivannan, C.S. Wang, J. Power Sources 223 (2013) 62–67.

[88] N. Recham, J.N. Chotard, L. Dupont. K. Djellab, M. Armand, J.M. Tarascon, J. Electrochem. Soc. 156 (2009) A993–A999.

[89] C. Masquelier, L. Croguennec, Chem. Rev. 113 (2013) 6552–6591.

[90] R. Dominko, M. Bele, M. Gaberscek, A. Meden, M. Remskar, J. Jamnik, Electrochem. Commun. 8 (2006) 217–222.

[91] A. Nyten, A. Abouimrane, M. Armand, T. Gustafsson, J.O. Thomas, Electrochem. Commun. 7 (2005) 156–160.

[92] T. Muraliganth, K.R. Stroukoff, A. Manthiram, Chem. Mater. 22 (2010) 5754–5761.

[93] D. Rangappa, K.D. Murukanahally, T. Tomai, A. Unemoto, I. Honma, Nano Lett. 12 (2012) 1146–1151.

[94] H. Duncan, A. Kondamreddy, P.H.J. Mercier, Y. Le Page, Y. Abu–Lebdeh, M. Couillard, P.S. Whitfield, I.J. Davidson, Chem. Mater. 23 (2011) 5446–5456.

[95] D.A. Stevens, J.R. Dahn, J. Electrochem. Soc. 148 (2001) A803–A811.

[96] D.A. Stevens, J.R. Dahn, J. Electrochem. Soc. 147 (2000) A1271–A1273.

[97] G.E. Pascal, M. Fouletier, Solid State Ionics 28 (1988) 1172–1175.

[98] V.L. Chevrier, G. Ceder, J. Electrochem. Soc. 158 (2011) A1011–A1014.

[99] M.M. Doeff, Y.P. Ma, S.J. Visco, L.C. Dejonghe, J. Electrochem. Soc. 140 (1993) L169–L179.

[100] R. Alcantara, J.M. Jimenez–Mateos, P. Lavela, J.L. Tirado, Electrochem. Commun. 3 (2001) 639–642.

[101] P. Thomas, D. Billaud, Electrochim. Acta 47 (2002) 3303–3307.

[102] S. Komaba, W. Murata, T. Ishikawa, N. Yabuuchi, T. Ozeki, T. Nakayama, A. Ogata, K. Gotoh, K. Fujiwara, Adv. Funct. Mater. 21 (2011) 3859–3867.

[103] K. Gotoh, T. Ishikawa, S. Ishikawa, S. Shimadzu, N. Yabuuchi, S. Komaba, K. Takeda, A. Goto, K. Deguchi, S. Ohki, H. Hashi, T. Shimizu, H. Ishida, J. Power Sources 225 (2013) 137–140.

[104] S. Wenzel, T. Hara, J. Janek, P. Adelhelm, Energy Environ. Sci. 4 (2011) 3342–3345.

[105] K. Tang, L.J. Fu, R.J. White, L.H. Yu, M.M. Titirici, M. Antonietti, J. Maier, Adv. Energy Mater. 2 (2012) 873–877.
[106] Y.L. Cao, L.F. Xiao, M.L. Sushko, W. Wang, B. Schwenzer, J. Xiao, Z.M. Nie, L.V. Saraf, Z.G. Yang, J. Liu, Nano. Lett. 12 (2012) 3783–3787.
[107] S. Komaba, Y. Matsuura, T. Ishikawa, N. Yabuuchi, W. Murata, S. Kuze, Electrochem. Commun. 21 (2012) 65–68.
[108] Y.M. Lin, P.R. Abel, A. Gupta, J.B. Goodenough, A. Heller, C.B. Mullins, ACS. Appl. Mater. Interfaces 5 (2013) 8273–8277.
[109] Y.H. Xu, Y.J. Zhu, Y.H. Liu, C.S. Wang, Adv. Energy Mater. 3 (2013) 128–133.
[110] D.W. Su, H.J. Ahn, G.X. Wang, Chem. Commun. 49 (2013) 3131–3133.
[111] L. Wu, X.H. Hu, J.F. Qian, F. Pei, F.Y. Wu, R.J. Mao, X.P Ai, H.X. Yang, Y.L. Cao, Energy Environ. Sci. 7 (2014) 323–328.
[112] L.F. Xiao, Y.L. Cao, J. Xiao, W. Wang, L. Kovarik, Z.M. Nie, J. Liu, Chem. Commun. 48 (2012) 3321–3323.
[113] Y. Kim, Y. Park, A. Choi, N.S. Choi, J. Kim, J. Lee, J.H. Ryu, S.M. Oh, K.T. Lee, Adv. Mater. 25 (2013) 3045–3049.
[114] A. Darwiche, C. Marino, M.T. Sougrati, B. Fraisse, L. Stievano, L. Monconduit, J. Am. Chem. Soc. 134 (2012) 20805–20811.
[115] J.B. Goodenough, Y. Kim, Chem. Mater. 22 (2010) 587–603.
[116] D. Yaakov, Y. Gofer, D. Aurbach, I.C. Halalay, J. Electrochem. Soc. 157 (2010) A1383–A1391.
[117] K. Xu, Chem. Rev. 104 (2004) 4303–4417.
[118] A. Ponrouch, E. Marchante, M. Courty, J.M. Tarascon, M.R. Palacin, Energy Environ. Sci. 5 (2012) 8572–8583.
[119] A. Ponrouch, R. Dedryvere, D. Monti, A.E. Demet, J.M.A. Mba, L. Croguennec, C. Masquelier, P. Johansson, M.R. Palacin, Energy Environ. Sci. 6 (2013) 2361–2369.
[120] K. Kuratani, N. Uemura, H. Senoh, H.T. Takeshita, T. Kiyobayashi, J. Power Sources 223 (2013) 175–182.
[121] S. Komaba, T. Ishikawa, N. Yabuuchi, W. Murata, A. Ito, Y. Ohsawa, ACS. Appl. Mater. Interfaces 3 (2011) 4165–4168.
[122] X. Xia, M.N. Obrovac, J.R. Dahn, Electrochem. Solid–State Lett. 14 (2011) A130–A130.
[123] J.F. Whitacre, A. Tevar, S. Sharma, Electrochem. Commun. 12 (2010) 463–466.

[124] Z. Li, D. Young, K. Xiang, W.C. Carter, Y.M. Chiang, Adv. Energy Mater. 3 (2013) 290–294.
[125] C.D. Wessells, S.V. Peddada, R.A. Huggins, Y. Cui, Nano Lett. 11 (2011) 5421–5425.
[126] M. Armand, F. Endres, D.R. MacFarlane, H. Ohno, B. Scrosati, Nat. Mater. 8 (2009) 621–629.
[127] M. Galinski, A. Lewandowski, I. Stepniak, Electrochim. Acta 51 (2006) 5567–5580.
[128] S. Passerini, G.B. Appetecchi, MRS Bull. 38 (2013) 540–547.
[129] L.G. Chagas, D. Buchholz, L.M. Wu, B. Vortmann, S. Passerini, J. Power Sources 247 (2014) 377–383.
[130] D. Monti, E. Jonsson, M.R. Palacin, P. Johansson, J. Power Sources 245 (2014) 630–636.
[131] N. Wongittharom, T.C. Lee, C.H. Wang, Y.C. Wang, J.K. Chang, J. Mater. Chem. A 2 (2014) 5655–5661.
[132] K. Kubota, T. Nohira, T. Goto, R. Hagiwara, Electrochem. Commun. 10 (2008) 1886–1888.
[133] K. Kubota, T. Nohira, R. Hagiwara, J. Chem. Eng. Data 55 (2010) 3142–3146.
[134] K. Kubota, T. Nohira, R. Hagiwara, Electrochim. Acta 66 (2012) 320–324.
[135] R. Hagiwara, K. Tamaki, K. Kubota, T. Goto, T. Nohira, J. Chem. Eng. Data 53 (2008) 355–358.
[136] T. Yamamoto, T. Nohira, R. Hagiwara, A. Fukunaga, S. Sakai, K. Nitta, S. Inazawa, J. Power Sources 217 (2012) 479–484.
[137] T. Yamamoto, T. Nohira, R. Hagiwara, A. Fukunaga, S. Sakai, K. Nitta, S. Inazawa, J. Power Sources 237 (2013) 98–103.
[138] C. Chen, K. Matsumoto, T. Nohira, R. Hagiwara, Y. Orikasa, Y. Uchimoto, J. Power Sources 246 (2014) 783–787.
[139] T. Nohira, T. Ishibashi, R. Hagiwara, J. Power Sources 205 (2012) 506–509.
[140] Q. Zhou, W.A. Henderson, G.B. Appetecchi, M. Montanino, S. Passerini, J. Phys. Chem. B 112 (2008) 13577–13580.
[141] C. Chen, K. Matsumoto, T. Nohira, C. Ding, T. Yamamoto, R. Hagiwara, Electrochim. Acta 133 (2014) 583–588.
[142] C. Chen K. Matsumoto, T. Nohira, R. Hagiwara, Submitted
[143] C. Chen, K. Matsumoto, T. Nohira, R. Hagiwara, Electrochem. Commun. 45 (2014) 63–66.

Table 1–1 The comparison of energy and power characteristics of potential batteries for grid–scale energy storage applications [1, 2].

Battery type	Voltage Range (V)	Operating Temp. (K)	Energy Density (Wh/L)	Specific Energy (Wh/kg)	Specific Power (W/kg)	Cycleability
Lithium ion $LiCoO_2$–C	2.5–4.2	248–313	200–250	120–160	200–300	300–1000
Lithium ion $LiFePO_4$–C	2.5–3.5	248–313	120–150	80–90	200–300	1500–2000
Lithium metal–polymer	2.4–4.0	–	100–110	100–110	130–170	600
Sodium–sulfur	1.8–2.1	573–623	70–150	60–120	15–70	4000
Sodium–metal chloride	2.6	573–623	20–140	50–100	30–150	3000
Lead acid	1.8–2.1	233–333	60–75	30–40	60–110	100–500
Nickel–cadmium	0.8–1.3	263–318	130–150	40–60	40–100	2000
Nickel–metal hydride	0.9–1.3	–	250–300	70–100	70–200	1000
Vanadium redox flow	1.1–1.6	283–313	10–20	10–20	1–4	5000

Table 1–2 Main applications, advantages and limitations of different battery technologies [3, 23].

Battery type	Main application	Advantages	Limitations
Lithium ion	Transportation and portable electronics, targets grid–scale	High efficiency High energy density High power	High cost (~\$700 kWh^{-1}) Safety/reliability problems Small temperature range of operation
Sodium–sulfur Sodium–metal chloride	Targets grid–scale storage	High efficiency High energy density	Operating at 573–623 K High production cost Weight and size specification Safety and durability concerns due to fracture of beta–alumina and molten sodium electrode
Lead acid	Current automobile and industrial application, backup power	Least expensive	Short cycle life High maintenance Low energy density
Redox flow	Targets grid–scale storage	MW storage system Potential long cycle life	High cost Unknown long term durability Capacity loss issues

Table 1–3 The comparison between Na and Li [31–33].

	Na	Li
E^0 (vs. SHE)	–2.71 V	–3.04 V
Atomic weight	23 g mol^{-1}	6.9 g mol^{-1}
Ionic radius	1.02 Å	0.76 Å
A–O coordination	Octahedral, prismatic	Octahedral, tetrahedral
Melting point of metal	371 K	454 K
Price of carbonates	150 USD T^{-1}	5000 USD T^{-1}
Crustal abundance	23000 mg kg^{-1}	20 mg kg^{-1}
Distribution	Evenly worldwide	70% in South America

Table 1–4 Selected layered oxides that have been investigated as positive electrode for Na secondary batteries [39, 40, 41, 44, 45, 47–51].

Active material	Voltage range (V)	Reversible capacity (mAh g^{-1})	Current rate (mA g^{-1})	Cycleability
O3–$NaCrO_2$ [39, 44, 45]	2.0–3.6	120	25	Moderate
O3–$NaNiO_2$[47]	1.25–3.75	120	23.5	Good
O3–$Na[Ni_{0.5}Mn_{0.5}]O_2$ [40]	2.2–3.8	125	4.8	Moderate
O3–$Na[Ni_{0.33}Mn_{0.33}Co_{0.33}]O_2$ [48]	2.0–3.75	120	24	Good
O3–$Na[Fe_{0.5}Co_{0.5}]O_2$ [49]	2.5–4.0	160	12	Good
P2–$Na_{0.67}[Fe_{0.5}Mn_{0.5}]O_2$ [41, 50]	1.5–4.3	190	12	Poor
P2–$Na_{0.67}[Fe_{0.33}Mn_{0.66}]O_2$ [50, 51]	1.5–4.3	191	12	Poor

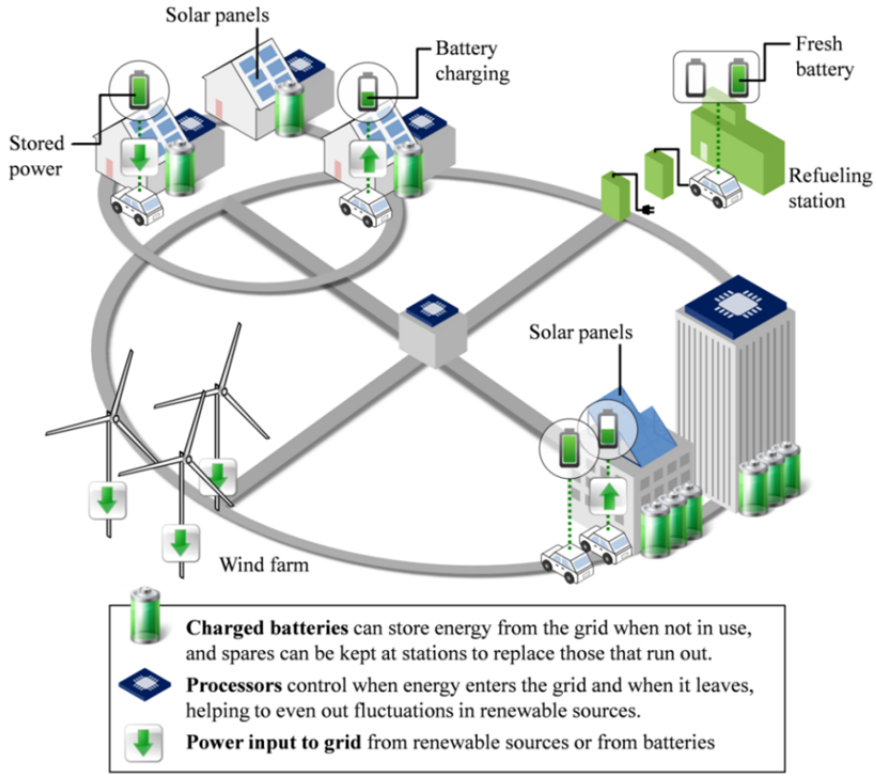

Fig. 1–1 An illustration for the smart grid concept. [8, 9]

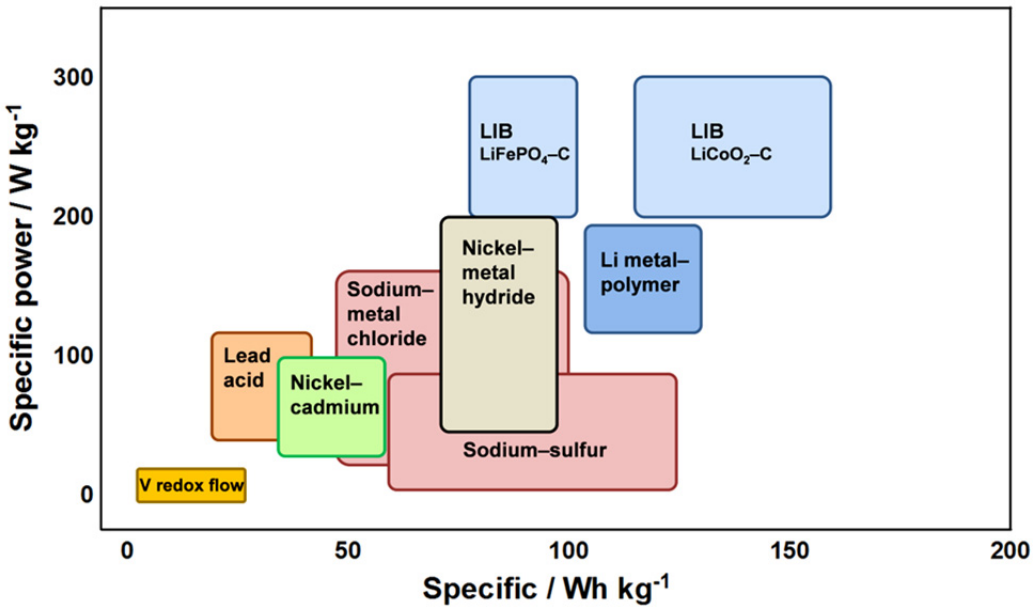

Fig. 1–2 Gravimetric energy and power densities for presently available batteries being considered for grid scale energy storage applications [2].

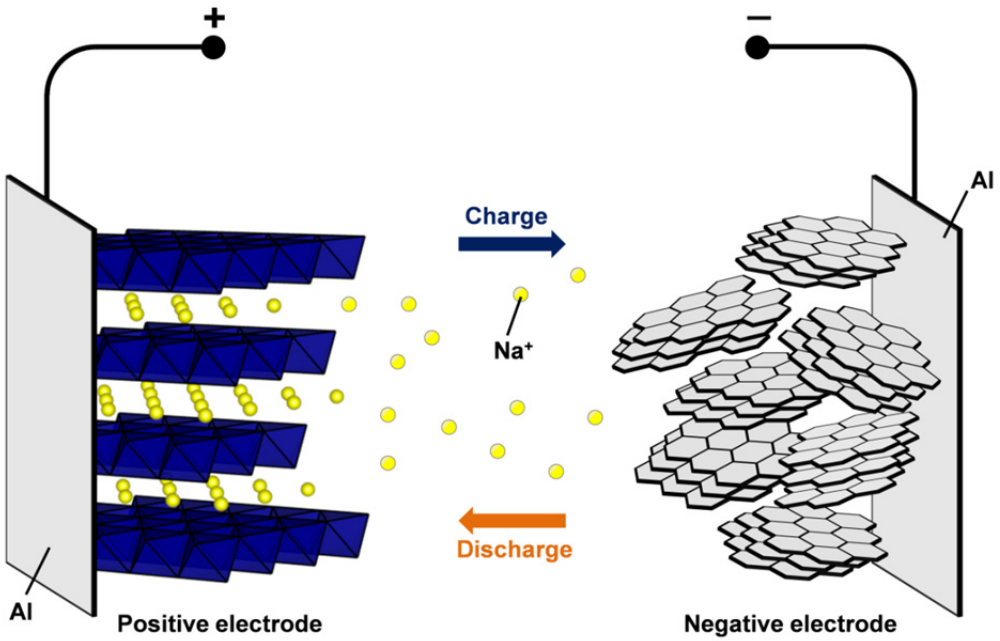

Fig. 1–3 A schematic illustration depicting the working principle of rocking–chair type Na secondary batteries [33, 102].

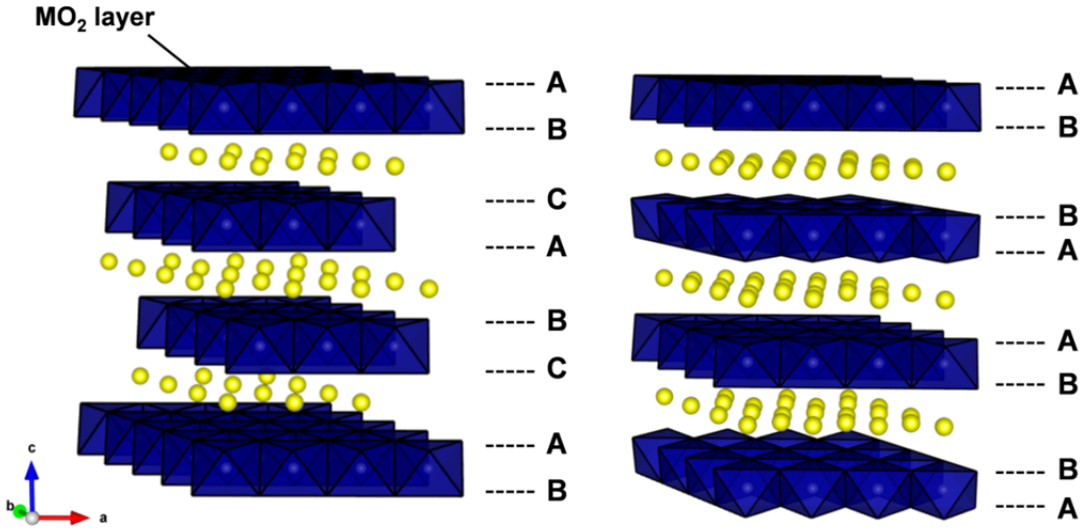

Fig. 1–4 The crystalline structure of O3–type (left) and P2–type (right) layered oxide $NaMO_2$. Symbols A, B and C in the schematics represent the three different oxygen layers [41].

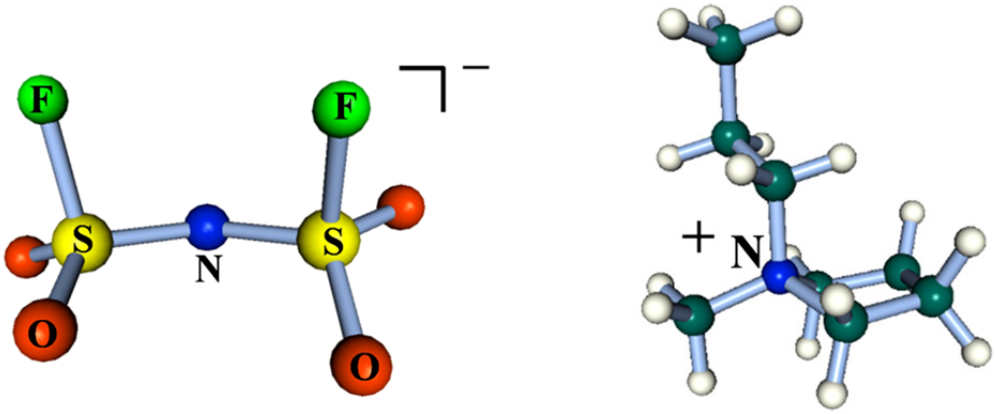

Fig. 1–5 The structures of FSA anions (left) and C_3C_1pyrr cations (right).

Chapter 2

Experimental

2.1 Apparatus

Air– and moisture–sensitive materials were handled in a glove box (MDB–4B, Miwa Manufacturing Co., Ltd.) with a gas–refining instrument filled with dried and deoxygenated argon gas (99.995%). The dew point (*ca*. 163 K) and concentration of oxygen (*ca*. 1 ppm) were always monitored during the experiment.

For the purposes of drying the materials and impregnation of ionic liquids into a separator and electrodes, a vacuum line and vessels were used. Their schematic illustrations are shown in Figs. 2–1 and 2–2. The main line was made of corrosion–resistant stainless steel pipes (SUS316, 1/2 inch o.d.) connected by the stainless unions and valves with a Kel–F (polychlorotrifluoroethylene) tip (Swagelok Co.). Metal and PFA (tetrafluoroethylene–perfluoroalkylvinylether copolymer) tube (1/4 inch o.d.) were used as the connecting parts to a vacuum vessel. The line was connected to a rotary vacuum pump through a Pyrex glass cold trap. The typical degree of vacuum in this system was below 5 Pa. The pressure was monitored by Bourdon and Pirani gauges.

2.2 Electrochemical measurements

2.2.1 Ionic liquids electrolyte

The ionic liquid (IL) electrolytes used in this study consist of alkali metal cations or *N*–methyl–*N*–propylpyrrolidinium (C_3C_1pyrr) cations and bis(fluorosulfonyl)amide (FSA) anions. Na[FSA] (Mitsubishi Materials Electronic Chemicals CO., Ltd., purity >99%) and K[FSA] (Mitsubishi Materials Electronic Chemicals CO., Ltd., purity >99%) were purchased and dried under vacuum at 353 K and 333 K for 48 h, respectively. [C_3C_1pyrr][FSA] (Kanto Chemical Co., Inc., purity >99.9%) were dried under vacuum for 24 h at 333 K prior to use. The IL mixtures, Na[FSA]–K[FSA] (56:44 molar ratio) and Na[FSA]–[C_3C_1pyrr][FSA], were utilized as the electrolyte. Contents of impurities in the electrolytes such as metallic cations or halide anions were determined to be less than 10 ppm by ICP–AES (iCAP6500 DUO, Thermo Fisher Scientific Inc.) and ion chromatography analysis (Dionex ICS–3000, Thermo Fisher Scientific Inc.). Water content of all electrolytes was determined to be less than 50 ppm by the Karl Fischer titration method (ADP–611, Kyoto Electronics Manufacturing Co., Ltd.).

2.2.2 Electrodes and cell configurations

The positive electrodes were fabricated by mixing as–synthesized $NaCrO_2$ with acetylene black (AB, DENKA BLACK HS–100, Denka Co., Ltd.) as a conductive additive and polytetrafluoroethylene (PTFE; Aldrich) or polyvinylidenedifluoride (PVdF, KF POLYMER

L#1120, Kureha Battery Materials Japan Co., Ltd.) as a binder at a fixed weight ratio in *N*–methyl–2–pyrrolidone (Kishida Chemical Co., Ltd., >99.5%) using a dispersion mixer (AR–100, THINKY Corp.). The negative electrode active material hard carbon (HC, Carbotron P, Kureha Battery Materials Japan Co., Ltd.) and polyamide–imide binder (NIPPON KODOSHI Corp.) were mixed in *N*–methyl–2–pyrrolidone at a weight ratio of 96:4 using a dispersion mixer. The obtained slurry was coated onto an aluminum foil current collector and pressed by roller press. Metallic sodium discs (Aldrich, purity 99.95%) pressed onto aluminum or nickel current collectors or HC electrodes were used as negative electrodes. Borosilicate glass microfiber filters (Whatman GF/A, thickness of 260 μm) or polyolefin membrane (NPS050, Nippon Sheet Glass Co., Ltd., thickness of 50 μm) were used as the separators and soaked with Na[FSA]–K[FSA] or Na[FSA]–[C_3C_1pyrr][FSA] electrolyte under vacuum at 363 K and 298 K, respectively, for 12 h to achieve full impregnation. Since Na[FSA]–K[FSA] is solid at room temperature, a customized two–electrode cell (Tomcell Japan Co., Ltd.) was used to favor the cell assembling. A schematic illustration of the two–electrode cell is shown in Fig. 2–4. For the cells utilized Na[FSA]–[C_3C_1pyrr][FSA] electrolyte, conventional CR2032 type coin cells with PFA gasket (Hohsen Corp.) were used. All cells were assembled in the Ar–filled glove box.

2.2.3 Galvanostatic charge–discharge test

The specific capacity of the as–synthesized $NaCrO_2$ and hard carbon was evaluated by

galvanostatic charge–discharge test conducted by a computer–controlled charge–discharge unit (ABE 1024–05R1, Electrofield Corp). The cells were aged for 2 h before charge–discharge to ensure full absorption of the electrolyte in the electrode and also to reach a thermal equilibrium. The current density during galvanostatic charge–discharge cycling was maintained constant for both charge and discharge. The operating temperature was controlled by thermostatic chamber (PVH–210, ESPEC Corp.). All of the specific capacities in the following chapters are calculated based on the mass of active material.

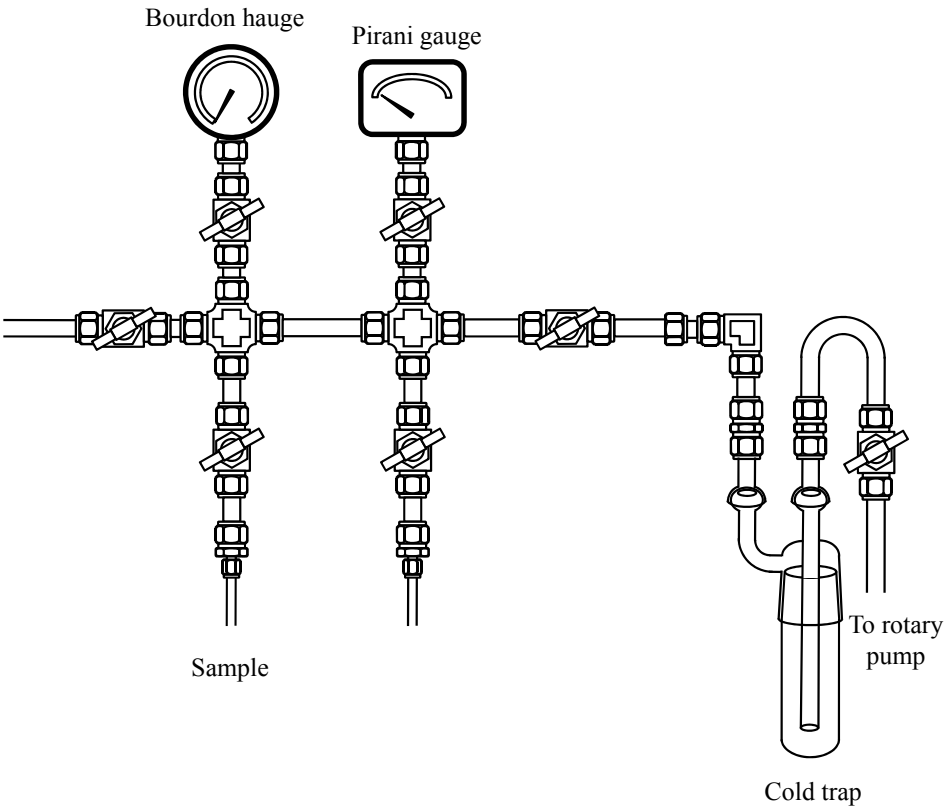

Fig. 2–1 A schematic illustration of a vacuum line.

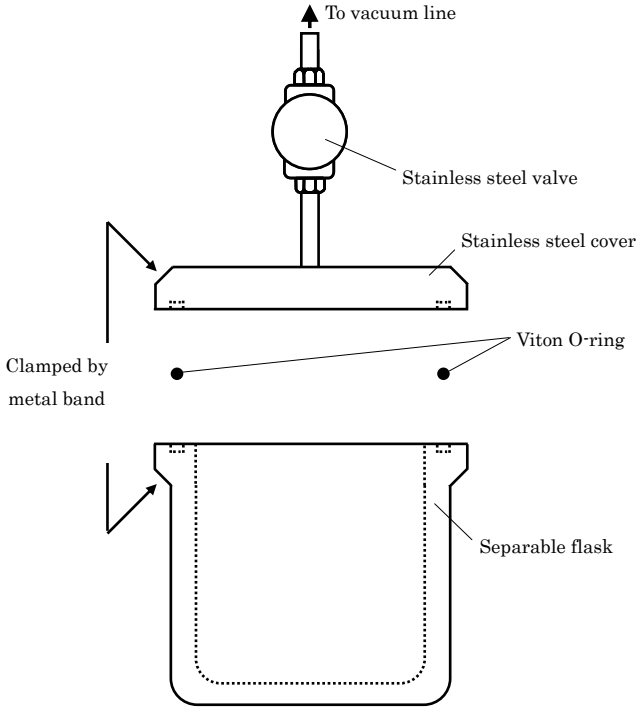

Fig. 2–2 A schematic illustration of a vessel for vacuum drying.

Chapter 3

$NaCrO_2$ positive electrode in Na[FSA]–K[FSA] ionic liquid

3.1 Introduction

Ionic liquids have been studied as safe electrolytes for lithium ion batteries because they generally provide negligibly low volatility, nonflammability, and high thermal and electrochemical stability. More particularly, intense interest has been shown towards room–temperature ionic liquids (RTILs) over the past decade. However, low ionic conductivity, high viscosity and, in some cases, high cost has perhaps prevented RTILs from being of practical use. It is our claim that there are many advantages to the use of molten salts (or ionic liquids in original definition [1, 2]) at intermediate temperatures (e.g., 373–473 K) [3]. Their advantages are remarkable when they are used as electrolytes for large–scale lithium [4] and sodium [5, 6] secondary batteries, including improved ionic conductivity, decreased viscosity, enhanced reaction rate, the possibility of new electrode active materials, a simplified cooling system, and the efficient use of generated heat.

Hagiwara et al. first focused on salts consisting of alkali metal cations and the bis(trifluoromethylsulfonyl)amide (TFSA) anion, M[TFSA]s (M = Li, Na, K, Rb, or Cs), and reported that they have melting points in the range of 400–540 K. These melting points are significantly lowered by mixing two or three of these salts in prescribed compositions [7, 8].

Such mixed salts of M[TFSA] possess wide electrochemical windows of approximately 5 V [9]. Hagiwara et al. have reported that the Li[TFSA]–K[TFSA]–Cs[TFSA] system shows promise as an electrolyte for lithium metal secondary batteries, and that a Li/$LiFePO_4$ cell exhibits good cycle performance at 423 K [4]. Recently, Hagiwara et al. also reported that a Na/Na[TFSA]–Cs[TFSA]/$NaCrO_2$ cell shows promise as a sodium secondary battery that can operate at around 423 K [5]. Furthermore, in order to develop salts with lower melting points, we investigated M[FSA] ionic liquids that consist of alkali metal cations and bis(fluorosulfonyl)amide (FSA) anion, and found that binary and ternary M[FSA]s (M = Li, Na, K, Rb, or Cs) mixtures possess lower melting points than those of the single constituent salts [10–13]. Table 3–1 shows the eutectic compositions and temperatures of binary M[FSA] salt mixtures [12]. Although the melting points of single M[FSA] salts are relatively high (typically above 370 K), it is possible to lower the melting points to around 330 K through mixing. Hagiwara et al. pointed out that the Na[FSA]–K[FSA] system is expected to operate as an electrolyte for a sodium secondary battery at 353 K [10]. It should be noted that both Na[FSA] and K[FSA] are completely inorganic compounds and as such are expected to be synthesized with a reasonably low cost because they do not contain expensive organic cations. Furthermore, FSA anions can be synthesized without using the expensive electrofluorination process.

In this Chapter, the author measured the viscosity, ionic conductivity, and density of a

Na[FSA]–K[FSA] eutectic melt (xNa[FSA] = 0.56 and xK[FSA] = 0.44) at 333–398 K since these are the fundamental electrolyte properties for use in a sodium secondary battery. The relationship between viscosity and molar conductivity was discussed from the Walden plot. The electrochemical window of the melt was investigated to reveal its accessible potential range. The stability of aluminum, which is used as a current collector of the positive electrode, was also studied. Finally, a Na/Na[FSA]–K[FSA]/$NaCrO_2$ cell was constructed and its charge–discharge properties investigated at 353 K. Here in, $NaCrO_2$ was selected as a positive electrode active material because it had previously been reported to exhibit good cycle performance at both room [14] and high temperature [5].

3.2. Experimental

Na[FSA] and K[FSA] (Mitsubishi Materials Electronic Chemicals, purity >99.0%) were purchased and dried as described in Chapter 2. Then, they were mixed into a eutectic composition (xNa[FSA] = 0.56 and xK[FSA] = 0.44). Density was measured using the Archimedes method by measuring the weight change of a volume–known nickel ball immersed in the melt. Viscosity was measured by a viscometer (Brookfield Engineering Laboratories, DV–II+ PRO). Ionic conductivity was measured by electrochemical impedance spectroscopy using a calibrated cell with two platinum plate electrodes and a potentiostat/galvanostat/frequency response analyzer (Ivium Technologies, IviumStat). The

cell constant was determined with a standard KCl aqueous solution. The density, viscosity, and ionic conductivity were measured from 333 K to 398 K at intervals of 5 K.

Electrochemical measurements were performed with a three–electrode system constructed in a Pyrex® beaker cell in an argon–filled glove box. The electrochemical window of the eutectic Na[FSA]–K[FSA] melt was measured by cyclic voltammetry. A copper plate disk (6 mm in diameter and 0.1 mm in thickness) and a glassy carbon disk (3 mm in diameter) were used as working electrodes to investigate the cathode and anode limits, respectively. Sodium foils were used for counter and reference electrodes. The scan rate for the cyclic voltammetry was 10 mV s^{-1}. Galvanostatic electrolysis was performed to obtain the deposit for the identification of the reactions at the cathode limit. The deposited substance was analyzed by means of differential scanning calorimetry (DSC) and X–ray diffraction (XRD) analysis. The stability of aluminum was investigated by cyclic voltammetry and potentiostatic electrolysis. An aluminum plate (15 mm in diameter and 0.1 mm in thickness) was used as a working electrode.

The charge–discharge property of the Na/Na[FSA]–K[FSA]/$NaCrO_2$ cell was measured by a two–electrode cell as described in Chapter 2. The positive electrode active material, $NaCrO_2$, was prepared by a solid phase method. Equimolar Na_2CO_3 and Cr_2O_3 were mixed and then reacted at 1123 K for 5 h under Ar flow. The $NaCrO_2$ thus prepared was well mixed with acetylene black (Wako Pure Chemical Industries, purity >99.99%) and PTFE

(Sigma–Aldrich) at a weight ratio of 85/10/5 using a mortar and pestle. The resultant mixture was then pressed onto an aluminum mesh current collector at 300 MPa. Charge–discharge tests were conducted at a constant current rate of 15–150 mA $(g–NaCrO_2)^{-1}$. All measurements were conducted in an argon glove box with a gas–refining instrument. The cell temperature, 353 K, was controlled by a heater with a temperature controller.

3.3 Results and discussion

3.3.1 Physicochemical properties of Na[FSA]–K[FSA]

Fig. 3–1 shows an Arrhenius plot of viscosity for the eutectic Na[FSA]–K[FSA] melt. The viscosity was 435 cP at 363 K. Distinct upward trends in the curvatures are observed at lower temperatures. In such a case, the following Vogel–Tamman–Fulcher (VTF) equation [15] is frequently applied:

$$\eta(T) = A_\eta \sqrt{T} \exp\left(\frac{B_\eta}{T - T_{0\eta}}\right) \qquad (1),$$

where A_η, B_η, and $T_{0\eta}$ are constants that are determined empirically. $T_{0\eta}$ is called the "ideal glass transition temperature." The viscosity of the Na[FSA]–K[FSA] melt fitted well (R^2 > 0.999) to the VTF equation with $A_\eta = 3.87 \times 10^{-3}$ cP $K^{-1/2}$, $B_\eta = 1111$ K, and $T_{0\eta} = 235$ K.

Fig. 3–2 shows an Arrhenius plot of ionic conductivity for the eutectic Na[FSA]–K[FSA] melt. The conductivity was measured as 3.3 mS cm^{-1} at 363 K. Slightly downward curvatures are observed at lower temperatures. Similarly to the case of viscosity, such

temperature dependence is described by the following VTF equation [16]:

$$\sigma(T) = \frac{A_\sigma}{\sqrt{T}} \exp\left(-\frac{B_\sigma}{T - T_{0\sigma}} \right) \quad (2),$$

where A_σ, B_σ, and $T_{0\sigma}$ are constants that are determined empirically. The ionic conductivity of the Na[FSA]–K[FSA] melt fitted well ($R^2 > 0.999$) to this VTF equation, with $A_\sigma = 1.02 \times 10^5$ mS cm^{-1} K$^{-1/2}$, $B_\sigma = 887$ K, and $T_{0\sigma} = 243$ K.

The relationship between ionic conductivity and molar conductivity is given by the following equation:

$$\lambda = \sigma \frac{M}{d} \quad (3),$$

where λ is the molar conductivity, d is the density, and M is the average molecular weight of the melt. Fig. 3–3 shows the temperature dependence of the density for the eutectic Na[FSA]–K[FSA] melt. The density was measured as 2.14 g cm^{-3} at 363 K. The density linearly decreased with an increase in temperature, as expressed by the following equation:

$$d \text{ / g cm}^{-3} = 2.43 - 8.08 \text{ x } 10^{-4}\ T \quad (4)$$

Fig. 3–4 shows plots of the logarithmic molar conductivity against the logarithmic reciprocal viscosity for the eutectic Na[FSA]–K[FSA] melt. If the viscosity and conductivity of the electrolyte obey Walden's rule, the product of the molar conductivity and viscosity is a constant [17]:

$$\lambda\eta = \text{const} \quad (5)$$

The interpretation of this equation is that the ionic conductivity of the liquid is governed by

the viscosity. Although all of the plots (see Fig. 3–4) show a straight line, their gradients are slightly lower than unity. This tendency is called "decoupling" the behavior of ionic conductivity from that of viscosity [18, 19]. Thus, in the case of a Na[FSA]–K[FSA] melt, the relationship between molar conductivity and viscosity should be described by the fractional Walden rule that is presented by the following equation [20]:

$$\lambda \eta^{\alpha} = \text{const} \qquad (6),$$

where α is a positive constant smaller than one and inversely proportional to the logarithm of the decoupling index, which indicates the level of decoupling [21]. For the Na[FSA]–K[FSA] melt, α was calculated to be 0.924, thus indicative of decoupling. The straight line, which has a unit gradient and passes through the points for 1 M KCl aqueous solution at 298 K, is called the "ideal" Walden line, as plotted as a dashed line in Fig. 3–4. The plot for the Na[FSA]–K[FSA] melt falls above the dashed line, thus indicating a "super ionic liquid area" where the ionic conductivity exhibits a higher value than that expected from the viscosity.

3.3.2 Electrochemical properties of Na[FSA]–K[FSA]

Fig. 3–5 shows cyclic voltammograms of (a) copper and (b) a glassy carbon electrode in the Na[FSA]–K[FSA] melt at 363 K. A pair of cathodic and anodic currents is observed at 0 V vs. Na/Na^{+} on a copper electrode. These cathodic and anodic currents are interpreted as the deposition of sodium metal and its dissolution, respectively. Galvanostatic electrolysis was performed at –10 mA cm^{-2} in order to identify the reaction at the cathode

limit. As a result, deposits with partial metallic luster were obtained. When the deposits were analyzed by DSC, endothermic peaks were only observed at the melting point of sodium metal, 371 K, as well as the melting point of the eutectic salt, 330 K. Hence, it was confirmed that only sodium metal was deposited at the cathode limit of Na[FSA]–K[FSA]. An anodic current was observed from around 5.2 V vs. Na/Na^+ on a glassy carbon electrode. This anodic current corresponds to the oxidation of FSA anion, though more studies are required to elucidate the detail of this reaction. The electrochemical window of Na[FSA]–K[FSA] melt is determined as 5.2 V at 363 K, with the limiting potentials defined as the potential at a current density of 0.1 mA cm^{-2}. Such a wide electrochemical window is highly desirable as an electrolyte for a battery because high voltage (i.e., high energy density) batteries can be constructed.

3.3.3 Charge–discharge tests of a Na/Na[FSA]–K[FSA]/$NaCrO_2$ cell

Before the charge–discharge experiments, the stability of aluminum, which was used as a current collector of the cathode, was checked by two methods. First, cyclic voltammetry was conducted for an aluminum plate electrode in the potential range of 1.0–5.0 V. Fig. 3–6 shows the measured voltammograms for the 1st, 2nd, and 5th cycles. The currents become smaller as the cycles proceed and are negligibly small in the potential range of 1.0–4.0 V, i.e., where the successive charge–discharge tests were conducted. The surface of the Al plate was

partially discolored after the experiments. Second, the current on an aluminum plate electrode was measured during potentiostatic electrolysis at 4.5 V vs. Na/Na^+. As shown in Fig. 3–7, the current is negligibly small, below 0.1 μA cm^{-2}. Similar electrochemical stability of aluminum to that observed in Li[TFSA]–K[TFSA]–Cs[TFSA] at 423 K [4] is explained by the formation of a passivation film on the aluminum surface. The passivation film is most probably formed by the reaction of Al^{3+} and FSA^-.

Fig. 3–8 shows charge–discharge curves for the 1st, 20th, and 100th cycle for a Na/Na[FSA]–K[FSA]/$NaCrO_2$ cell at the rate of 15 mA $(g–NaCrO_2)^{-1}$ at 353 K. The high and low cut–off voltages were 2.5 V and 3.5 V, respectively. Flat potential plateaus are repeatedly observed at approximately 3.0 V in both charge and discharge curves. The specific discharge capacity reached 77.3 mA h $(g–NaCrO_2)^{-1}$. Fig. 3–9 shows the cycling properties during the charge–discharge tests for 100 cycles. After the 50th cycle, the discharge capacity became almost constant and about 89% of the initial discharge capacity was maintained after 100 cycles. Except for the initial few cycles, the coulombic efficiency was higher than 99.9%. These results indicate that the electrolyte and electrode materials are stable at 353 K. Fig. 3–10 shows the charge–discharge curves at the rate of 15, 37.5, 75, and 150 mA $(g–NaCrO_2)^{-1}$. The shape of the curve did not change, even at the higher rates. This result indicates that no side reaction occurred during the cycles. It is concluded that the Na/Na[FSA]–K[FSA]/$NaCrO_2$ cell is highly promising as a new rechargeable sodium secondary battery

operating at intermediate temperatures.

3.4. Conclusions

Densities, viscosities, ionic conductivities, and electrochemical windows have been measured for the eutectic Na[FSA]–K[FSA] melt. The viscosities and ionic conductivities are well described by VTF equations. The logarithmic molar conductivity is proportional to the logarithmic reciprocal viscosity and obeys the fractional Walden rule. The binary eutectic Na[FSA]–K[FSA] melt possesses a wide electrochemical window of ca. 5.2 V at 363 K. Aluminum is stable as the current collector material for the positive electrode, even at the high–potential region for this melt. A Na/Na[FSA]–K[FSA]/$NaCrO_2$ cell showed excellent cycle performance at 353 K, whereby 89% of the initial discharge capacity was maintained after 100 cycles with coulombic efficiencies of almost 100% at a charge–discharge rate of 15 mA $(g–NaCrO_2)^{-1}$. It is concluded that the binary eutectic Na[FSA]–K[FSA] melt is a promising electrolyte for a sodium secondary battery operating at intermediate temperatures, and that $NaCrO_2$ is a good candidate as a positive electrode active material.

References

[1] J. O'M. Bockris, A. K. N. Reddy, Modern Electrochemistry, Vol. 1, Chap. 6, "Ionic Liquids", Plenum Press, (1970).

[2] K. Ui, M. Ueda, R. Hagiwara, and Y. Mizuhata, Yoyuen oyobi Koon Kagaku, 47 (2004) 114–123. (in Japanese)

[3] T. Nohira, T. Goto, and R. Hagiwara, Yoyuen oyobi Koon Kagaku, 50 (2008) 148–154.

(in Japanese)
[4] A. Watarai, K. Kubota, M. Yamagata, T. Goto, T. Nohira, R. Hagiwara, K. Ui, N. Kumagai, J. Power Sources, 183 (2008) 724–729.
[5] T. Nohira, T. Ishibashi and R. Hagiwara, J. Power Sources, 205 (2012) 506–509.
[6] R. Hagiwara, T. Nohira, A. Fukunaga, S. Sakai, K. Nitta and S. Inazawa, Electrochemistry, 80 (2012) 98–103. (in Japanse).
[7] R. Hagiwara, K. Tamaki, K. Kubota, T. Goto, T. Nohira, J. Chem. Eng. Data, 53 (2008) 355–358.
[8] K. Kubota, T. Nohira, T. Goto, and R. Hagiwara, J. Chem. Eng. Data, 53 (2008) 2144–2147.
[9] K. Kubota, K. Tamaki, T. Nohira, T. Goto, R. Hagiwara, Electrochim. Acta, 55 (2010) 1113–1119.
[10] K. Kubota, T. Nohira, T. Goto, and R. Hagiwara, Electrochem. Commun., 10 (2008) 1886–1888.
[11] K. Kubota, T. Nohira, T. Goto, and R. Hagiwara, ECS Transactions, 16 (24) (2009) 91–98.
[12] K. Kubota, T. Nohira, and R. Hagiwara, J. Chem. Eng. Data, 55 (2010) 3142–3146.
[13] K. Kubota, T. Nohira, and R. Hagiwara, Electrochim. Acta, 66 (2012) 320–324.
[14] S. Komaba, C. Takei, T. Nakayama, A. Ogata, and N. Yabuuchi, Electrochem. Commun., 12 (2010) 355–358.
[15] A.J. Easteal, C.A. Angell, J. Chem. Phys., 56 (1972) 4231–4233.
[16] C.A. Angell, J. Phys. Chem., 68 (1964) 1917–1929.
[17] P. Walden, Z. Phys. Chem., 55 (1906) 207–249.
[18] C.A. Angell, W. Xu, M. Yoshizawa, A. Hayashi, J.P. Belieres, in: H. Ohno (Ed.), Ionic Liquids: The Front and Future of Material Development, High Technology Information, Tokyo, 2003, p. 43 (in Japanese).
[19] C.A. Angell, Wu Xu, M. Yoshizawa, A. Hayashi, J.–P. Belieres, P. Lucas, M. Videa, in: H. Ohno (Ed.), Electrochemical Aspects of Ionic Liquids, Wiley Interscience, 2005 (Chapter 2).
[20] W. Xu, C.A. Angell, Science, 302 (2003) 422–425.
[21] M. Videa, C.A. Angell, J. Phys. Chem. B, 103 (1999) 4185–4190.

Tables

Table 3–1 The eutectic temperatures and compositions of binary MFSA (M=Li, Na, K, Rb, Cs) systems [12].

System	x_{MFSA}	T_m / K
LiFSA–NaFSA	*E*: $x_{LiFSA} = 0.40$, $x_{NaFSA} = 0.60$	349
LiFSA–KFSA	*E*: $x_{LiFSA} = 0.41$, $x_{KFSA} = 0.59$	341
LiFSA–RbFSA	*E*: $x_{LiFSA} = 0.38$, $x_{RbFSA} = 0.62$	337
LiFSA–CsFSA	*E*: $x_{LiFSA} = 0.47$, $x_{CsFSA} = 0.53$	335
NaFSA–KFSA	*E*: $x_{NaFSA} = 0.56$, $x_{KFSA} = 0.44$	334
NaFSA–RbFSA	*E*: $x_{NaFSA} = 0.50$, $x_{RbFSA} = 0.50$	328
NaFSA–CsFSA	*E*: $x_{NaFSA} = 0.47$, $x_{CsFSA} = 0.53$	325
KFSA–RbFSA	*E*: $x_{KFSA} = 0.31$, $x_{RbFSA} = 0.69$	354
KFSA–CsFSA	*E*: $x_{KFSA} = 0.54$, $x_{CsFSA} = 0.46$	336
RbFSA–CsFSA	*E*: $x_{RbFSA} = 0.65$, $x_{CsFSA} = 0.35$	360

Figures

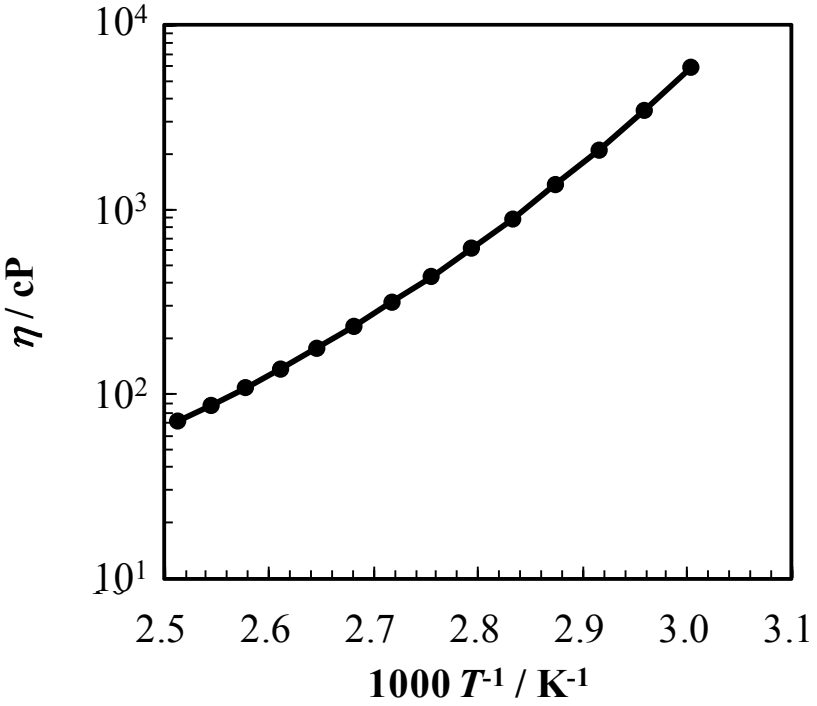

Fig. 3–1 Arrhenius plot of viscosity for a Na[FSA]–K[FSA] eutectic melt.

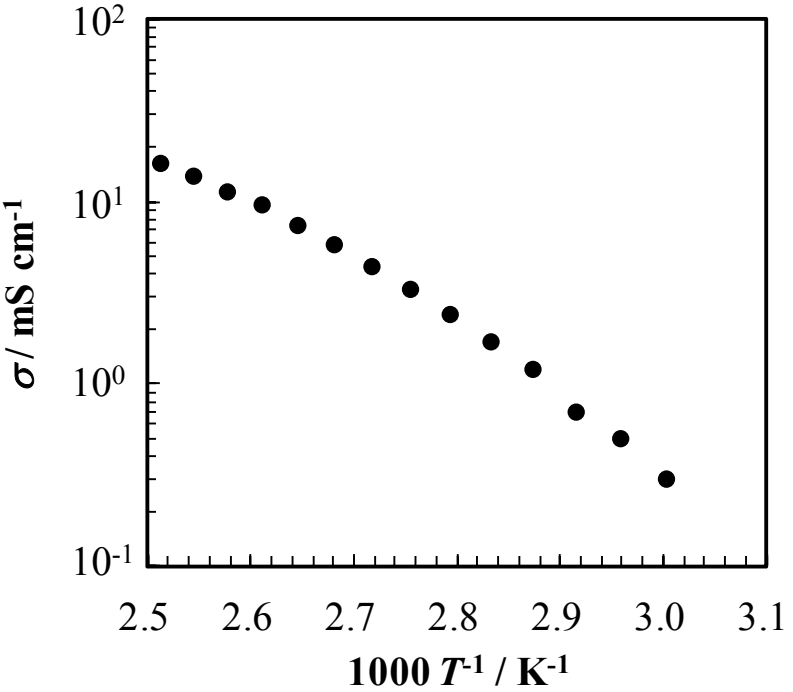

Fig. 3–2 Arrhenius plot of conductivity for a Na[FSA]–K[FSA] eutectic melt.

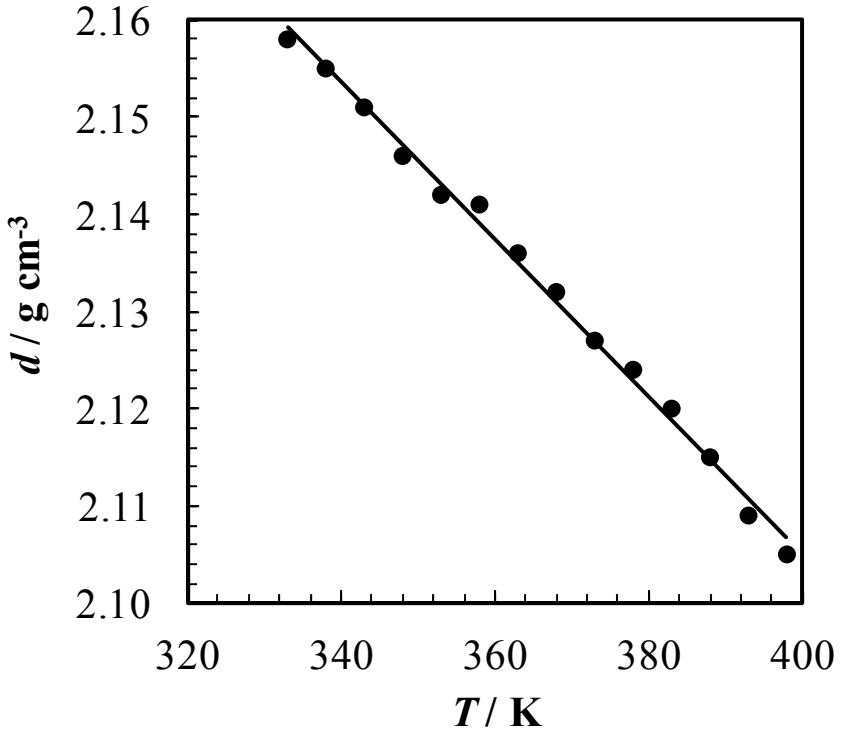

Fig. 3–3 Temperature dependence of density for a Na[FSA]–K[FSA] eutectic melt.

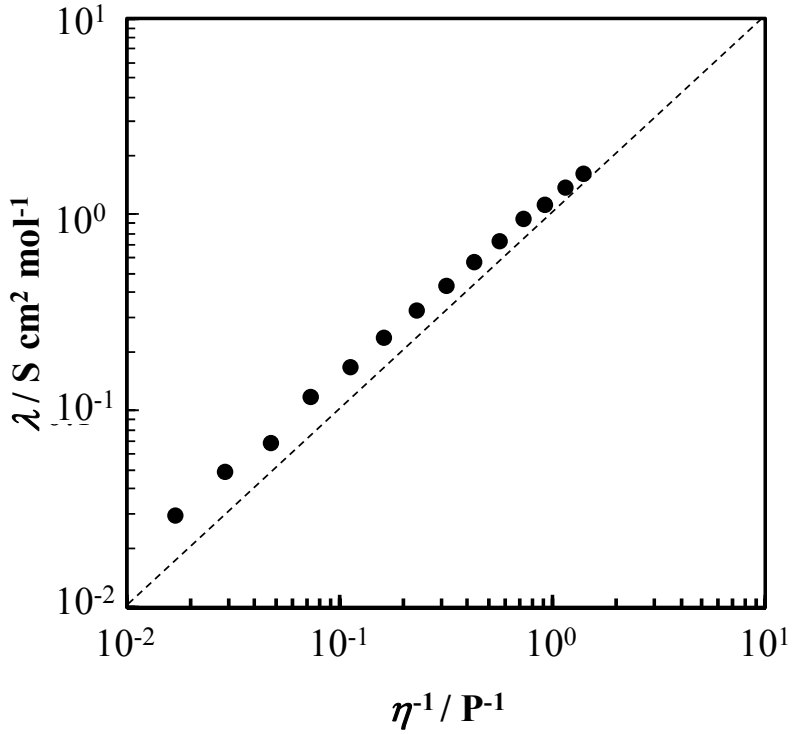

Fig. 3–4 Walden plot of molten Na[FSA]–K[FSA].

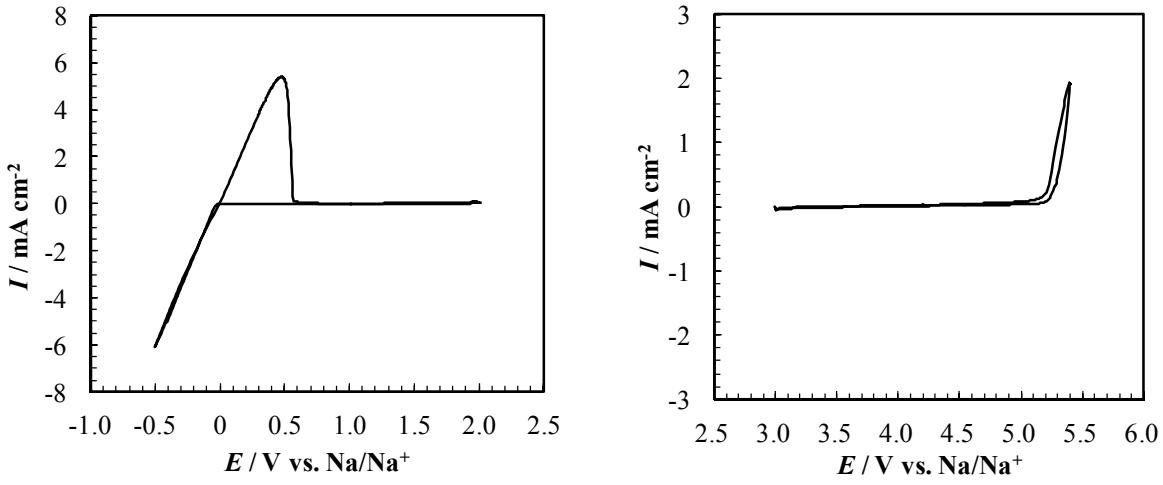

Fig. 3–5 Cyclic voltammograms of (a) a Cu plate electrode and (b) a glassy carbon rod electrode in Na[FSA]–K[FSA] eutectic melt at 363 K. Scan rate: 10 mV s^{-1}.

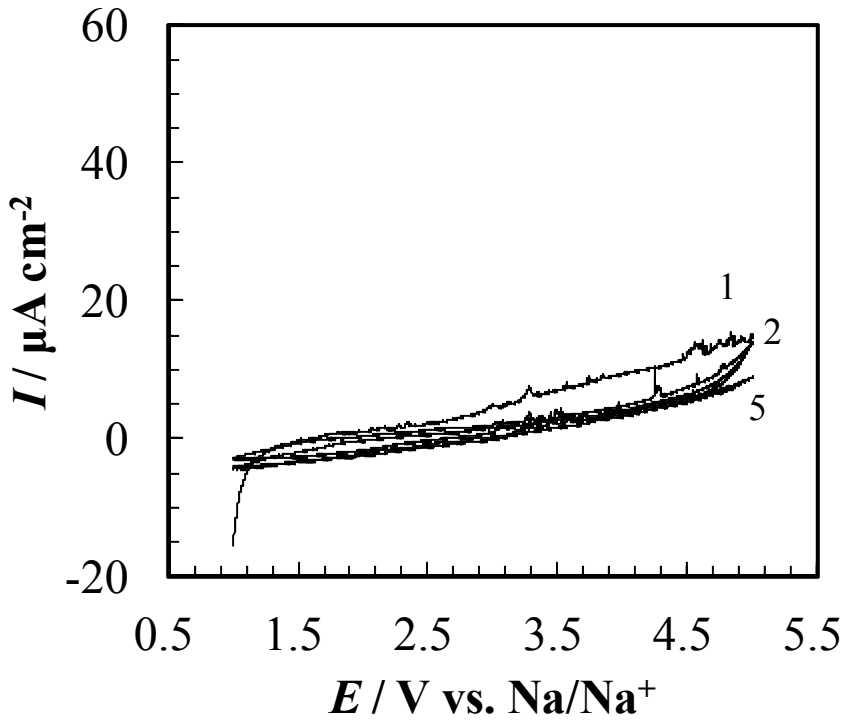

Fig. 3–6 Cyclic voltammograms of an Al plate electrode in Na[FSA]–K[FSA] eutectic melt at 363 K. Scan rate: 10 mV s^{-1}. Cycle number: 1, 2, and 5.

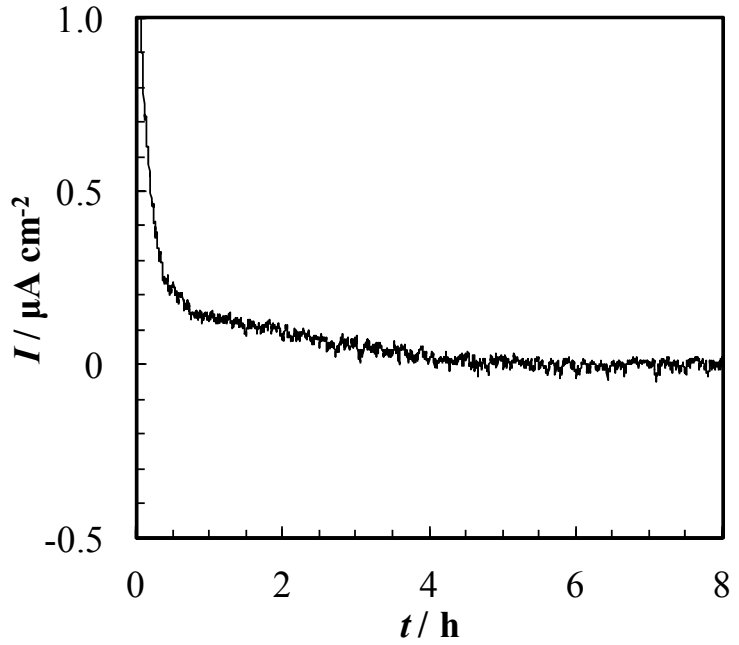

Fig. 3–7 A chronoamperogram of an Al plate electrode in Na[FSA]–K[FSA] eutectic melt at 363 K. Potential: 4.5 V vs. Na/Na^+.

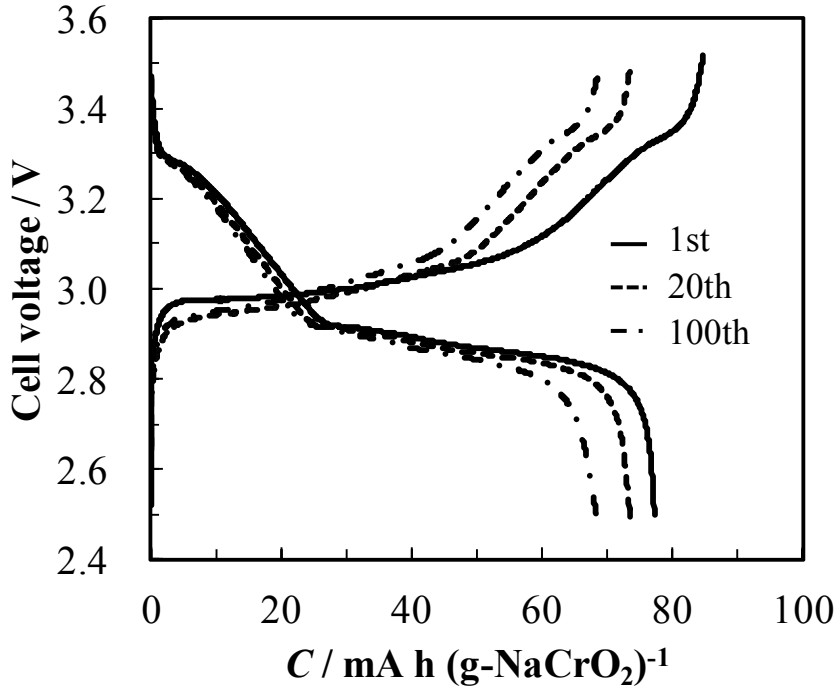

Fig. 3–8 Charge–discharge curves for a Na/Na[FSA]–K[FSA]/$NaCrO_2$ cell at 353 K. Charge–discharge rate: 15 mA g^{-1}. Cut–off voltage: 2.5–3.5 V. Cycle number: 1, 20, and 100.

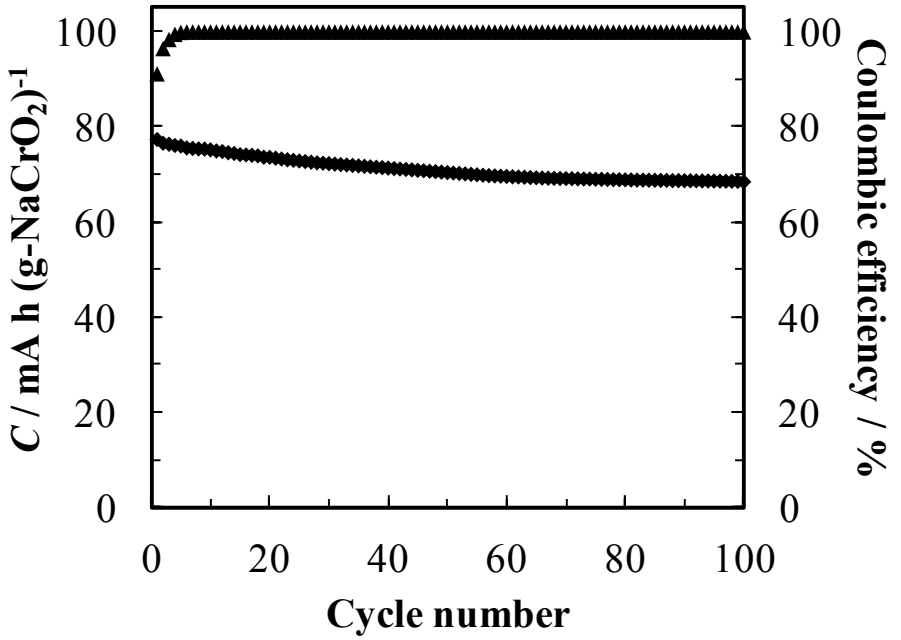

Fig. 3–9 Discharge capacity and coulombic efficiency for a Na/Na[FSA]–K[FSA]/$NaCrO_2$ cell at 353 K. Charge–discharge rate: 15 mA g^{-1}. Cut–off voltage: 2.5 and 3.5 V.

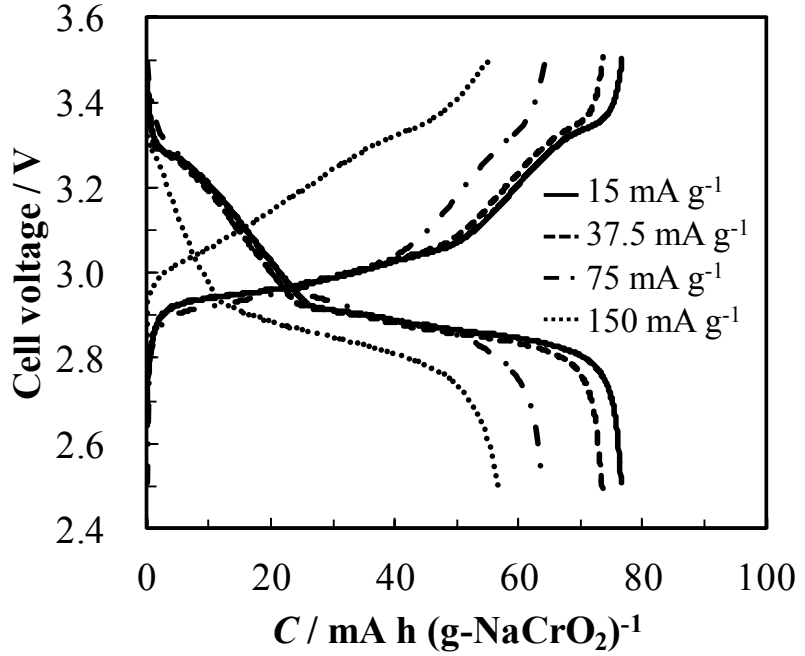

Fig. 3–10 Charge–discharge curves for a Na/Na[FSA]–K[FSA]/$NaCrO_2$ cell at 353 K. Charge–discharge rate: 150, 75, 37.5, 15 mA g^{-1}. Cut–off voltage: 2.5 and 3.5 V.

Chapter 4

$NaCrO_2$ positive electrode in Na[FSA]–[C_3C_1pyrr][FSA] ionic liquid

4.1 Introduction

A $NaCrO_2$ positive electrode was successfully operated in Na[TFSA]–Cs[TFSA] ionic liquid at 423 K, and showed a discharge capacity of 83.0 mAh $(g–NaCrO_2)^{-1}$ at 10 mA g^{-1} [1]. A Na/Na[FSA]–K[FSA]/$NaCrO_2$ cell exhibited a discharge capacity of 77.3 mAh $(g–NaCrO_2)^{-1}$ at 15 mA g^{-1}, at 353 K (See Chapter 3). However, these ionic liquids have rather high melting points (390 K for Na[TFSA]–Cs[TFSA] and 330 K for Na[FSA]–K[FSA]), which limits the operation temperature of the battery. Thus, in order to increase the operation temperature range, new ionic liquids with lower melting points are expected to be developed.

Consequently, the author focused on ionic liquid mixtures of Na[FSA] and [C_3C_1pyrr][FSA] (C_3C_1pyrr = *N*–methyl–*N*–propylpyrrolidinium). It has been reported that [C_3C_1pyrr][FSA] has a low melting point (264 K), high conductivity (6.4 mS cm^{-1} at 298 K), high thermal stability (up to 398 K), and a wide electrochemical window (ca. 5.3 V at 298 K) [2]. Several research groups have also reported that [C_3C_1pyrr][FSA] [3] and [C_4C_1pyrr][FSA] [4] ionic liquids exhibit good properties as the electrolytes for lithium secondary batteries. Therefore, the Na[FSA]–[C_3C_1pyrr][FSA] ionic liquid is expected to

have favorable properties as an electrolyte for sodium secondary battery operating over a wide temperature range.

In this Chapter, the viscosity, ionic conductivity, and electrochemical window of the Na[FSA]–[C_3C_1pyrr][FSA] ionic liquids that have several Na concentrations were measured at 258–368 K. A Na/Na[FSA]–[C_3C_1pyrr][FSA]/$NaCrO_2$ cell was constructed, and its charge–discharge properties were investigated in operation temperature range of 253–363 K in order to optimize the Na concentration in Na[FSA]–[C_3C_1pyrr][FSA] ionic liquid for better charge–discharge properties. $NaCrO_2$ was selected as an active material for the positive electrode because of its good performance at both room temperature [5] and intermediate temperatures (See Chapter 3). It has been also reported that $NaCrO_2$ is a fundamentally safe positive electrode material for sodium ion batteries with liquid electrolytes [6].

4.2 Experimental

Na[FSA]–[C_3C_1pyrr][FSA] ionic liquids were prepared as described in Chapter 2 in molar ratios of 0–60 mol% Na[FSA]. The viscosities of the Na[FSA]–[C_3C_1pyrr][FSA] ionic liquids were measured by a viscometer (Brookfield Engineering Laboratories, DV–II+ PRO). Their conductivities were measured by electrochemical impedance spectroscopy using a calibrated cell with two platinum plate electrodes and a potentiostat/galvanostat/frequency response analyzer (Ivium Technologies, IviumStat). The cell constant was determined using

standard KCl aqueous solution.

Electrochemical measurements were performed with a three–electrode system constructed in a Pyrex® beaker cell. The electrochemical window of the Na[FSA]–[C_3C_1pyrr][FSA] ionic liquid was measured by cyclic voltammetry. Sodium plate was used as the counter and reference electrodes. A nickel plate and a glassy carbon rod (3 mm in diameter) were used as the working electrodes to investigate the negative and positive potential limits of the Na[FSA]–[C_3C_1pyrr][FSA] ionic liquid, respectively. The scan rate for the cyclic voltammetry experiments was 10 mV s^{-1}.

Charge–discharge properties of the Na/Na[FSA]–[C_3C_1pyrr][FSA]/$NaCrO_2$ cell were measured by a two–electrode cell as described in Chapter 2. Charge–discharge tests were conducted at constant current rates of 20–2000 mA g^{-1} in the voltage range of 2.5–3.5 V at 253–363 K.

4.3 Results and discussion

Viscosities of the Na[FSA]–[C_3C_1pyrr][FSA] ionic liquids with 0–60 mol% Na[FSA] at different temperatures are shown in Fig. 4–1 (a). The viscosity increases with increase in the Na ion concentration. Similar phenomenon has also been observed for the Na[FSA]–[C_2C_1im][FSA] (C_2C_1im: 1–ethyl–3–methylimidazolium) [7], Na[TFSA]–[C_2C_1im][TFSA] [8], and Na[TFSA]–[C_4C_1pyrr][TFSA] (C_4C_1pyrr: *N*–butyl–*N*–methylpyrrolidinium) [9] ionic

liquid systems. The increase in viscosity is probably attributed to the strong interaction between Na^+ cation and FSA^- anion, forming ion pairs/clusters [8, 10]. Nevertheless, the viscosity of the Na[FSA]–[C_3C_1pyrr][FSA] ionic liquid decreases as the temperature rises. In the case of 40 mol% Na[FSA], the viscosity significantly decreases from 1180 mPa s at 278 K to 30.4 mPa s at 353 K.

Fig. 4–1 (b) shows the dependence of ionic conductivity on the Na[FSA] concentration at different temperatures. As expected from the results of viscosity, the ionic conductivity decreases when the Na ion concentration increases. However, the ionic conductivity can be largely improved by the elevation of temperature. For instance, the ionic conductivity of an IL containing 40 mol% Na[FSA] is as low as 0.04 mS cm^{-1} at 258 K. It increases, however, to 13 mS cm^{-1} at 368 K. For an IL containing 20 mol% Na[FSA], which corresponds to approximately 1 mol dm^{-3} Na[FSA], the ionic conductivity is 3.6 mS cm^{-1} at 298 K. This value is slightly lower than that of conventional $NaClO_4$/PC electrolyte at 1 mol dm^{-3} at 298 K (5–6 mS cm^{-1}) [11]. However, the conductivity of 20 mol% Na[FSA] system can be elevated to as high as 21 mS cm^{-1} at 368 K, at which the conventional organic electrolytes cannot be used.

A cyclic voltammogram of a nickel electrode in the Na[FSA]–[C_3C_1pyrr][FSA] ionic liquid with a molar ratio of 20 mol% Na[FSA] at 353 K is shown in Fig. 4–2. A pair of cathodic and anodic currents is observed at 0 V vs. Na/Na^+, which corresponds to the

deposition and dissolution of sodium metal. Fig. 4–3 shows a cyclic voltammogram of the glassy carbon rod electrode in the Na[FSA]–[C_3C_1pyrr][FSA] ionic liquid at 353 K. It can be seen that anodic current increases rapidly from 5.2 V vs. Na/Na^+. The anodic current is believed to correspond to the irreversible oxidation of FSA anions. From the results in Figs. 4–2 and 4–3, the electrochemical window of the Na[FSA]–[C_3C_1pyrr][FSA] ionic liquid with a molar ratio of 20 mol% Na[FSA] is determined to be 5.2 V at 353 K. The wide electrochemical window indicates that the Na[FSA]–[C_3C_1pyrr][FSA] ionic liquid is highly desirable as an electrolyte for sodium secondary batteries.

Aluminum was used as a current collector for the positive electrode in this study. The stability of the aluminum plate electrode was investigated before the charge–discharge tests. Since the highest charging voltage is 3.5 V for the $NaCrO_2$ positive electrode (See chapter 3), the stability test for the aluminum plate electrode was conducted at 3.8 V vs. Na/Na^+ in the Na[FSA]–[C_3C_1pyrr][FSA] ionic liquid at 353 K. Fig. 4–4 shows the current at an aluminum plate electrode in the Na[FSA]–[C_3C_1pyrr][FSA] ionic liquid at 353 K during potentiostatic electrolysis at 3.8 V vs. Na/Na^+. The current is negligibly small, below 0.6 μA cm^{-2}, implying that the aluminum plate electrode is electrochemically stable at potential of 3.8 V vs. Na/Na^+. Similar electrochemical stability of aluminum is explained by the formation of a passivation film on the aluminum surface. The passivation film is probably formed by the reaction between Al^{3+} and FSA^- (See Chapter 3).

Fig. 4–5 (a) shows the discharge curves at current rates of 50–2000 mA (g–$NaCrO_2$)$^{-1}$ for a Na/Na[FSA]–[C_3C_1pyrr][FSA]/$NaCrO_2$ cell with 40 mol% Na[FSA] at 363 K. Here, the current rate for charge and discharge processes is the same. When the theoretical capacity of $NaCrO_2$ is defined as 125 mAh (g–$NaCrO_2$)$^{-1}$ ($0.5 \leqq x \leqq 1$ in Na_xCrO_2), 50 and 2000 mA (g–$NaCrO_2$)$^{-1}$ correspond to 0.4C and 16C in the C–rate, respectively. The discharge capacities and coulombic efficiency for different current rates are shown in Fig. 4–5 (b). The shape of the charge–discharge curves at 50 mA (g–$NaCrO_2$)$^{-1}$ is the same for those reported previously [12, 13]. The composition–driven structural changes observed during the charge or desodiation process occur in the following sequence: rhombohedral O3, monoclinic O'3, and monoclinic P'3 structures [12, 13]. The discharge capacity decreases gradually with increase in the charge–discharge rate. At 500 mA (g–$NaCrO_2$)$^{-1}$, the discharge capacity is 96 mAh (g–$NaCrO_2$)$^{-1}$ and about 90% of the capacity at 50 mA (g–$NaCrO_2$)$^{-1}$ is maintained. The discharge capacity decreases to 76 mAh (g–$NaCrO_2$)$^{-1}$ at a high rate of 2000 mA (g–$NaCrO_2$)$^{-1}$, but it still corresponds to about 71% of the capacity at 50 mA (g–$NaCrO_2$)$^{-1}$. For all charge–discharge rates, except for the initial cycle, the coulombic efficiencies are higher than 99.5%. The cell also shows good cycle performance at each rate. These results demonstrate that the cell with 40 mol% Na[FSA] exhibits good rate capability and cycleability at 363 K.

It is expected that the cells would show different rate capabilities when the Na ion

concentration in the ionic liquids is varied. Fig. 4–6 compares the rate capabilities of Na/Na[FSA]–[C_3C_1pyrr][FSA]/$NaCrO_2$ cells with 20, 30, 40, 50, and 60 mol% Na[FSA] at 363 K. At charge–discharge rates lower than 500 mA $(g–NaCrO_2)^{-1}$, the effect of Na ion concentration on the discharge capacity is very small. On the contrary, the Na ion concentration considerably affects the discharge capacity at charge–discharge rates higher than 500 mA $(g–NaCrO_2)^{-1}$. At the highest charge–discharge rate of 2000 mA $(g–NaCrO_2)^{-1}$, the discharge capacity increases with an increase in the Na ion concentration from 20 to 40 mol% Na[FSA]. When the Na ion concentration reaches 40 mol% Na[FSA], the cell shows the highest discharge capacity of 76 mAh $(g–NaCrO_2)^{-1}$. Then, the discharge capacity decreases with an increase in the Na ion concentration. This is because higher Na ion concentration leads to increased Na ion conductivity, but excess Na ion concentration also increases the viscosity of the ionic liquid, resulting in the decrease of Na ion conductivity. Thus, it is concluded that 40 mol% Na[FSA] is the optimum concentration for Na/Na[FSA]–[C_3C_1pyrr][FSA]/$NaCrO_2$ cell, which shows the best rate capability at 363 K.

To investigate the effect of operation temperature on the charge–discharge performance, Na/Na[FSA]–[C_3C_1pyrr][FSA]/$NaCrO_2$ cells with different Na ion concentrations (10, 15, 20, 25, and 30 mol% Na[FSA]) were tested from 363 K down to 253 K. As a typical result, Fig. 4–7 (a) shows the charge–discharge curves of a cell with 25 mol% Na[FSA] at 253–363 K at current rate of 20 mA $(g–NaCrO_2)^{-1}$. The discrepancy of the plateau

potentials between the charge and discharge curves is increased when the operation temperature is lowered. As a natural consequence, the discharge capacity is reduced when the temperature is decreased. It should be noted, however, that both the discrepancy of the plateau potentials and the decrease in capacity are scarcely observed at 298 K.

Fig. 4–7 (b) shows the discharge capacities and coulombic efficiency of the cell with 25 mol% Na[FSA] at 253–363 K at a current rate of 20 mA $(g–NaCrO_2)^{-1}$. At 363 K, the discharge capacity is 123 mAh $(g–NaCrO_2)^{-1}$, which is very close to the theoretical capacity of 125 mAh $(g–NaCrO_2)^{-1}$. When the temperature is lowered from 363 K to 298 K, the discharge capacity decreases slightly to 117 mAh $(g–NaCrO_2)^{-1}$. For comparison, it was reported that a capacity of 104 mAh $(g–NaCrO_2)^{-1}$ was obtained at 298 K at a current rate of 5.0 mA $(g–NaCrO_2)^{-1}$, where 1 M $NaClO_4$/PC was used as an electrolyte [12]. Compared with the conventional organic electrolytes, the present ionic liquid electrolyte shows larger discharge capacity at 298–363 K, and is promising for the applications to EVs and HEVs. When the temperature becomes lower than 298 K, the discharge capacity further decreases. Nevertheless, a capacity of 106 mAh $(g–NaCrO_2)^{-1}$, corresponding to about 86% of the initial discharge capacity at 363 K, is still maintained at 273 K. At lower temperatures, 263 and 253 K, the cell delivers average discharge capacities of approximately 85 and 25 mAh $(g–NaCrO_2)^{-1}$, respectively. The lower capacity at low temperatures is attributed to the high internal resistance of cell, which arises from reduced ionic conductivity of electrolyte,

lowered diffusivity of sodium ion in solid Na_xCrO_2, and increased charge–transfer resistance at electrode/electrolyte interfaces [14]. It should be noted, however, that the discharge capacity is almost fully recovered to the initial value when the temperature is raised to 363 K again. The coulombic efficiency is close to 100% except for the initial cycle at each temperature and for all cycles at 253 K. As a result, the Na/Na[FSA]–$[C_3C_1pyrr][FSA]/NaCrO_2$ cell can be operable in a wide temperature range of 263–363 K. At a very low temperature, 253 K, the cell can discharge with a small capacity, which means that it is possible to start heating the battery by itself.

The Na/Na[FSA]–$[C_3C_1pyrr][FSA]/NaCrO_2$ cells with different Na ion concentrations show similar charge–discharge behaviors at low discharge rates of 20–50 mA $(g–NaCrO_2)^{-1}$ at 298–363 K. At lower temperatures of 253–273 K, however, the discharge capacities are different for cells with different Na ion concentrations. Fig. 4–8 is the comparison of discharge capacities of the cells with 10, 15, 20, 25, and 30 mol% Na[FSA] at 253–363 K. As previously mentioned, the discharge capacities at 298–363 K are almost unaffected by the Na ion concentration. At temperatures below 273 K, the discharge capacity increases gradually with an increase in the Na ion concentration. At temperatures of 253, 263, and 273 K, the cell exhibits the highest discharge capacities at 25 mol% Na[FSA]. At 30 mol% Na[FSA], the discharge capacity decreases again, which is attributed to the opposing effect on ionic conduction caused by the increase of viscosity of the electrolyte. It is

concluded that the cell with 25 mol% Na[FSA] exhibits the best electrochemical performance below room temperature.

4.4 Conclusions

The author has investigated the use of Na[FSA]–[C_3C_1pyrr][FSA] ionic liquids as electrolytes for sodium secondary batteries operating over a wide temperature range of 253–363 K. This ionic liquid exhibits a wide electrochemical window of 5.2 V at 353 K. The viscosity increases and the ionic conductivity decreases when the Na ion concentration in IL increases. By the elevation of temperature, however, ionic conductivities much higher than that of conventional organic electrolyte at room temperature can be achieved. Na ion concentration in the ionic liquids strongly affects the rate capability of a Na/Na[FSA]–[C_3C_1pyrr][FSA]/$NaCrO_2$ cell. The best rate capability at 363 K is obtained at 40 mol% Na[FSA]. The operation temperature also significantly influences the charge–discharge performance, especially at low temperatures, and the discharge capacity decreases gradually with decrease in the operation temperature. At operation temperatures below 273 K, 25 mol% Na[FSA] is found to be the optimum Na ion concentration. It is concluded that there exist different optimum ranges of Na ion concentration depending on the operation temperatures.

References

[1] T. Nohira, T. Ishibashi, R. Hagiwara, J. Power Sources 205 (2012) 506–509.

[2] Q. Zhou, W.A. Henderson, G.B. Appetecchi, M. Montanino, S. Passerini, J. Phys. Chem. B 112 (2008) 13577–13580.

[3] M. Ishikawa, T. Sugimoto, M. Kikuta, E. Ishiko, M. Kono, J. Power Sources 162 (2006) 658–662.

[4] E. Paillard, Q. Zhou, W.A. Henderson, G.B. Appetecchi, M. Montanino, S. Passerini, J. Electrochem. Soc. 156 (2009) A891–A895.

[5] S. Komaba, C. Takei, T. Nakayama, A. Ogata, N. Yabuuchi, Electrochem. Commun. 12 (2010) 355–358.

[6] X. Xia, J.R. Dahn, Electrochem. Solid–State Lett. 15 (2012) A1–A4.

[7] K. Matsumoto, T. Hosokawa, T. Nohira, R. Hagiwara, A. Fukunaga, K. Numata, E. Itani, S. Sakai, K. Nitta, S. Inazawa, J. Power Sources 265 (2014) 36–39.

[8] D. Monti, E. Jonsson, M.R. Palacin, P. Johansson, J. Power Sources 245 (2014) 630–636.

[9] S.A.M. Noor, P.C. Howlett, D.R. MacFarlane, M. Forsyth, Electrochim. Acta 114 (2013) 766–771.

[10] A. Andriola, K. Singh, J. lewis, L. Yu, J. Phys. Chem. B 114 (2010) 11709–11714.

[11] K. Kuratani, N. Uemura, H. Senoh, H.T. Takeshita, T. Kiyobayashi, J. Power Sources 223 (2013) 175–182.

[12] S. Komaba, T. Nakayama, A. Ogata, T. Shimizu, C. Takei, S. Takada, A. Hokura, I. Nakai, ECS Trans. 16 (2009) 43–55.

[13] C.Y. Chen, K. Matsumoto, T. Nohira, R. Hagiwara, A. Fukunaga, S. Sakai, K. Nitta, S. Inazawa, J. Power Sources 237 (2013) 52–57.

[14] S.S. Zhang, K. Xu, T.R. Jow, J. Power Sources 115 (2003) 137–140.

Figures

(a)

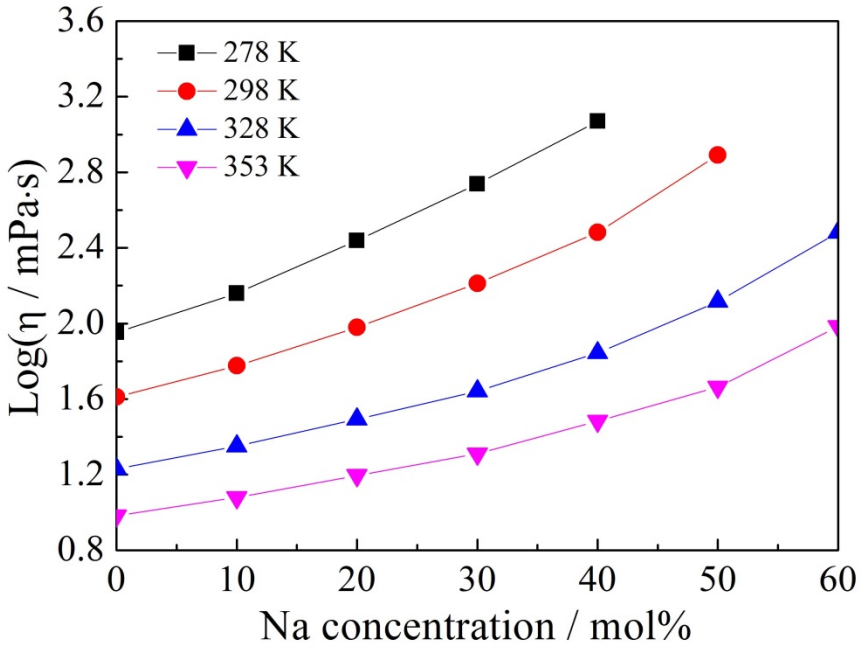

(b)

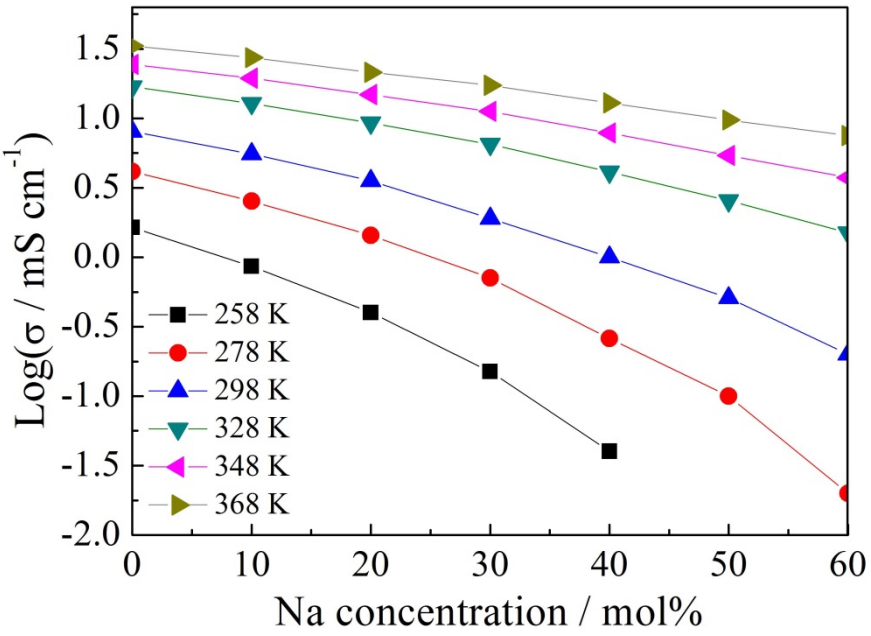

Fig. 4–1 Dependences of (a) viscosity and (b) ionic conductivity on the Na[FSA] concentration of Na[FSA]–[C_3C_1pyrr][FSA] ionic liquid at different temperatures.

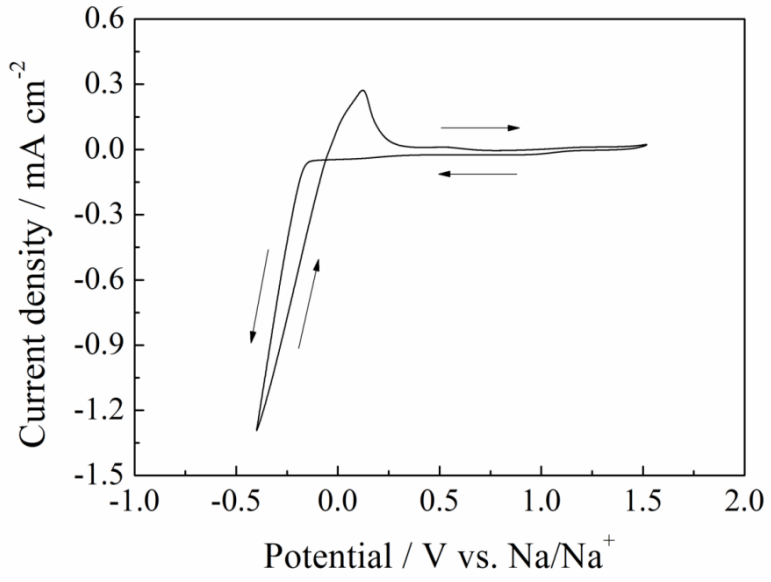

Fig. 4–2 Cyclic voltammogram of a Ni plate electrode in Na[FSA]–[C_3C_1pyrr][FSA] ionic liquid with 20 mol% Na[FSA] at 353 K.

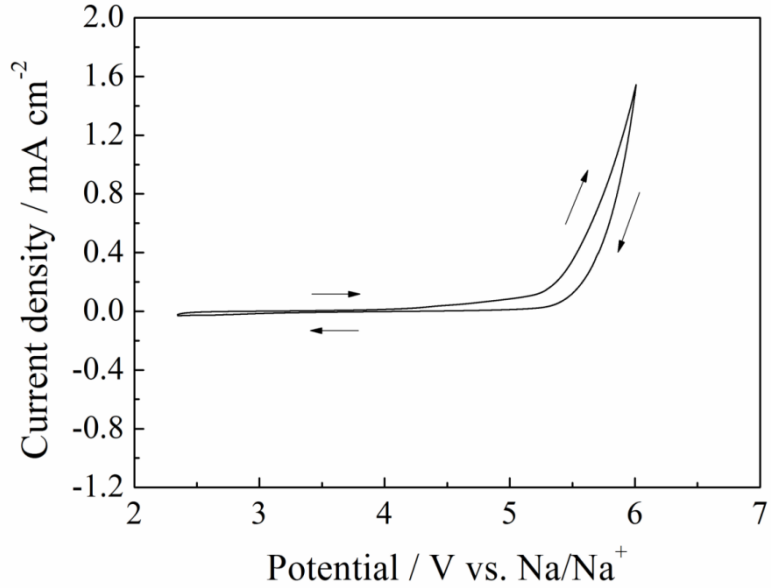

Fig. 4–3 Cyclic voltammogram of a glassy carbon rod electrode in Na[FSA]–[C_3C_1pyrr][FSA] ionic liquid with 20 mol% Na[FSA] at 353 K.

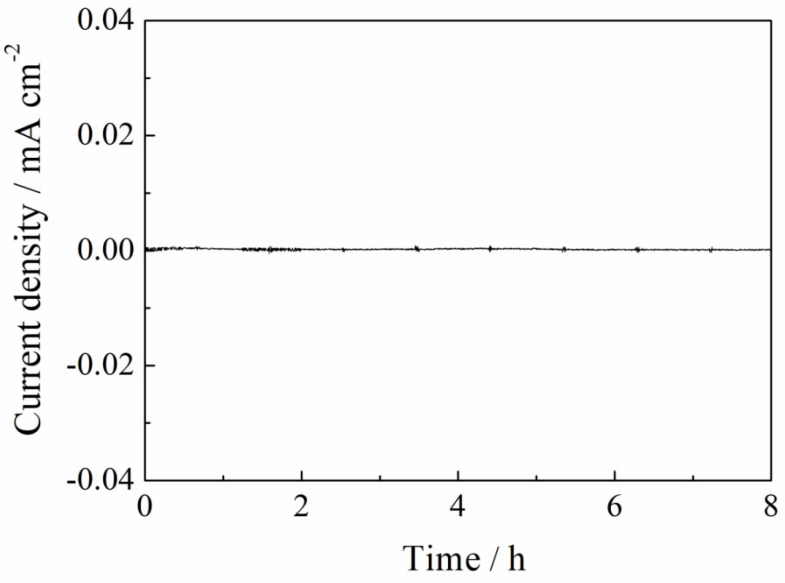

Fig. 4–4 Chronoamperogram of an Al plate electrode in Na[FSA]–[C_3C_1pyrr][FSA] ionic liquid with 20 mol% Na[FSA] at 353 K. Potential: 3.8 V vs. Na/Na^+.

(a)

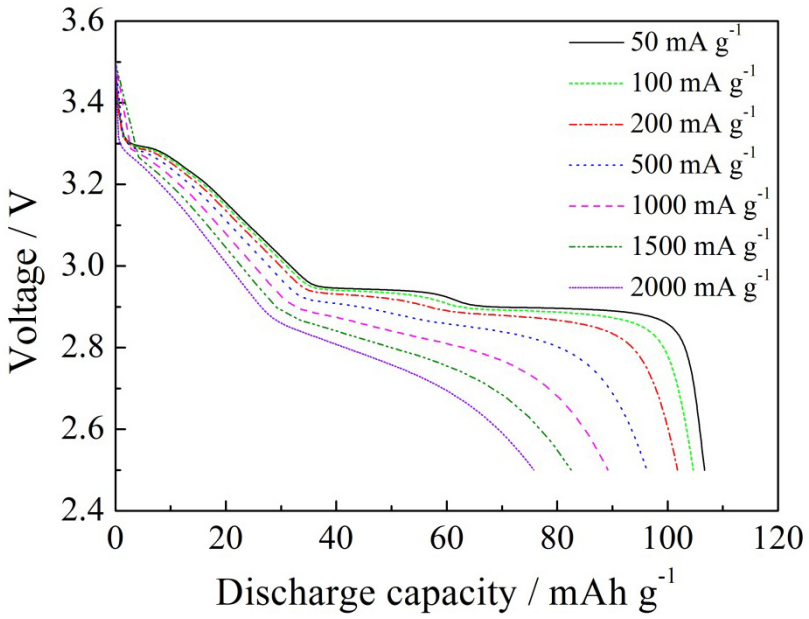

(b)

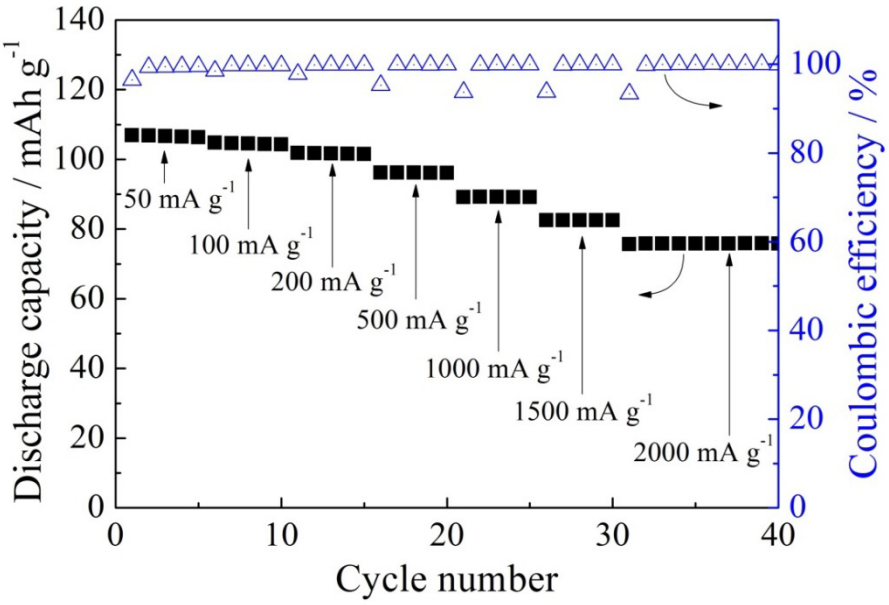

Fig. 4–5 Rate capability of a Na/Na[FSA]–[C_3C_1pyrr][FSA]/$NaCrO_2$ cell with 40 mol% Na[FSA] at 363 K: (a) discharge curves and (b) discharge capacities and coulombic efficiency. Charge–discharge rates: 50–2000 mA g^{-1}. Cut–off voltages: 2.5 V and 3.5 V.

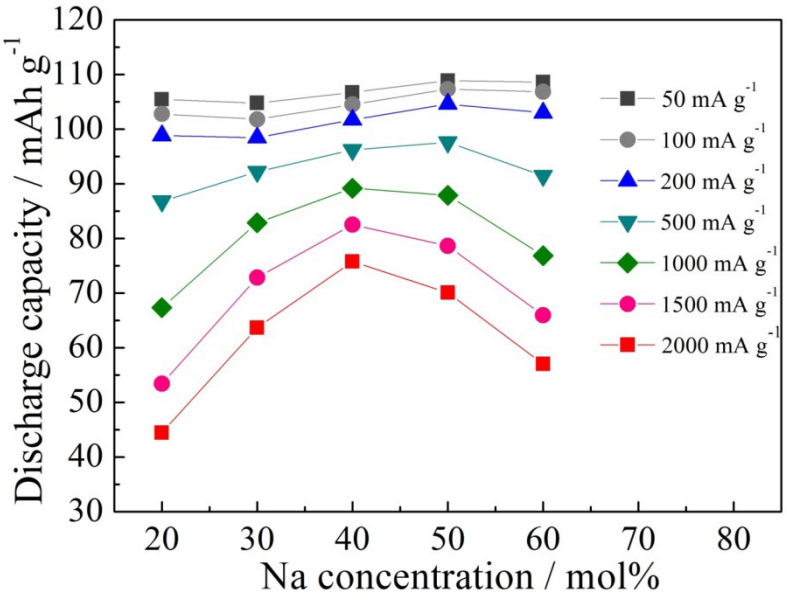

Fig. 4–6 Comparison of rate capability for Na/Na[FSA]–[C_3C_1pyrr][FSA]/$NaCrO_2$ cells with 20–60 mol% Na[FSA] at 363 K. Charge–discharge rates: 50–2000 mA g^{-1}. Cut–off voltages: 2.5 V and 3.5 V.

(a)

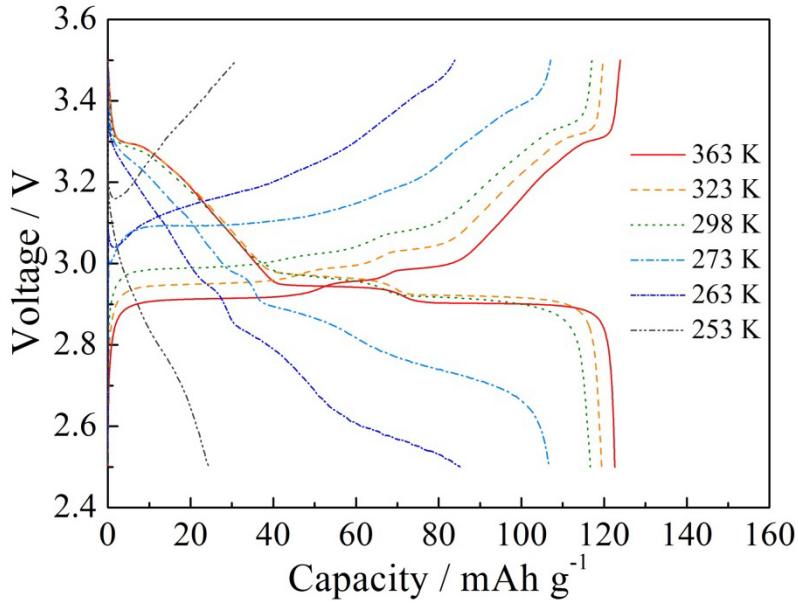

(b)

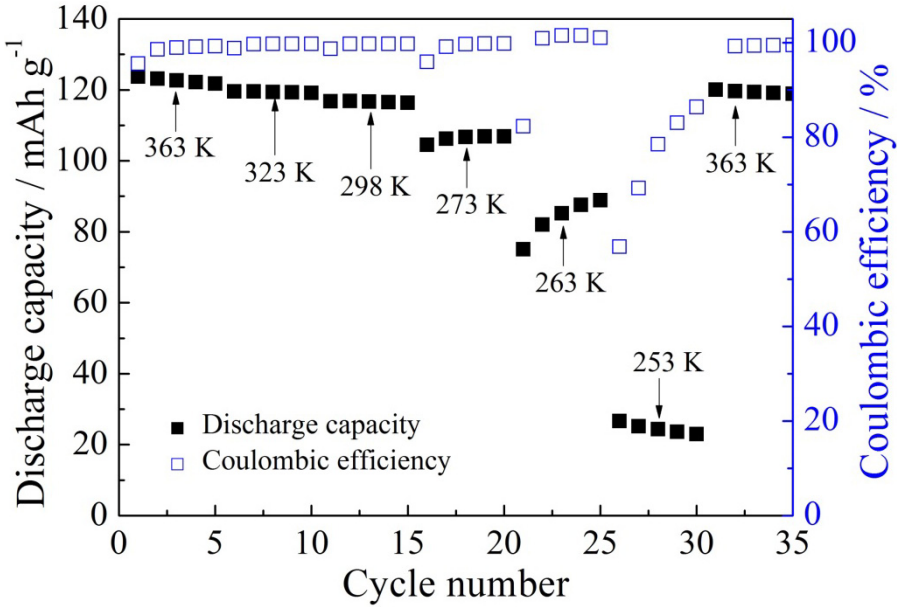

Fig. 4–7 Charge and discharge performance of a Na/Na[FSA]–[C_3C_1pyrr][FSA]/$NaCrO_2$ cell with 25 mol% Na[FSA] at 253–363 K: (a) charge–discharge curves and (b) discharge capacities and coulombic efficiency. Charge–discharge rate: 20 mA g^{-1}. Cut–off voltages: 2.5 V and 3.5 V.

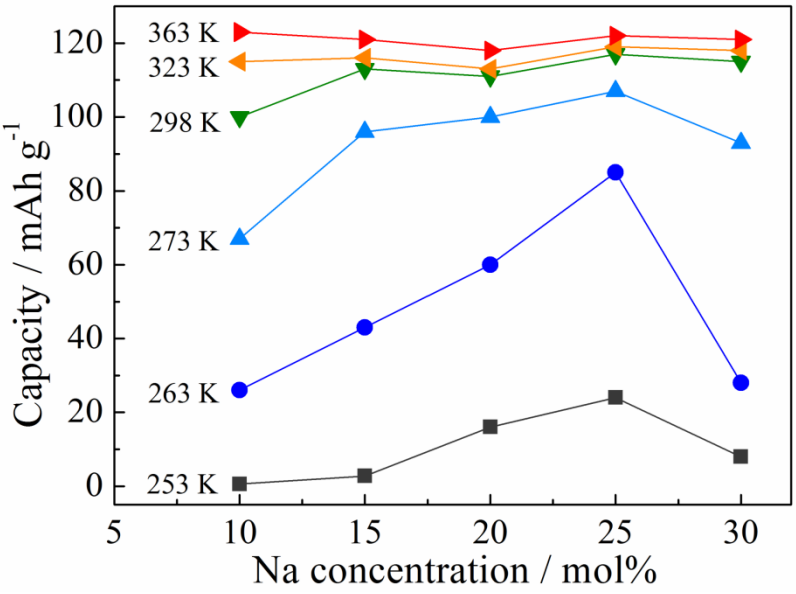

Fig. 4–8 Comparison of discharge capacities for Na/Na[FSA]–[C_3C_1pyrr][FSA]/$NaCrO_2$ cells with 10–30 mol% Na[FSA] at 253–363 K. Charge–discharge rate: 20 mA g^{-1}. Cut–off voltages: 2.5 V and 3.5 V.

Chapter 5

Hard carbon in Na[FSA]–[C_3C_1pyrr][FSA] ionic liquid

5.1 Introduction

Concerning the studies on negative electrodes of sodium secondary batteries in organic electrolytes, Komaba et al. [1] and Ponrouch et al. [2] have reported that hard carbon (HC) shows a stable charge–discharge behavior with 250–300 mAh $(g–HC)^{-1}$ at 298 K. However, HC shows poor rate capability at room temperature; the capacity at a discharge rate of 2C shows only 40% of the capacity at rate of C/10 [2]. Because high rate capability is one of the more important properties for the practical use of HC (e.g. batteries for EVs), the improvement of rate capability is necessary for the Na/HC system.

It is reasonably expected that rate capability is largely improved by the elevation of operation temperature. Hagiwara et al. have already reported an excellent rate capability of 2000 mA $(g–NaCrO_2)^{-1}$ (approximately 18C) for the $NaCrO_2$ positive electrode in a Na[FSA]–K[FSA] ionic liquid at 353 K [3]. Thus, the author first tried to apply the HC negative electrode to Na[FSA]–K[FSA] ionic liquid at 363 K. As described in Section 5.3, however, a Na/Na[FSA]–K[FSA]/HC cell showed a small discharge capacity and poor cycleability. Because the presence of K^+ ions was presumed to be the cause of the poor properties obtained, the author selected Na[FSA]–[C_3C_1pyrr][FSA] (C_3C_1pyr: *N*–methyl–*N*–

propylpyrrolidinium, Fig. 1–5) as a second ionic liquid for investigation. In Chapter 4, fundamental properties such as ionic conductivity and viscosity were measured for this ionic liquid; a Na/Na[FSA]–[C_3C_1pyrr][FSA] /$NaCrO_2$ cell was successfully operated at 253–363 K. In this Chapter, the author report the charge–discharge behavior of Na/Na[FSA]–[C_3C_1pyrr][FSA] (10 mol% Na[FSA])/HC cells at 363 K. To study the influence of the K^+ ion, the behavior of the HC negative electrode was also investigated by using different compositions of ionic liquids (Na[FSA]:K[FSA]:[C_3C_1pyrrr][FSA] = 8:2:90, 5:5:90, 0:10:90 mol%). Finally, to demonstrate high rate capability at 363 K, the Na/Na[FSA]–[C_3C_1pyrr][FSA]/HC cell was tested in the range 25–1000 mA $(g\text{–}HC)^{-1}$.

5.2 Experimental

Na[FSA], K[FSA] (Mitsubishi Materials Electronic Chemicals Co., Ltd., Japan, >99.0%) and [C_3C_1pyrr][FSA] (Kanto Chemical Co., Inc. Japan, >99.0%) were dried and mixed as described in Chapter 2. The eutectic Na[FSA]–K[FSA] ionic liquid (Na[FSA]:K[FSA] = 56:44 mol%), Na[FSA]–[C_3C_1pyrr][FSA] ionic liquid (Na[FSA]:[C_3C_1pyrr][FSA] = 10:90 mol%), and Na[FSA]–K[FSA]–[C_3C_1pyrr][FSA] ionic liquids (Na[FSA]:K[FSA]:[C_3C_1pyrr][FSA] = 8:2:90, 5:5:90 and 0:10:90 mol%) were prepared.

HC electrode was fabricated as described in Chapter 2. Loading density of HC was

4.7 (mg–HC) cm^{-2}. Thickness of the obtained HC electrode was ca. 50 μm.

Charge–discharge properties of the Na/HC cell were measured with a 2032 type two–electrode cell as described in Chapter 2. The HC electrode was used as a positive (working) electrode. Sodium foil (Aldrich, >99.9%) was used for the negative (reference and counter) electrode. A microporous membrane (NPS050, Nippon Sheet Glass Co., Ltd., thickness of 50 μm) was used as a separator. Charge–discharge tests were conducted at a constant charge current rate of 25 mA $(g–HC)^{-1}$ and discharge current rates of 25–1000 mA $(g–HC)^{-1}$ in the voltage region 0.005–1.200 V. Temperature of the cell was maintained at 363 K.

5.3 Results and discussion

Fig. 5–1 indicates the charge–discharge curves of first, second, and third cycles for a Na/Na[FSA]–KFSA/HC cell at 363 K. Unfortunately, the cell showed poor charge–discharge properties; the capacity at first charge was 147 mAh $(g–HC)^{-1}$, which is much smaller than the reported value of 250 mAh $(g–HC)^{-1}$ for $NaClO_4$/PC at 298 K [1]. An even smaller capacity of 72 mAh $(g–HC)^{-1}$ was observed for the first discharge. For the second cycle, charge and discharge capacities were largely decreased, displaying the values of 31 and 26 mAh $(g–HC)^{-1}$, respectively. Since, Na^+ ions are known to be inserted/extracted into/from HC electrode, this result suggested that the HC electrode irreversibly reacted with the Na[FSA]–K[FSA] electrolyte, likely with K^+ ions. It was expected that an ionic liquid containing no potassium salt would give a reversible charge/discharge behavior.

Thus, a Na[FSA]–[C_3C_1pyrr][FSA] (10 mol% Na[FSA]) ionic liquid was used at the same temperature of 363 K. Fig. 5–2 shows the charge–discharge curves of a Na/Na[FSA]–[C_3C_1pyrr][FSA]/HC cell at the first (solid curve), 10th (dashed curve), and 40th cycle (dashed–dotted curve), respectively. At the first cycle, charge capacity was 343 mAh (g–HC)$^{-1}$, and discharge capacity was 264 mAh (g–HC)$^{-1}$. Fig. 5–3 shows the cycle properties of a Na/Na[FSA]–[C_3C_1pyrr][FSA]/HC cell. Although coulombic efficiency was 76.9% for the first cycle, it was drastically improved to 99% for the second cycle. The coulombic efficiency continuously improved as the charge–discharge cycle progressed, reaching 99.9% at the 37th cycle. The discharge capacity at the 50th cycle was 252 mAh (g–HC)$^{-1}$ corresponding to 95.5% of the first discharge capacity. These results confirm that Na^+ ions can be practically inserted/extracted into/from the HC electrode reversibly in the Na[FSA]–[C_3C_1pyrr][FSA] ionic liquid. It should be noted that only EC/DEC, PC, or EC/PC (EC: ethylene carbonate, DEC: diethyl carbonate, PC: propylene carbonate) systems have been previously reported to give a reversible charge–discharge behavior for HC [1, 2]. Irreversible capacity for the initial few cycles (in total, 80 mAh (g–HC)$^{-1}$) appears to be the cause of the formation of a solid electrolyte interphase (SEI), which was probably formed by decomposition of [C_3C_1pyrr][FSA] and/or Na[FSA] on the HC electrode surface. It is presumed that the SEI formation mainly occurs at a long sloping region at 1.3–0.2 V in the first charge curve in Fig. 5–2.

To investigate the influence of K^+ ions on Na^+ insertion, charge–discharge curves of the HC electrode were measured in ionic liquids with different compositions (Na[FSA]:K[FSA]:[C_3C_1pyrr][FSA] = 10:0:90, 8:2:90, 5:5:90, and 0:10:90 mol%) at 363 K. Fig. 5–4 shows the obtained curves at the first cycles. Here, the curves for 10:0:90 were observed to be similar to those shown in Fig. 5–2. The charge capacity decreased as the content of K^+ ion increased, i.e., 343, 285, 266, and 235 mAh $(g–HC)^{-1}$ for 10:0:90, 8:2:90, 5:5:90, and 0:10:90, respectively. More drastic differences were observed for the discharge capacities; the capacity decreased from 264 to 209, 173, and 87 mAh $(g–HC)^{-1}$. These results indicate that the insertion of K^+ ions into HC proceeds, and that once K^+ ions are inserted, they are more difficult to be extracted compared with Na^+ ions. The influence of K^+ ions was also clearly observed when the charge–discharge cycle was allowed to proceed. Fig. 5–5 shows the cycle dependence of discharge capacity for these cells. In contrast with the cell containing no K^+ ion, the increase in K^+ ions was found to exert a serious effect on the discharge capacity. It is obvious from these results that the existence of K^+ ions inhibits the reversible insertion/extraction of Na^+ ions into/from HC. One of the more conceivable explanations is as follows: when K^+ ions are inserted into HC, compounds with low crystallinity somehow structurally related to graphite intercalation compounds such as C_8K and $C_{12n}K$ ($n \geq 2$) [4, 5] from which K^+ ions can be reversibly extracted may form. However, the presence of K^+ ions may change the nature of SEI film so that the incorporation of K^+ ions

into the SEI film results in an increase of the electrical resistivity of film. The ratio of K^+ ion in the film increases due to the ion–exchange reaction as the charging and discharging cycle proceeds, resulting in a further increase of the resistivity and a decrease in the capacity.

Finally, the rate capability of the Na/Na[FSA]–[C_3C_1pyrr][FSA] (10 mol% Na[FSA])/HC cell was studied at 363 K. Fig. 5–6 shows discharge curves at currents of 25 (corresponding to ca. C/10), 50 (C/5), 125 (C/2), 250 (1C), 500 (2C), 750 (3C), and 1000 (4C) mA $(g–HC)^{-1}$. The rate dependence of the discharge capacity is described in Fig. 5–7. All charging was conducted at a constant current of 25 mA $(g–HC)^{-1}$. As can be seen from Fig. 5–6, the decrease in the discharge capacity was small even at high currents. At the discharge rate of 1000 mA $(g–HC)^{-1}$ (4C), a discharge capacity of 211 mAh $(g–HC)^{-1}$, which corresponds to 80% of the capacity at 25 mA $(g–HC)^{-1}$ (C/10), was maintained. Discharge curves at higher rates exhibited a characteristic behavior corresponding to an increase in IR drop (voltage drop that caused by the DC resistance of the cell). This indicates that extraction of Na^+ ions from the HC nanostructure is not the rate–determining process during the discharge. Concerning the rate capability of the HC electrode in $NaClO_4$/PC at room temperature (298 K) [2], it was reported that the discharge capacity decreased from >300 mAh $(g–HC)^{-1}$ at a rate of C/10 to 120 mAh $(g–HC)^{-1}$ at 2C. Thus, the HC electrode in Na[FSA]–[C_3C_1pyrr][FSA] electrolyte at 363 K has a remarkably high rate capability.

5.4 Conclusions

Charge–discharge properties of HC in a Na[FSA]–[C_3C_1pyrr][FSA] ionic liquid have been investigated. The cycle test of a Na/Na[FSA]–[C_3C_1pyrr][FSA]/HC cell at 363 K revealed that the HC electrode has a reversible capacity of ca. 250 mAh $(g–HC)^{-1}$ in the Na[FSA]–[C_3C_1pyrr][FSA] electrolyte, maintaining 95.5% of the first discharge capacity after 50 cycles with 99.9% coulombic efficiency. In contrast, a Na/HC cell with Na[FSA]–K[FSA] electrolyte showed poor reversibility. By using Na[FSA]–K[FSA]–[C_3C_1pyrr][FSA] systems with various Na^+/K^+ ratios, it was revealed that irreversible K^+ insertion inhibits the reversible Na^+ insertion into HC. Finally, it was demonstrated that a Na/Na[FSA]–[C_3C_1pyrr][FSA]/HC cell has an excellent rate capability. At a rate of 1000 mA $(g–HC)^{-1}$ (4C), a discharge capacity of 211 mAh $(g–HC)^{-1}$ was obtained, which corresponds to 80% of the capacity at 25 mA $(g–HC)^{-1}$ (C/10). Thus, it is concluded that this combination of HC electrode and Na[FSA]–[C_3C_1pyrr][FSA] ionic liquid can provide a safe and high–rate negative electrode for sodium–ion batteries.

References

[1] S. Komaba, W. Murata, T. Ishikawa, N. Yabuuchi, T. Ozeki, T. Nakayama, A. Ogata, K. Gotoh, K. Fujiwara, Adv. Funct. Mater. 21 (2011) 3859–3867.

[2] A. Ponrouch, A.R. Goñi, M.R. Palacín, Electrochem. Commun. 27 (2013) 85–88.

[3] C.Y. Chen, K. Matsumoto, T. Nohira, R. Hagiwara, A. Fukunaga, S. Sakai, K. Nitta, S. Inazawa, J. Power Sources 237 (2013) 52–57.

[4] J. Sangster, J. Phase Equilib. Diffus. 29 (2008) 73–83.

[5] P.L. Walker, P.A. Thrower, Chemistry and Physics of carbon. 12 (1977) 1–37.

Figures

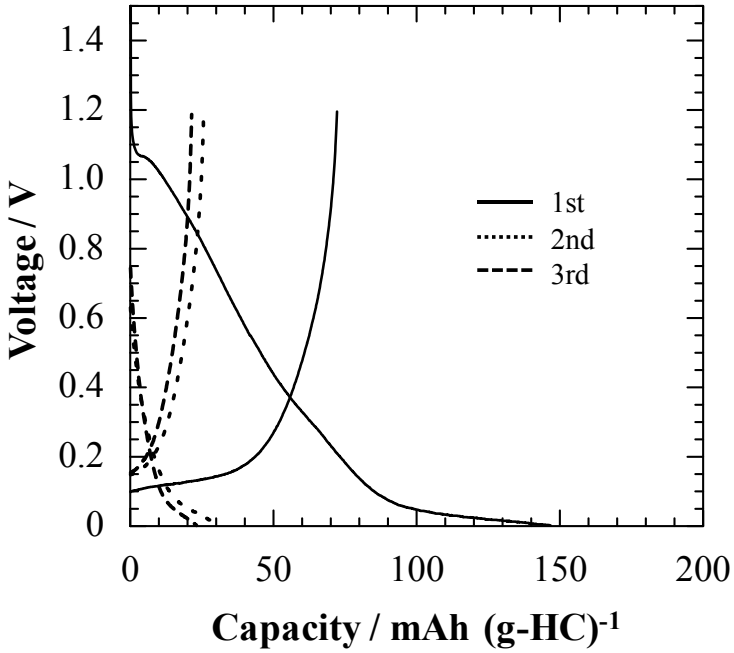

Fig. 5–1 Charge–discharge curves for a Na/Na[FSA]–K[FSA]/HC cell at 363 K. Charge–discharge rate: 50 mA $(g–HC)^{-1}$; cut–off voltages: 0.005 and 1.200 V; cycle number: 1st, 2nd, and 3rd.

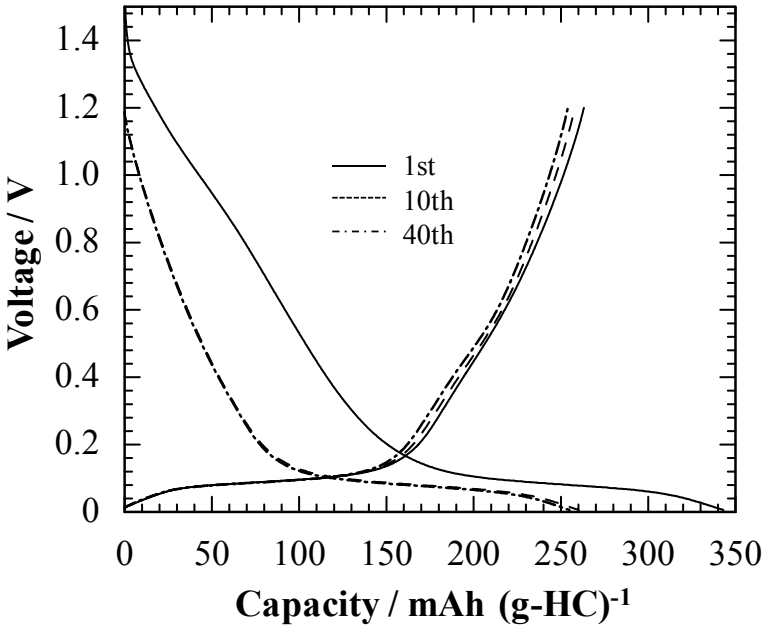

Fig. 5–2 Charge and discharge curves for a Na/Na[FSA]–[C_3C_1pyrr][FSA]/HC cell at 363 K. Charge–discharge rate: 50 mA $(g–HC)^{-1}$; cut–off voltages: 0.005 and 1.200 V; cycle number: 1st, 10th, and 40th.

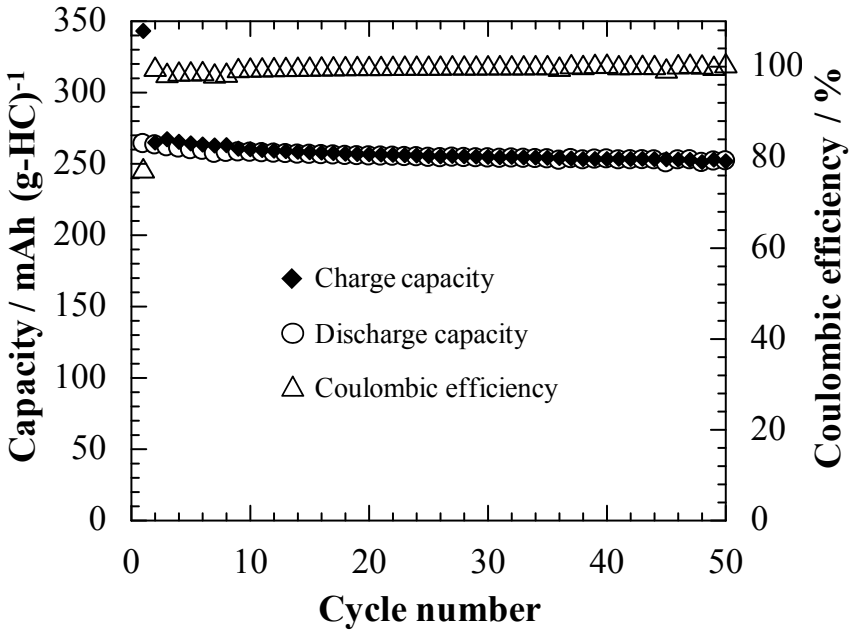

Fig. 5–3 Cycle dependence of charge capacity, discharge capacity, and coulombic efficiency for a Na/Na[FSA]–[C_3C_1pyrr][FSA]/HC cell at 363 K. Charge–discharge rate: 50 mA (g–HC)$^{-1}$; cut–off voltages: 0.005 and 1.200 V.

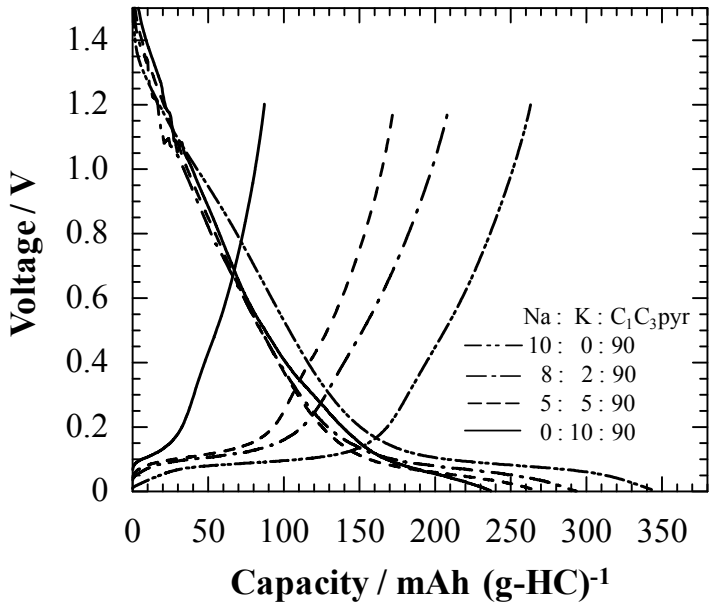

Fig. 5–4 Charge–discharge curves at the 1st cycle for Na/Na[FSA]–K[FSA]–[C_3C_1pyrr][FSA]/HC cells (Na[FSA]:K[FSA]:[C_3C_1pyrr][FSA] = 10:0:90, 8:2:90, 5:5:90 and 0:10:90 mol%). Charge–discharge rate: 50 mA (g–HC)$^{-1}$; operating temperature: 363 K; cut–off voltages: 0.005 and 1.200 V.

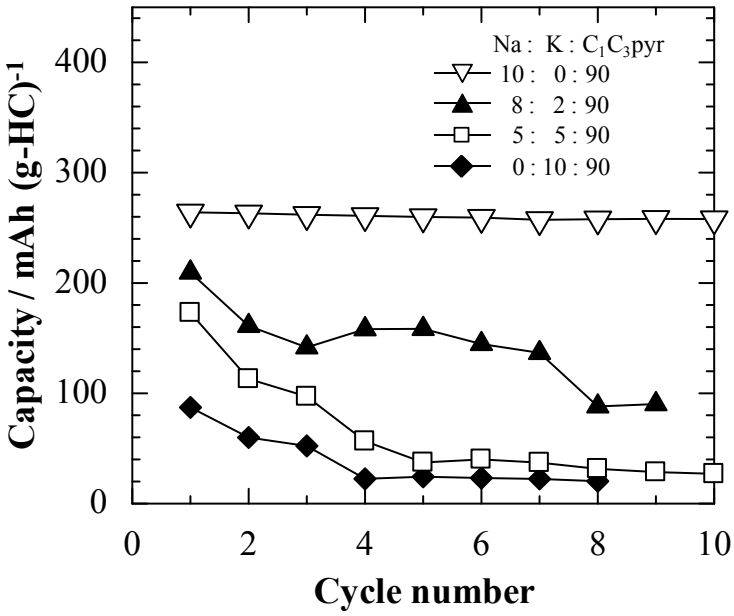

Fig. 5–5 Cycle dependence of discharge capacity for Na/Na[FSA]–K[FSA]–[C_3C_1pyrr][FSA]/HC cells (Na[FSA]:K[FSA]:[C_3C_1pyr][FSA] = 10:0:90, 8:2:90, 5:5:90 and 0:10:90 mol%) at 363 K. Charge–discharge rate: 50 mA $(g–HC)^{-1}$; cut–off voltages: 0.005 and 1.200 V.

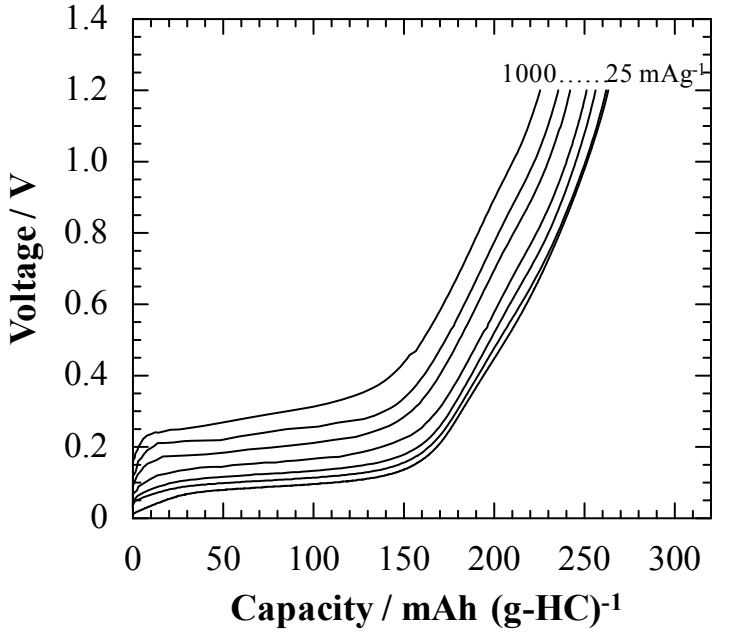

Fig. 5–6 Discharge curves for a Na/Na[FSA]–[C_3C_1pyrr][FSA]/HC cell at 363 K. Charge rate: 25 mA $(g–HC)^{-1}$; discharge rate: 25 (C/10), 50 (C/5), 125 (C/2), 250 (1C), 500 (2C), 750 (3C), and 1000 (4C) mA $(g–HC)^{-1}$; cut–off voltage: 1.200 V.

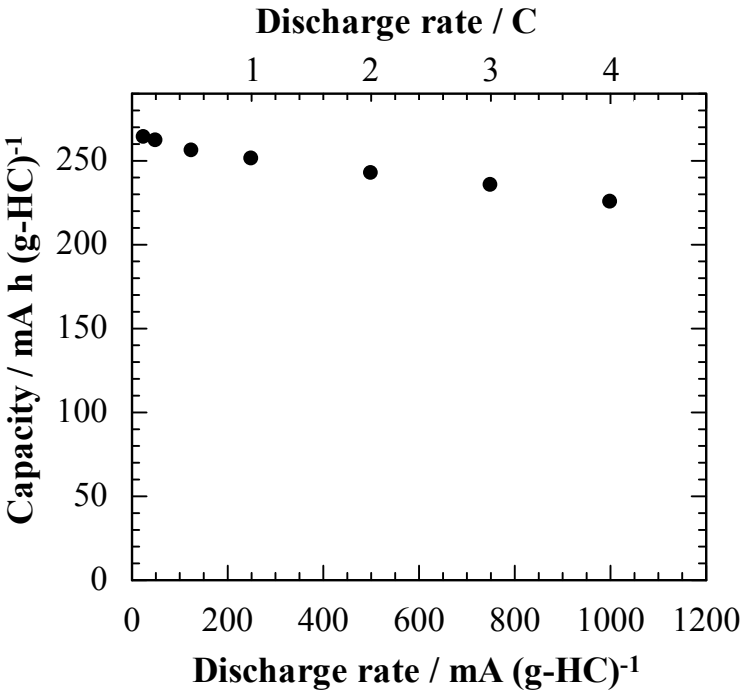

Fig. 5–7 Rate dependence of discharge capacity for a Na/Na[FSA]–[C_3C_1pyrr][FSA]/HC cell at 363 K. Charge rate: 25 mA $(g–HC)^{-1}$; discharge rate: 25 (C/10), 50 (C/5), 125 (C/2), 250 (1C), 500 (2C), 750 (3C), and 1000 (4C) mA $(g–HC)^{-1}$; cut–off voltage: 1.200 V.

Chapter 6

Full cell performance tests and evaluation of large–sized prismatic cell

6.1 Introduction

In previous Chapters, sodium metal was used as a negative electrode. Although dendrite deposition of sodium metal is suppressed by operating at a temperature close to the melting point of sodium (371 K), it is difficult to completely prevent dendrite deposition, especially at lower operating temperatures. Referring to the reports on hard carbon (HC) by Komaba et al. [1–3], the author also investigated HC negative electrodes (see Chapter 5) to avoid the use of sodium metal negative electrodes. Unfortunately, when the Na[FSA]–K[FSA] ionic liquid was used, HC irreversibly reacted with K^+ cations during the charge–discharge test. However, good reversibility and rate capability were obtained by using the Na[FSA]–[C_3C_1pyrr][FSA] ionic liquid.

Further research has been conducted on sodium secondary batteries using half–cells, especially coin–type half–cells. Some of the work using half–cells reported the results of long–term cycle life of batteries. However, investigations on long–term cycle life should also be verified by using full cells. Unfortunately, few studies have been conducted using "full cells." Although full cell performance is predictable from the results of positive and negative electrode

half–cell tests, actual verification using full cells is imperative for the practical applications of sodium secondary batteries. Ideally, the verification should also include the scaling up of full cells, because the most expected application of such cells is in large–size batteries.

In this Chapter, the author first investigated the fundamental charge–discharge characteristics of $NaCrO_2$ positive electrodes and HC negative electrodes using Na[FSA]–[C_3C_1pyrr][FSA] ionic liquids and coin–type half–cells at 333 and 363 K. Furthermore, the author examined, for the first time, the detailed full cell performance, including the long–term cycle life of a 1.5 mAh HC/$NaCrO_2$ cell using a coin–type cell over the temperature range of 273–363 K. Finally, the author fabricated a large–sized prismatic full cell with a capacity of 27 Ah and compared the performance with that of a coin–type cell.

6.2 Experimental

Na[FSA]–[C_3C_1pyrr][FSA] ionic liquid (Na[FSA]:[C_3C_1pyrr][FSA] = 20 mol% Na[FSA]) was used as the electrolyte (see Chapter 2).

The positive electrode active material, $NaCrO_2$, was prepared using a solid phase method as described in Chapter 3. $NaCrO_2$ electrode was fabricated as described in Chapter 2. The loading weight was 13.5 (mg–$NaCrO_2$) cm^{-2} (ca. 1.7 mAh in theoretical capacity 125 mAh (g–$NaCrO_2$)$^{-1}$). The HC negative electrode was also fabricated as described in Chapter 2 The loading weight was 5.2 (mg–HC) cm^{-2}.

Charge–discharge properties of Na/$NaCrO_2$ and Na/HC half–cells, and HC/$NaCrO_2$

full cell were measured with a 2032–type coin cell as described in Chapter 2. Charge–discharge tests were conducted at a constant current rate. Current rate and cut–off voltages are shown in Table 6–1. Temperature of the cell was maintained at 273–363 K by a thermostatic oven during the charge–discharge tests.

In addition to a coin–type full cell, a 27 Ah prismatic HC/$NaCrO_2$ full cell was fabricated using a mass production process. Fig. 6–1 shows the appearance of the fabricated 27 Ah cell. Positive electrodes, negative electrodes, and separators were the same as those used in the coin–type cell. Positive and negative electrode active materials were coated on both sides of the Al foil current collector. A bundle of electrodes and separators electrically connected in parallel via lead tabs. Na[FSA]–[C_3C_1pyrr][FSA] electrolyte was filled into an aluminum case (external size: 113 × 150 × 38 mm) and the lid sealed by laser welding. Charge–discharge tests of a 27 Ah HC/$NaCrO_2$ prismatic cell were conducted at a constant current rate in a thermostatic oven conducted by a computer controlled charge–discharge unit (ABE 1028–5V, Electrofield Corp.).

6.3 Results and discussion

6.3.1 $NaCrO_2$ half–cell (coin–type cell)

A typical charge–discharge curve of a coin–type Na/$NaCrO_2$ half–cell at 363 K is shown in Fig. 6–2 (a). The shape of charge–discharge curve is derived from phase transition of $Na_{1-x}CrO_2$ ($x < 0.5$) during charge–discharge [4, 5]. In our previous study, phase transitions of

$NaCrO_2$ at 363 K were evaluated by ex–situ XRD measurements [5]. The desodiation of $NaCrO_2$ during charging produces following phase transition: rhombohedral O3 ($x < 0.03$) → monoclinic O'3 ($x = 0.2$) → monoclinic P'3 ($x > 0.34$). The notations of the phase were designed by Delmas [6]. The potential plateau around 2.9 V indicates the mixed phase of O3/O'3 or O'3/P'3, whereas the potential slope from 3.0 V to 3.3 V means the change of interslab distance of CrO_2 layers in single phase. The observed reversible capacity is 110 mAh g^{-1}, and the coulombic efficiency is >99.9%, which are almost the same numbers as those reported in Chapter 4. Figs. 6–2 (b) and (c) show discharge curves at 363 and 333 K, respectively, at rates of 10–600 mA $(g–NaCrO_2)^{-1}$. The rate dependence of discharge capacity is also shown in Fig. 6–3. It is seen that the $Na/NaCrO_2$ cell maintains almost the same discharge capacity of 110 mAh g^{-1} at discharge rates below 100 mA g^{-1} at both 333 and 363 K. In the case of 363 K, the discharge capacity gradually decreases with the discharge rate, but retains approximately 80 mAh g^{-1} even at 400 mA g^{-1}. In contrast, the discharge capacity markedly decreases at 333 K as the discharge rate increases over 200 mA g^{-1}. Specifically, in the discharge curves at 333 K, the voltage of the plateaus drop and its length shortens at values higher than 200 mA g^{-1}. These results indicate that the operating temperature has a significant effect on the discharge rate performance. These results suggest that Na^+ ion insertion into the CrO_2 layer of $NaCrO_2$ is decelerated at lower temperatures.

6.3.2 Hard carbon half–cell (coin–type cell)

A typical charge–discharge curve for a Na/HC cell at 50 mA g^{-1} at 363 K is shown in Fig. 6–4 (a). The observed reversible capacity is ca. 270 mAh g^{-1} and the coulombic efficiency is higher than 99%. The cycle properties of the Na/HC cell have already been reported in previous study (see Chapter 5). Discharge curves at various discharge rates of 25–1000 mA g^{-1} at 363 and 333 K are shown in Figs. 6–4 (b) and (c), respectively. The outline shapes of discharge curves do not change even at 750 mA g^{-1} at 333 K and 1000 mA g^{-1} at 363 K. The observed positive shifts of the curves at higher discharge rates (> 250 mA g^{-1}) are likely due to IR drops, because the value of positive shift is proportional to the increment of discharge rate (current density).

Fig. 6–5 shows the rate dependence of the discharge capacity at 333 and 363 K. The observed discharge capacities at the same discharge rate are almost identical at both temperatures, indicating that the rate of Na^+ extraction from HC is not largely affected by temperature under the present experimental conditions. In summary, the HC negative electrode has excellent rate capability in the Na[FSA]–[C_3C_1pyrr][FSA] ionic liquid at 333 and 363 K. A comparison of Fig. 6–3 with Fig. 6–5 clearly indicates that the HC negative electrode has a superior rate capability than the $NaCrO_2$ positive electrode, in the present tests.

6.3.3 1.5 mAh HC/$NaCrO_2$ full cell (coin–type cell)

Fig. 6–6 (a) shows the charge–discharge curve for a 1.5 mAh HC/$NaCrO_2$ full cell

operating in the voltage range of 1.5–3.4 V at 0.3 mA and 363 K. The voltage plateaus observed at around 2.9 V on both the charge and discharge curves are derived from the character of the $NaCrO_2$ positive electrode. The monotonic voltage changes in the region of 1.5–2.7 V arise from the features of the HC negative electrode. The average discharge voltage is ca. 2.6 V. The observed cell capacity is 1.53 mAh, which corresponds to 102 mAh $(g–NaCrO_2)^{-1}$ for the positive electrode and 252 mAh $(g–HC)^{-1}$ for the negative electrode. Since the reversible capacities observed in the half–cell tests are 110 mAh $(g–NaCrO_2)^{-1}$ and 270 mAh $(g–HC)^{-1}$, the capacity utilizing ratios are calculated as ca. 93% for the $NaCrO_2$ and HC electrodes. Discharge curves at discharge rates of 0.3–9.0 mA (approximately 5/C–6C rate) at 363 and 333 K are shown in Figs. 6–6 (b) and (c), respectively. Appreciable changes are observed from 9.0 mA at 363 K and 3.0 mA at 333 K. The observed charge–discharge characteristics are consistent with the results of the half–cells. A superior rate capability is achieved when the cell is operated at 363 K.

To check whether the HC/$NaCrO_2$ full cell works at temperatures lower than 333 K, charge–discharge tests were conducted at 313, 298, 283, and 273 K. Fig. 6–7 shows typical discharge curves at 0.3 mA and 298 K, and 0.15 mA at 283 K. The discharge capacities are 1.50 mAh at 298 K and 1.35 mAh at 283 K. This result confirms that the HC/$NaCrO_2$ full cell is operable at room temperature or even lower than room temperature with moderate discharge rates. Fig. 6–8 shows the rate dependence of the discharge capacity at 273–363 K. The

designated capacity of 1.5 mAh is exerted at temperatures higher than 298 K. The rate capability steadily increases as the temperature increases. The highest rate capability is attained at 363 K.

Fig. 6–9 shows the cycle properties of the 1.5 mAh HC/$NaCrO_2$ full cell at 1C rate at 333 K and 363 K. Even for the fully charging and discharging tests, remarkably stable cycleability is obtained. The capacity is maintained up to 90% of the initial capacity after 1000 cycles. There is almost no difference in the capacity retentions between 333 K and 363 K. This stable cycleability at 363 K is an astounding achievement, considering that conventional LIBs employing organic solvent–based electrolytes cannot be operated at such high temperatures. The long–term cycle stability in the intermediate temperature range is attributed to the high thermal stability of SEI films on HC negative electrodes as well as good thermal stability of the Na[FSA]–[C_3C_1pyrr][FSA] ionic liquid itself. Table 6–2 summarizes the coulombic and energy efficiencies for the HC/$NaCrO_2$ full cell at a rate of 0.3 mA at 298, 333, and 363 K. The obtained coulombic efficiencies are higher than 99.7% for all temperatures. Considerably high charge–discharge energy efficiencies are achieved: 96.9% at 333 K and 97.5% at 363 K. These values are comparable with, or better, than those of conventional LIBs at ambient temperature [7, 8]. The slight decrease in the energy efficiency at 298 K (93.2%) is caused by the increase in the internal resistance due to lower ionic conductivity.

6.3.4 27 Ah HC/$NaCrO_2$ full cells (large–sized prismatic cell)

Based on the results for coin–type cells, large–size prismatic cells having a designed capacity of 27 Ah were fabricated. The weight and volume of the 27 Ah cell were 1.08 kg, and 0.644 L, respectively.

Fig. 6–10 shows the charge–discharge curves for the 27 Ah HC/$NaCrO_2$ full cell at 298 and 333 K. The observed discharge capacity at a rate of 2.7 A is 27.3 Ah at 298 K, which is equal to the designed capacity. At 333 K, almost the same charge–discharge behavior is obtained, even at the higher rate of 10 A. The calculated volumetric and gravimetric energy densities of the 27 Ah cell are ca. 125 Wh L^{-1} and 75 Wh kg^{-1}, respectively. These values are comparable with those for large–scale prismatic LIBs in the early 2000s [9]. It should be noted that the shape of the charge–discharge curve for the 27 Ah cell is almost identical to that of a 1.5–mAh coin–type cell. Thus, it is expected that the performance of a large–sized full cell is well predicted by that of a coin–type cell. Actually, the calculated energy efficiencies at a rate of 5.4 A are 93.9% at 298 K and 96.8% at 333 K. These values are almost the same as those for coin–type cells shown in Table 6–2.

Fig. 6–11 shows the rate dependence of discharge capacity for the 27 Ah full cell at 283, 298, 313, 333, and 363 K. Again, the rate capability is comparable with that for the 1.5 mAh coin–type cell. An especially superior rate capability is obtained at 333 and 363 K. On the other hand, the performance is unsatisfactory at 283 K, which is due to the lower conductivity of the ionic liquid. Fig. 6–12 shows the cycleability of the 27 Ah full cell at a rate of 10 A at 333

K. This is also the fully charging and discharging test done in the same manner as the coin–type cell. The capacity retention after 500 cycles is 87%. Although this value is slightly lower than that of the 1.5 mAh coin–type cell shown in Fig. 6–6, it is the same value as that of large–scaled prismatic LIBs used in the early 2000s [9]. Considering that the 27 Ah cell has been produced by an industrial process similar to that for conventional LIBs, it is safe to say that a large–sized HC/Na[FSA]–[C_3C_1pyrr][FSA]/$NaCrO_2$ cell can show further improvements in energy density, power density (rate capability), energy efficacy, and cycleability with improved manufacturing technology.

As described in this section, HC/Na[FSA]–[C_3C_1pyrr][FSA]/$NaCrO_2$ cells exhibit high performance and long cycle life over a wide temperature range including a high temperature of 363 K. Thus, these cells are best expected to be used in new fields where conventional LIBs cannot be used. For example, near heated devices such as engines in hybrid electric vehicles (HEVs), or fuel cells in fuel cell vehicles (FCVs). This is highly beneficial even for electric vehicles (EVs). The temperature controlling system for the EV battery becomes much simpler, and the closest packing of cells can be realized because the upper–limit temperature of the battery is improved by 40–50 K compared with that in conventional LIBs. In addition, these cells can be used in mid–to–large–sized power storage devices that are operated under hot environments (for example, the tropical and desert regions).

6.4 Conclusions

Sodium ion batteries consisting of an HC negative electrode, a $NaCrO_2$ positive electrode, and a Na[FSA]–[C_3C_1pyrr][FSA] ionic liquid have been systematically investigated using coin–type half–cells, coin–type full cells, and large–sized full cells at 273–363 K. First, fundamental charge–discharge characteristics of $NaCrO_2$ and HC electrodes were presented using coin–type half–cells at 333 and 363 K. Second, a coin–type 1.5 mAh HC/$NaCrO_2$ full cell was successfully fabricated, giving a specific capacity of 102 mAh $(g–NaCrO_2)^{-1}$ and 252 mAh $(g–HC)^{-1}$ at an operation voltage range of 1.5–3.35 V. Charge–discharge energy efficiencies were as high as 96.9% at 333 K, and 97.5% at 363 K. The cell also exhibited a wide operational temperature range of 283–363 K, and excellent cycle performance of 90% capacity retention after 1000 cycles at 363 K. Finally, a 27 Ah HC/$NaCrO_2$ full cell was constructed using a mass production process. The calculated volumetric and gravimetric energy densities were 125 Wh L^{-1} and 75 Wh kg^{-1}, respectively. The energy efficiencies were 93.9% at 298 K, and 96.8% at 333 K, as high as those of the coin–type 1.5 mAh full cell. The 27 Ah full cell also showed a wide operational temperature range and a long cycle life of 87% capacity retention after 500 cycles. The performance of the 27 Ah cell was comparable with that of the 1.5 mAh coin–type cell, demonstrating for the first time the successful fabrication of a large–scale sodium–ion battery using a Na[FSA]–[C_3C_1pyrr][FSA] ionic liquid.

References

[1] M. Dahbi, T. Nakano, N. Yabuuchi, T. Ishikawa, K. Kubota, M. Fukunishi, S. Shibahara, J. Y. Son, Y. T. Cui, H. Oji, S. Komaba, Electrochem. Comm. 44 (2014) 66–69.

[2] K. Gotoh, T. Ishikawa, S. Shimadzu, N. Yabuuchi, S. Komaba, K. Takeda, A. Goto, K. Deguchi, S. Ohki, K. Hashi, T. Shimizu, H. Ishida, J. Power Sources 225 (2013) 137–140.

[3] S. Komaba, W. Murata, T. Ishikawa, N. Yabuuchi, T. Ozeki, T. Nakayama, A. Ogata, K. Gotoh, K. Fujiwara, Adv. Funct. Mater. 21 (2011) 3859–3867.

[4] S. Komaba, C. Takei, T. Nakayama, A. Ogata, N. Yabuuchi, Electrochem. Comm. 12 (2012) 355–358.

[5] C.Y. Chen, K. Matsumoto, T. Nohira, R. Hagiwara, A. Fukunaga, S. Sakai, K. Nitta, S. Inazawa, J. Power Sources 237 (2013) 52–57.

[6] C. Delmas, C. Fouassier, P. Hagenmuller, Physica B+C 99 (1980) 81–85.

[7] J. Rydh, B. A. Sandén, Energ. Convers. Manag. 46 (2005) 1980–2000.

[8] H. Chen, T. N. Cong, W. Yang, C. Tan, Y. Li, Y. Ding, Prog. Nat. Sci. 19 (2009) 291–312.

[9] T. Iguchi, K. Okamoto, J. Kuratomi, K. Ohkawa, K. Kohno, S. Izuchi, GS Yuasa Technical Report 1 (2004) 25–31 (in Japanese).

Tables

Table 6–1 Charge and discharge conditions for $Na/NaCrO_2$, Na/HC, and $HC/NaCrO_2$ cells.

Cell	Charge rate	Discharge rate	Cut–off voltages
$Na/NaCrO_2$	20 mA $(g–NaCrO_2)^{-1}$	20–600 mA $(g–NaCrO_2)^{-1}$	2.5 and 3.5 V
Na/HC	25 mA $(g–HC)^{-1}$	25–1000 mA $(g–HC)^{-1}$	0.005 and 1.2 V
$HC/NaCrO_2$	20–100 mA $(g–NaCrO_2)^{-1}$	10–600 mA $(g–NaCrO_2)^{-1}$	1.5 and 3.35 V

Table 6–2 Coulombic and energy efficiencies for a 1.5 mAh $HC/Na[FSA]–[C_3C_1pyrr][FSA]/NaCrO_2$ full cell. Operating temperatures: 298, 333, and 363 K. Charge–discharge rate: 0.3 mA.

Operating temperature	Coulombic efficiency	Energy efficiency
363 K	99.85%	97.5%
333 K	99.84%	96.9%
298 K	99.78%	93.2%

Figures

Fig. 6–1 Appearance of a 27 Ah HC/Na[FSA]–[C_3C_1pyrr][FSA]/$NaCrO_2$ prismatic cell. External size: 113×150×38 mm. Weight: 1.08 kg.

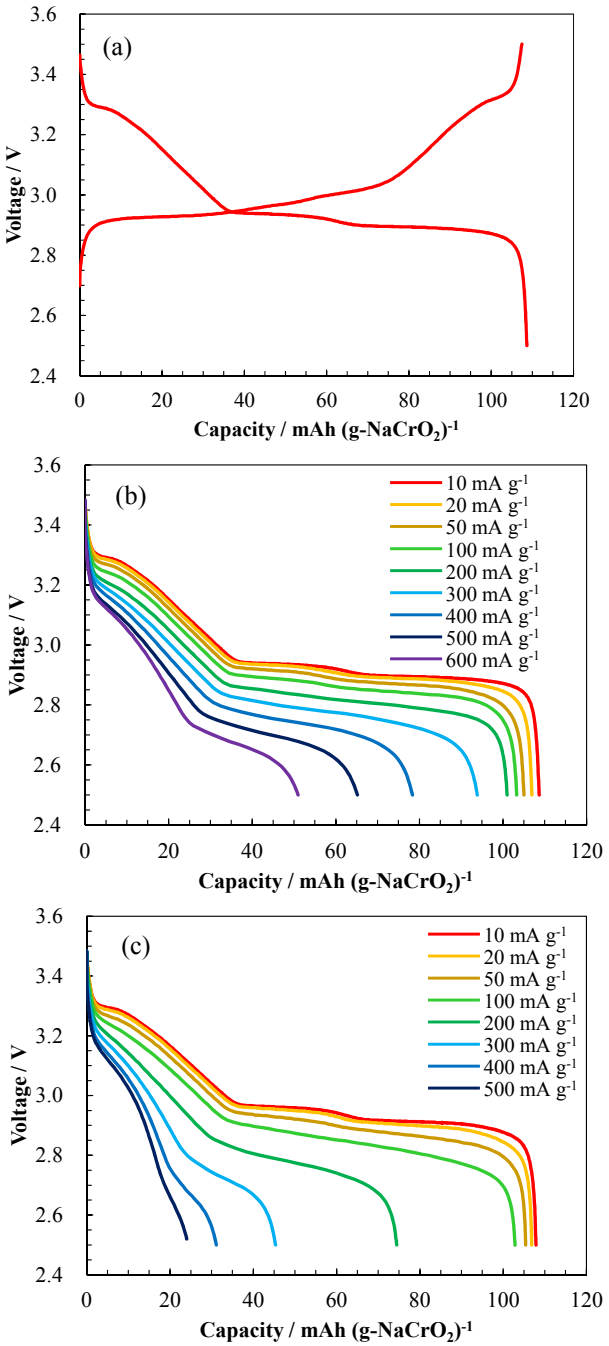

Fig. 6–2 (a) A charge–discharge curve for a Na/Na[FSA]–[C_3C_1pyrr][FSA]/$NaCrO_2$ cell at 363 K. Charge–discharge rate: 20 mA (g–$NaCrO_2$)$^{-1}$. (b) Discharge curves at 363 K and (c) discharge curves at 333 K. Charge rate: 20 mA (g–$NaCrO_2$)$^{-1}$. Discharge rate: 10–600 mA (g–$NaCrO_2$)$^{-1}$. Cut–off voltages: 2.5 V and 3.5 V.

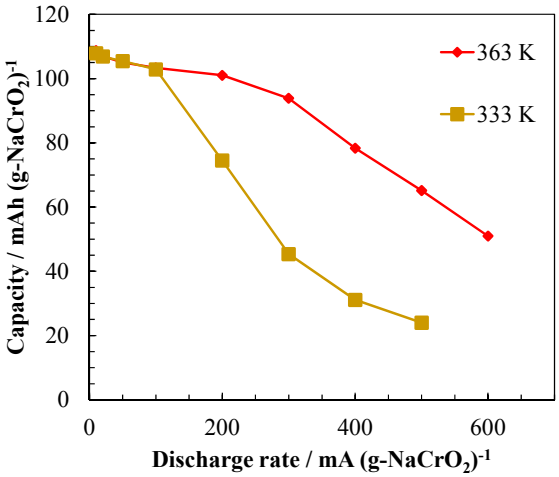

Fig. 6–3 Rate dependence of discharge capacity for a Na/Na[FSA]–[C_3C_1pyrr][FSA]/$NaCrO_2$ cell. Charge rate: 20 mA (g–$NaCrO_2$)$^{-1}$, discharge rate: 10–600 mA (g–$NaCrO_2$)$^{-1}$. Operation temperature: 333 and 363 K.

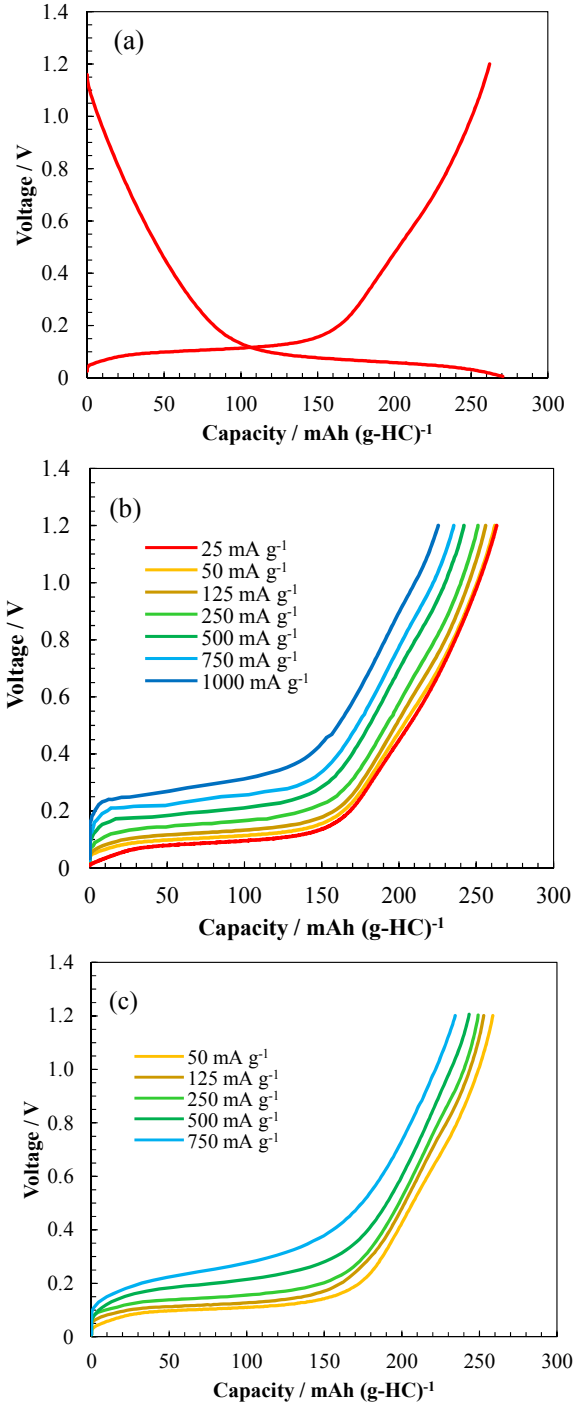

Fig. 6–4 (a) A charge–discharge curve for a Na/Na[FSA]–[C_3C_1pyrr][FSA]/HC cell at 363 K. Charge–discharge rate: 50 mA (g–HC)$^{-1}$. (b) Discharge curves at 363 K and (c) discharge curves at 333 K. Charge rate: 50 mA (g–HC)$^{-1}$. Discharge rate: 25–1000 mA (g–HC)$^{-1}$. Cut–off voltages: 0.005 V and 1.2 V.

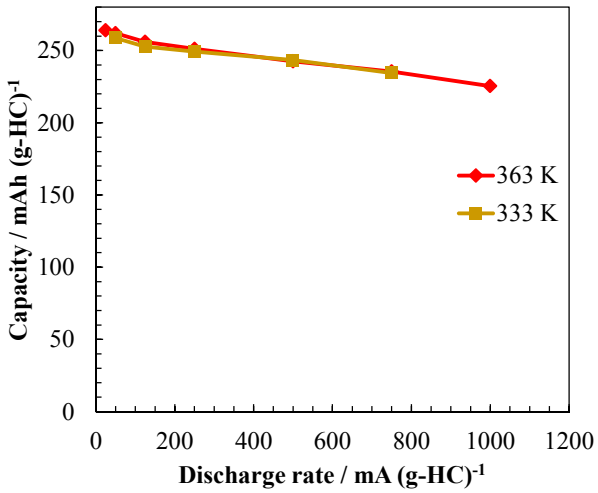

Fig. 6–5 Rate dependence of discharge capacity for a Na/Na[FSA]–[C_3C_1pyrr][FSA]/HC cell. Charge rate: 50 mA $(g–HC)^{-1}$, discharge rate: 25–1000 mA $(g–HC)^{-1}$. Operation temperature: 363 and 333 K.

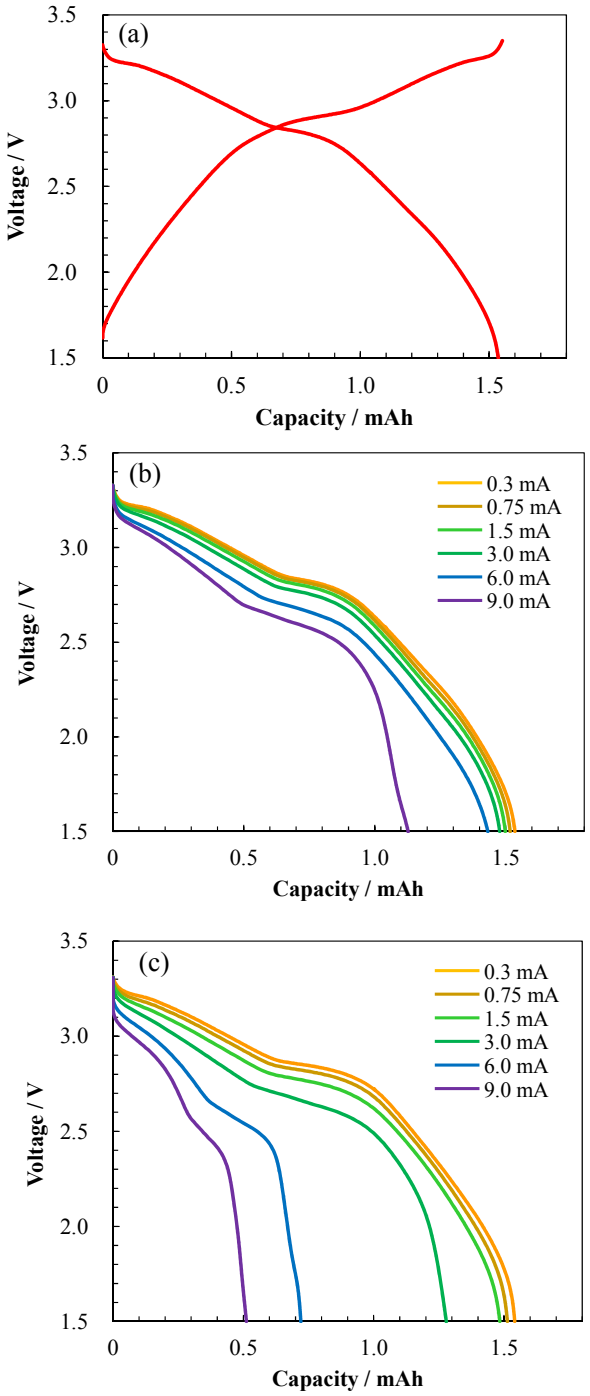

Fig. 6–6 (a) A charge–discharge curve for a 1.5 mAh HC/Na[FSA]–[C_3C_1pyrr][FSA]/$NaCrO_2$ full cell at 363 K. Charge–discharge rate: 0.3 mA. (b) Discharge curves at 363 K, and (c) discharge curves at 333 K. Charge rate: 0.3 mA. Discharge rate: 0.3–9.0 mA. Cut–off voltages: 1.5 V and 3.4 V.

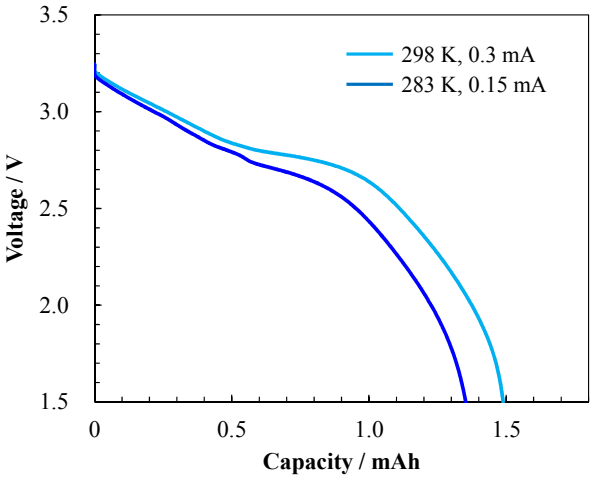

Fig. 6–7 Discharge curves for a 1.5 mAh HC/Na[FSA]–[C_3C_1pyrr][FSA]/$NaCrO_2$ full cell at 298 and 283 K. Charge condition: 0.3 mA CC–CV (to 0.075 mA) at 298 K. Discharge rate: 0.3 mA (298 K) and 0.15 mA (283 K). Cut–off voltages: 1.5 V and 3.35 V.

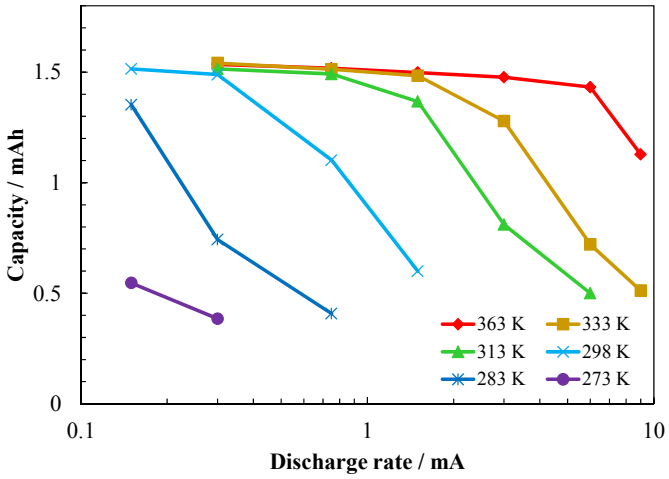

Fig. 6–8 Rate dependence of the discharge capacity for a 1.5 mAh HC/Na[FSA]–[C_3C_1pyrr][FSA]/$NaCrO_2$ full cell. Charge condition: 0.3 mA CC (313–363 K) and 0.3 mA CC–CV (to 0.075 mA) at 298 K (273–298 K). Discharge rate: 0.15–9.0 mA. Operation temperature: 273–363 K.

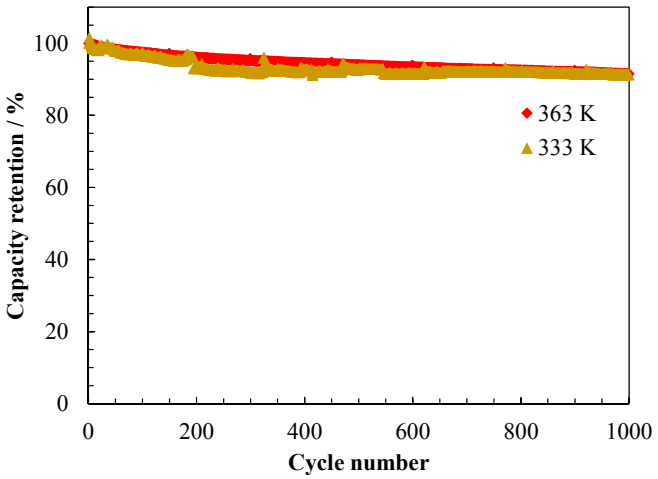

Fig. 6–9 Cycle property for a HC/Na[FSA]–[C_3C_1pyrr][FSA]/$NaCrO_2$ full cell. Charge–discharge rate: 1.5 mA. Operation temperature: 363 K and 333 K. Cut–off voltages: 1.5 V and 3.35 V.

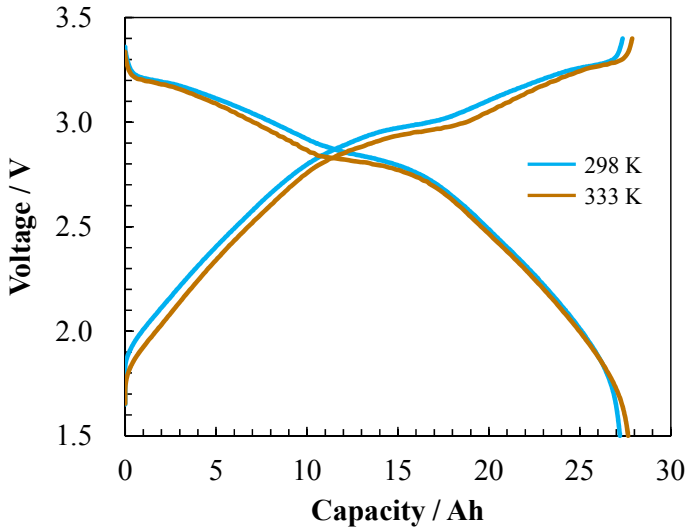

Fig. 6–10 Charge–discharge curves for a 27 Ah HC/Na[FSA]–[C_3C_1pyrr][FSA]/$NaCrO_2$ full cell at 298 and 333 K. Charge–discharge rate: 2.7 A (298 K) and 10 A (333 K). Cut–off voltages: 1.5 V and 3.35 V.

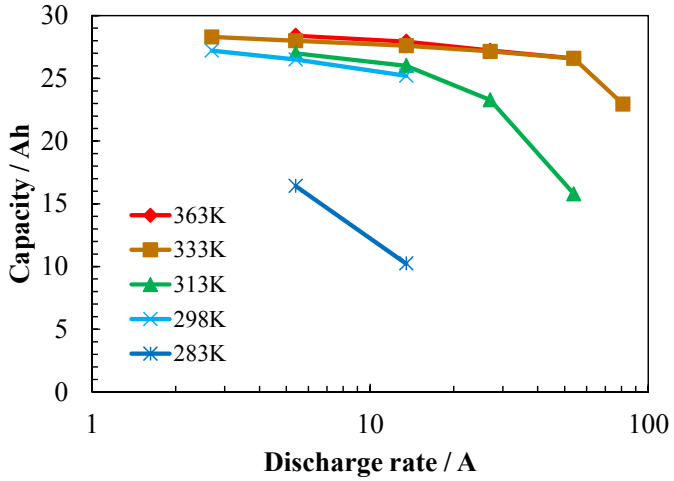

Fig. 6–11 Rate dependence of discharge capacity for a 27 Ah HC/Na[FSA]–[C_3C_1pyrr][FSA]/$NaCrO_2$ full cell. Charge rate: 2.7 A (283–293 K) and 5.4 A (313–363 K), discharge rate: 2.7–81 A. Operation temperature: 283–363 K.

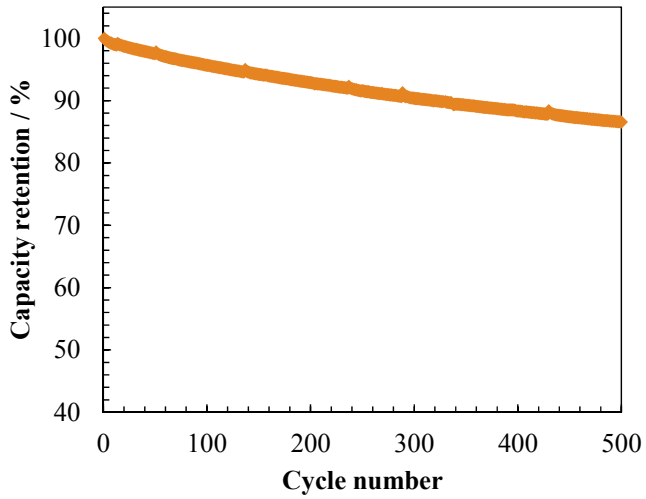

Fig. 6–12 Cycle property for a 27 Ah HC/Na[FSA]–[C_3C_1pyrr][FSA]/$NaCrO_2$ full cell. Charge–discharge rate: 10 A. Operation temperature: 333 K. Cut–off voltages: 1.5 V and 3.35 V.

Chapter 7

General conclusions

The aim of this study was to confirm the potential high performance of sodium secondary batteries utilizing ionic liquids. The results obtained through this study are summarized as follows.

In chapter 3, densities, viscosities, ionic conductivities, and electrochemical windows were measured for the eutectic Na[FSA]–K[FSA] melt. The viscosities and ionic conductivities are well described by VTF equations. The logarithmic molar conductivity is proportional to the logarithmic reciprocal viscosity, which obeys the fractional Walden rule. The binary eutectic Na[FSA]–K[FSA] melt possesses a wide electrochemical window of ca. 5.2 V at 363 K. Aluminum is stable as the current collector material for the positive electrode, even at the high–potential region, in this ionic liquid. A Na/Na[FSA]–K[FSA]/$NaCrO_2$ cell showed excellent cycle performance at 353 K, whereby 89% of the initial discharge capacity was maintained after 100 cycles with coulombic efficiencies of almost 100% at a charge–discharge rate of 15 mA $(g–NaCrO_2)^{-1}$. It is concluded that the binary eutectic Na[FSA]–K[FSA] melt is a promising electrolyte for a sodium secondary battery operating at intermediate temperatures, and that $NaCrO_2$ is a good candidate as a positive electrode active material.

In chapter 4, the author investigated the physicochemical properties of Na[FSA]–[C_3C_1pyrr][FSA] ionic liquids. This ionic liquid exhibits a wide electrochemical window of 5.2 V at 353 K. The viscosity increases and the ionic conductivity decreases when the Na ion concentration in IL increases. By the elevation of temperature, however, ionic conductivities much higher than that of conventional organic electrolyte at room temperature are achieved. The Na ion concentration in the ionic liquids strongly affects the rate capability of a Na/Na[FSA]–[C_3C_1pyrr][FSA]/$NaCrO_2$ cell. The best rate capability at 363 K is obtained at 40 mol% Na[FSA]. The operation temperature also significantly influences the charge–discharge performance, especially at low temperatures, and the discharge capacity gradually decreases when the operation temperature is lowered. At operation temperatures below 273 K, 25 mol% Na[FSA] is found to be the optimum Na ion concentration. It is concluded that the optimum Na ion concentration depends on the operation temperatures.

Chapter 5 describes the charge–discharge properties of HC in a Na[FSA]–[C_3C_1pyrr][FSA] ionic liquid. The cycling test of a Na/Na[FSA]–[C_3C_1pyrr][FSA]/HC cell at 363 K revealed that the HC electrode has a reversible capacity of ca. 250 mAh $(g– HC)^{-1}$ in this electrolyte, and that 95.5% of the first discharge capacity maintains after 50 cycles with 99.9% coulombic efficiency. In contrast, a Na/HC cell with Na[FSA]–K[FSA] electrolyte showed poor reversibility. By using Na[FSA]–K[FSA]–[C_3C_1pyrr][FSA] systems with various Na^+/K^+ ratios, it was revealed that irreversible K^+ insertion inhibits the reversible Na^+

insertion into HC. Finally, the Na/Na[FSA]–[C_3C_1pyrr][FSA]/HC cell was demonstrated to have an excellent rate capability. At a rate of 1000 mA (g–HC)$^{-1}$ (4C), a discharge capacity of 211 mAh (g–HC)$^{-1}$ was obtained, which corresponds to 80% of the capacity at 25 mA (g–HC)$^{-1}$ (C/10). Thus, the combination of HC electrode and Na[FSA]–[C_3C_1pyrr][FSA] ionic liquid provides a safe and high–rate negative electrode for sodium–ion batteries.

In chapter 6, sodium ion batteries consisting of an HC negative electrode, a $NaCrO_2$ positive electrode, and a Na[FSA]–[C_3C_1pyrr][FSA] ionic liquid have been systematically investigated using coin–type half–cells, coin–type full cells, and large–sized full cells at 273–363 K. First, fundamental charge–discharge characteristics of $NaCrO_2$ and HC electrodes were studies by using coin–type half–cells at 333 K and 363 K. Secondly, a coin–type 1.5 mAh HC/$NaCrO_2$ full cell was successfully fabricated, which gave a specific capacity of 102 mAh (g–$NaCrO_2$)$^{-1}$ and 252 mAh (g–HC)$^{-1}$ at an operation voltage range of 1.5–3.35 V. The charge–discharge energy efficiencies were as high as 96.9% at 333 K, and 97.5% at 363 K. The cell also exhibited a wide operational temperature range of 283–363 K, and excellent cycle performance of 90% capacity retention after 1000 cycles at 363 K. Finally, a 27 Ah HC/$NaCrO_2$ full cell was constructed using a mass production process. The calculated volumetric and gravimetric energy densities were 125 Wh L^{-1} and 75 Wh kg^{-1}, respectively. The energy efficiencies were 93.9% at 298 K, and 96.8% at 333 K, as high as those of the coin–type 1.5 mAh full cell. The 27 Ah full cell also had a wide operational temperature range and a long cycle life of 87% capacity

retention after 500 cycles. The performance of the 27 Ah cell was comparable with that of the 1.5 mAh coin–type cell, demonstrating for the first time the successful fabrication of a large–scale sodium–ion battery using the Na[FSA]–[C_3C_1pyrr][FSA] ionic liquid.

The obtained results in this study are of great importance in designing practical batteries for various applications such as grid applications and EVs. As can be seen from the past significant improvements in the LIBs' technology, further improvements are also expected for the performance and cycleability of the practical sodium secondary batteries utilizing ionic liquids.

List of publications

Chapter 3

"Intermediate–temperature ionic liquid NaFSA–KFSA and its application to sodium secondary batteries"

Atsushi Fukunaga, Toshiyuki Nohira, Yu Kozawa, Rika Hagiwara, Shoichiro Sakai, Koji Nitta, Shinji Inazawa

Journal of Power Sources 209 (2012) 52–56.

Chapter 4

"NaFSA–C_1C_3pyrFSA ionic liquids for sodium secondary battery operating over a wide temperature range"

Changsheng Ding, Toshiyuki Nohira, Keisuke Kuroda, Rika Hagiwara, Atsushi Fukunaga, Shoichiro Sakai, Koji Nitta, Shinji Inazawa

Journal of Power Sources 238 (2013) 296–300.

"Na[FSA]–[C_3C_1pyrr][FSA] ionic liquid as electrolytes for sodium secondary batteries: Effects of Na ion concentration and operation temperature"

Changsheng Ding, Toshiyuki Nohira, Rika Hagiwara, Kazuhiko Matsumoto, Yu Okamoto, Atsushi Fukunaga, Shoichiro Sakai, Koji Nitta, Shinji Inazawa

Journal of Power Sources 269 (2014) 124–128

Chapter 5

"A safe and high–rate negative electrode for sodium–ion batteries: hard carbon in NaFSA–C_1C_3pyrFSA ionic liquid at 363 K"

Atsushi Fukunaga, Toshiyuki Nohira, Rika Hagiwara, Koma Numata, Eiko Itani, Shoichiro Sakai, Koji Nitta, Shinji Inazawa

Journal of Power Sources 246 (2014) 387–391.

Chapter 6

"Performance validation of sodium–ion batteries using an ionic liquid electrolyte"

Atsushi Fukunaga, Toshiyuki Nohira, Rika Hagiwara, Koma Numata, Eiko Itani, Shoichiro Sakai, Koji Nitta

Accepted to Journal of Applied Electrochemistry

List of related publications

1. “Charge–discharge behavior of tin negative electrode for a sodium secondary battery using intermediate temperature ionic liquid sodium bis(fluorosulfonyl)amide–potassium bis(fluorosulfonyl)amide”

   Takayuki Yamamoto, Toshiyuki Nohira, Rika Hagiwara, Atsushi Fukunaga, Shoichiro Sakai, Koji Nitta, Shinji Inazawa,

   Journal of Power Sources 217 (2012) 479–484.

2. “Electrochemical and structural investigation of $NaCrO_2$ as a positive electrode for sodium secondary battery using inorganic ionic liquid NaFSA–KFSA”

   Chih–Yao Chen, Kazuhiko Matsumoto, Toshiyuki Nohira, Rika Hagiwara, Atsushi Fukunaga, Shoichiro Sakai, Koji Nitta, Shinji Inazawa,

   Journal of Power Sources 237 (2013) 52–57.

3. “Thermodynamic studies on Sn–Na alloy in an intermediate temperature ionic liquid NaFSA–KFSA at 363 K”

   Takayuki Yamamoto, Toshiyuki Nohira, Rika Hagiwara, Atsushi Fukunaga, Shoichiro Sakai, Koji Nitta, Shinji Inazawa,

   Journal of Power Sources 237 (2013) 98–103.

4. “Improved cyclability of Sn–Cu film electrode for sodium secondary battery using inorganic ionic liquid electrolyte”

   Takayuki Yamamoto, Toshiyuki Nohira, Rika Hagiwara, Atsushi Fukunaga, Shoichiro Sakai, Koji Nitta, Shinji Inazawa,

   Electrochimica Acta 135 (2014) 60–67.

5. “The Na[FSA]–[C_2C_1im][FSA] ($C_2C_1im^+$: 1–ethyl–3–methylimidazolium and FSA^-: bis(fluorosulfonyl)amide) ionic liquid electrolytes for sodium secondary batteries”
Kazuhiko Matsumoto, Takafumi Hosokawa, Toshiyuki Nohira, Rika Hagiwara, Atsushi Fukunaga, Koma Numata, Eiko Itani, Shoichiro Sakai, Koji Nitta, Shinji Inazawa,
Journal of Power Sources 265 (2014) 36–39.

6. “Electrochemical performance of hard carbon negative electrodes for ionic liquid–based sodium ion batteries over a wide temperature range”
Changsheng Ding, Toshiyuki Nohira, Rika Hagiwara, Atsushi Fukunaga, Shoichiro Sakai, Koji Nitta,
Electrochimica Acta 176 (2015) 344–349.

7. “Charge–discharge performance of an ionic liquid–based sodium secondary battery in a wide temperature range”
Changsheng Ding, Toshiyuki Nohira, Atsushi Fukunaga, Rika Hagiwara,
Electrochemistry 83 (2015) 91–94.

Acknowledgement

The author would like to express deep appreciation to Professor Rika Hagiwara for his supervision over all the Chapters of this thesis and kind encouragement. The author is sincerely grateful to Professor Toshiyuki Nohira for his earnest guidance and fruitful discussions throughout this study. The author would like to thank Professor Takashi Sagawa for his valuable comments on this thesis.

The author would like to express his great appreciation to Mr. Yoshihiro Nakai, chief of the author's section in Sumitomo Electric Industries, ltd. (SEI), for giving the chance of this study and kind encouragement throughout this study. The author would like to thank to all the members of "Electrochemistry section" in SEI, especially Dr. Koji Nitta Dr. Shoichiro Sakai, Mr. Koma Numata, and Ms. Eiko I. Imazaki for their valuable suggestions and stimulating discussions. The author would like to thank to the member of "Duties for research section" in SEI, especially Mr. Takashi Ueda, Mr. Yoshitaka Hashidzume, Mr. Masashi Yamashita, Mr. Hiroyuki Okamoto, and Mr. Hisatsugu Kurokawa for their great assistance on experiments. The author would like to thank Associate Professor Kazuhiko Matsumoto, Assistant Professor Changsheng Ding, Dr. Chih–Yao Chen, and Mr. Takayuki Yamamoto for their valuable discussions. The author would like to thank to all the members of Professor Hagiwara's laboratory for giving unique viewpoints.

Finally, the author would like to offer his special thanks to his family, Mrs. Ikumi Fukunaga, Mr. Hayato Fukunaga, and Miss Akari Fukunaga, for their cooperation and encouragement.

Atsushi Fukunaga

March 2016